Cold Air Drainage Flows and their Relation to the Formation of Nocturnal Convective Clouds at the Eastern Andes of South Ecuador

kumulative Dissertation
zur Erlangung des Doktorgrades
der Naturwissenschaften
(Dr. rer. nat.)

dem Fachbereich Geographie
der Philipps-Universität Marburg
vorgelegt von

Katja Trachte
aus Willingen - Schwalefeld

Marburg / Lahn 2010

Vom Fachbereich Geographie
der Philipps-Universität Marburg als Dissertation
am 27. Oktober 2010 angenommen.

Erstgutachter: Prof. Dr. Jörg Bendix (Marburg)
Zweitgutachter: Prof. Dr. Thomas Nauss (Bayreuth)
Drittgutachter: Prof. Dr. Thomas Foken (Bayreuth)

Tag der mündlichen Prüfung: 2. Februar 2011

Preface

At the end of a challenging time I would like to thank all the persons who supported and accompanied me on my way to realise this work. I have learned many things during this time. I experienced what it means to work for a long period of time on the same project with rapid progress and zero progress. Not at least because of all the persons around me I persued that way to its final objective.

With special gratitude I have to thank my supervisor Jörg Bendix for his extensive counsel and backing. He at all times had open ears and provide any support needed. I thank him for his contagious enthusiasm for scientific issues and finding solutions for unresolved questions.

Special thanks go to my colleagues at the Laboratory for Climatology and Remote Sensing at Philipps-University of Marburg. During this time they supported me in many situations ranging from little everyday problems to scientific discussions or just coffee breaks in our kitchen. I thank Thomas Nauss for many fruitful exchanges and discussions as well as for multiple help in everyday problems in scientific life. I thank Rütger Rollenbeck for his support and the funny days in Ecuador. Further, I thank Jan Cermak, who showed me more than once the fascination and challenge of scientific work.

A fundamental contribution to this thesis came from the open source software community, without this work could not have been conducted that way. I thank the OpenSuse community and the GNU project for realisation of many parts of this work, and the LaTeX within this thesis was typed.

The work was embedded in a subproject (B3.1, BE 1780/15-1, NA 783/1-1) within the research unit RU816 that was funded by the Deutsche Forschungsgemeinschaft (DFG). This is greatfully acknowledged.

Finally, I thank my parents for their support during my education and my sister Simone for her backing whenever needed.

Katja Trachte
Marburg, October 2010

Contents

List of Figures III

List of Tables VII

List of Acronyms IX

List of Symbols XI

1 Introduction 1
- 1.1 Motivation . . . 2
- 1.2 Aims and Outlines . . . 4

2 Conceptual Design 11
- 2.1 Detecting and Analysing Methods . . . 11
- 2.2 Numerical Gridbox Models . . . 12
  - 2.2.1 Advanced Regional Prediction System (ARPS) . . . 13
- 2.3 Elaboration of Hypotheses to Working Packages . . . 14
- 2.4 Technical Preparation of Working packages . . . 17

3 Impact of Terrain Configuration on Katabatic Flows 23
- 3.1 Introduction . . . 25
- 3.2 Model Set-up . . . 28
  - 3.2.1 Topography . . . 28
  - 3.2.2 Initialisation and Boundary Conditions . . . 29
  - 3.2.3 Physics . . . 30
- 3.3 Results . . . 31
  - 3.3.1 Development of Katabatic Flows . . . 31
  - 3.3.2 Impact of Topography . . . 36
- 3.4 Discussion . . . 42
- 3.5 Summary and Conclusions . . . 44

4 Katabatic Flows and the Formation of Convective Clouds 49
- 4.1 Introduction . . . 51
- 4.2 Methods . . . 52
  - 4.2.1 Frontogenesis . . . 52
  - 4.2.2 Model Set-up . . . 54

4.3 Results . . . 54
4.3.1 Density Current and Surface Front . . . 55
4.3.2 Atmospheric Environmental Parameters . . . 59
4.3.3 Formation of Convective Clouds . . . 61
4.4 Discussion . . . 68
4.5 Summary and Conclusions . . . 70

5 Nocturnal Convective Clouds at the Eastern Andes of South Ecuador 75
5.1 Introduction . . . 77
5.2 Data . . . 79
5.3 Model Set-up . . . 80
5.4 Results . . . 81
5.4.1 Convective Cloud Patterns . . . 81
5.4.2 Comparison of Observed and Simulated Cloud Patterns . . . 86
5.4.3 Analyses of Atmospheric Conditions . . . 87
5.4.4 Convective Cloud Development . . . 93
5.4.5 Katabatic Flows . . . 95
5.5 Discussion . . . 97
5.6 Summary and Conclusions . . . 100

6 Summary and Outlook 107
6.1 Summary . . . 107
6.2 Outlook . . . 109

Zusammenfassung 113

List of Figures

1.1 Outline of this work. Bold numbers on the left are chapter and section numbers 6

2.1 Conceptual design 15
2.2 Workflow of the technical preparation for WP1 - WP5 17

3.1 Schematic of an idealised katabatic flow (after Manins 1992) 25
3.2 Study area (left), target area (right) with coverage of the local area weather radar 26
3.3 Simplified terrain models: a) simple uniform slope (SLP), b) simple uniform valley (VAL), c) simple valley with an additional along-valley height gradient (VAL2), d) basin (BSN), e) basin with a drainage system (BSNV) 29
3.4 Vertical cross-section (*xz*-plots from $x = 3.0$ km, $y = 15.0$ km and $x = 17.0$ km, $y = 15.0$ km) of the potential temperature (*pt*, contour, K) and the wind field in *u*-*w* direction (vectors, m·s^{-1}) of SLP for time steps of (a) 3600 s and (b) 6900 s 32
3.5 Profiles of (a) the potential temperature (*pt)*, (b) the wind vector (u) and (c) the turbulent kinetic energy (TKE) for time steps of 3600 s and 6900 s taken at $x = 12.5$ km and $y = 15.0$ km 33
3.6 The heat energy fluxes in W·m^{-2} with the net radiation (Rn), the sensible heat flux (H), the latent heat flux (LE) and the ground heat flux (G) as a function of simulation time between 0 and 4 hours taken at $x = 12.5$ km and $y = 15.0$ km 35
3.7 Horizontal cross-section (*xy*-plot at $z = 50$ m above ground level) of the potential temperature (*pt*, shaded, K) and the wind field in *u*-*v* direction (vectors, m·s^{-1}) of BSN for time step 14,400 s 36
3.8 Horizontal cross-section (*xy* plot at $z = 50$ m above ground level) of the divergence field (DIV, shaded, s^{-1} amplified by a factor of 1000) of BSN for time step 14,400 s 37
3.9 Horizontal cross-section (*xy* plot at $z = 50$ m above ground level) of the pressure perturbation field (*pprt*, shaded, Pa) of BSN for time step 14,400 s 38

3.10 Horizontal cross-section (*xy* plot at $z = 50$ m above ground level) of the potential temperature (*pt*, shaded, K) and the wind field in *u*-*v* direction (vectors, m·s^{-1}) of BSNV for time step 14,400 s 39
3.11 Horizontal cross-section (*xy* plot at $z = 50$ m above ground level) of the divergence field (*DIV*, shaded, s^{-1} amplified by a factor of 1000) of BSNV for time step 14,400 s 40
3.12 Horizontal cross-section (*xy* plot at $z = 50$ m above ground level) of the pressure perturbation field (*pprt*, shaded, Pa) of BSNV for time step 14,400 s 41
3.13 Vertical cross-section (*xz* plot from $x = 50.0$ km, $y = 50.0$ km to $x = 79.0$ km, $y = 79.0$ km) of the divergence field (*DIV*, shaded, s^{-1} amplified by a factor of 1000) and the wind field in *u*-*w* direction (vectors, m·s^{-1}) of BSNV for time step 14,400 s 42

4.1 Topographical map (GTOPO30 data) of Southern Ecuador and the adjacent Peruvian Amazon basin displaying the target area and the location of the rain radar (left), a 3D view of the target area (lower right) and a 3D view of the simplified terrain (upper right) 51
4.2 Vertical cross-section (xz plots from x = 36.0 km, y = 36.0 km and x = 100.0 km, y = 100.0 km) of the wind speed in *u*-*w* direction (contour, blue, m·s^{-1}) and *TKE* (contour, red, m^2·s^{-2}) for time step 17100 s 55
4.3 Profiles of (a) the potential temperature (*pt)*, (b) the wind vector (*u*) and (c) the turbulent kinetic energy (*TKE*) taken at x = 24.5 km and y = 78.0 km for the time steps 4800 s and 17100 s 57
4.4 The heat energy fluxes in W·m^{-2} with the net radiation (*Rn*), the sensible heat flux (*H*), the latent heat flux (*LE*) and the ground heat flux (*G*) as a function of simulation time between 0 and 6 hours taken at x = 24.5 km and y = 78.0 km 57
4.5 Vertical cross-section (xz plot from x = 42.0 km, y = 42.0 km and x = 100.0 km, y = 100.0 km) of the potential temperature (*pt*, contour, blue, K) and the wind field in *w* direction (contour, red, m·s^{-1}) for time step 17100 s 58
4.6 Horizontal cross-section (xy plot at z = 50 m above ground level) of the divergence field (*DIV*, shaded, s^{-1} amplified by a factor of 1000) for time step 18000 s 60
4.7 Horizontal cross-section (xy plot at z = 50 m above ground level) of the Bulk Richardson Number (*BRN*, contour) for time step 19800 s . 62
4.8 Vertical cross-section (xz plot from x = 45.0 km, y = 45.0 km and x = 100.0 km, y = 100.0 km) of moisture convergence amplified by a factor of 1000 (*MC*, shaded, (g·kg^{-1})·s^{-1}), the wind field in *u*-*w* direction (vectors, m·s^{-1}) and the total condensed water (*TW*, solid line, g·kg^{-1}) for time steps a) 18000 s, b) 19800 s, c) 21600 s, d) 24600 s 63

4.9 Horizontal cross-section (xy plot at z = 200 m above ground level) of the initial wind field in *u*-*v* direction (vectors, m·s^{-1}) 65
4.10 Horizontal cross-section (xy plot at z = 50 m above ground level) of the Bulk Richardson Number (*BRN*, contour) for time step 2700 s . . 66
4.11 Vertical cross-section (xz plot from x = 45.0 km, y = 45.0 km and x = 100.0 km, y = 100.0 km) of moisture convergence amplified by a factor of 1000 (*MC*, shaded, (g·kg^{-1})·s^{-1}), the wind field in *u*-*w* direction (vectors, m·s^{-1}) and the total condensed water (*TW*, solid line, g·kg^{-1}) for time steps a) 900 s, b) 2700 s, c) 5400 s 67

5.1 South Ecuador and the adjacent Peruvian Amazon basin with the nested domain configuration (left), GOES-E image and location of the LAWR (upper right) and terrain of the study area (lower right) . 77
5.2 GOES-E brightness temperatures (10.2 - 11.2 μm, K) (a, d, g), ARPS brightness temperatures (K) (domain D3 b, e, h) ARPS brightness temperatures (K) (domain D4 c, f, i) with a white contour (220 K) for 2015 LST, 2115 LST and 2215 LST 83
5.3 GOES-E brightness temperatures (10.2 - 11.2 μm, K) (a, d, g), ARPS brightness temperatures (K) (domain D3 b, e, h) ARPS brightness temperatures (K) (domain D4 c, f, i) with a white contour (220 K) for 0115 LST, 0215 LST and 0315 LST 84
5.4 GOES-E brightness temperatures (10.2 - 11.2 μm, K) (a, d, g), ARPS brightness temperatures (K) (domain D3 b, e, h) ARPS brightness temperatures (K) (domain D4 c, f, i) with a white contour (220 K) for 0415 LST, 0615 LST and 0915 LST 85
5.5 Horizontal cross-section (xy-plot at z = 300 m asl) of the equivalent-potential temperature θ_e (*pte*, shaded, K) of a) subset of domain D3 equal to domain D4 and b) domain D4 for 1900 LST 88
5.6 Vertical cross-section (xz-plot at x = 38 km and y = 35 km, x = 170 km and y = 215 km) of the equivalent-potential temperature θ_e (*pte*, shaded, K) of a) domain D3 and b) domain D4 for 2015 LST 89
5.7 SkewT log P profiles a) domain D3 and b) domain D4 taken at -78.0° x -4.9° for 1900 LST 91
5.8 Horizontal cross-section (xy-plot at z = 300 m asl) of the divergence field (*DIV*, shaded, s^{-1} amplified by a factor of 1000) for a) subset of domain D3 equal to domain D4 and b) domain D4 for 1900 LST . . . 93
5.9 Vertical cross-section of domain D4 (xz-plot from x = 71 km, y = 80 km and x = 170 km, y = 215 km) of horizontal moisture convergence amplified by a factor of 1000 (*MC*, shaded, (g·kg^{-1})·s^{-1}), the wind field in *u*-*w* direction (vectors, m·s^{-1}) and the total condensed water (*TW*, solid line), g·kg^{-1} at a) 2000 LST, b) 2015 LST, c) 2030 LST and d) 2045 LST 94

5.10 Profiles of a) the wind vector (u, $\mathrm{m \cdot s^{-1}}$) and b) the turbulent kinetic energy (TKE, $\mathrm{m^2 \cdot s^{-2}}$) for 1900 LST and 2000 LST at -78.5° x -5.2° . 96
5.11 The heat energy fluxes in $\mathrm{W \cdot m^{-2}}$ with the net radiation (Rn), the sensible heat flux (H), the latent heat flux (LE) and the ground heat flux (G) as a function of time between 12 October 1300 LST and 13 October 1300 LST taken at -78.5° x -5.2° 97

List of Tables

2.1 Initial value settings and parametrisation schemes of ARPS 14

4.1 Environmental parameters 59

5.1 Grid configurations 80
5.2 Mesoscale convective complex definitions (as defined by Maddox (1980)) 82
5.3 Environmental parameters 92

List of Acronyms

ARPS	Advanced Regional Prediction System
AGL	Above Ground Level
AVHRR	Advanced Very High Resolution Radiometer
BSN	Basin
BSNV	Basin with Draining Valleys
CAM	Community Atmosphere Model
CAPS	Center for Analysis and Prediction of Storms
CLASS	Comprehensive Large Array Stewardship System
CRTM	Community Radiative Transfer Model
DEM	Digital Elevation Model
DFG	Deutsche Forschungs Gemeinschaft
DOE	Department of Energy
ECSF	Estacion Cientifica San Francisco
EL	Equilibrium Level
EUMETCast	EUMETSAT Broadcast System for Environmental Data
EUMETSAT	European Organisation for the Exploitation of Meteorological Satellites
GCM	General Circulation Model
GOES	Geostationary Operational Environmental Satellite
GVAR	GOES Variable format
IR	Infrared
LAWR	Local Area Weather Radar
LES	Large Eddy Simulation
Lidar	Light detection and ranging
LLJ	Low-level Jet
MCC	Mesoscale Convective Complex
MCS	Mesoscale Convective System
NCAR	National Center for Atmospheric Research
NCEP	National Centers for Environmental Prediction
NBL	Nocturnal Boundary Layer
NOAA	National Oceanic and Atmospheric Administration
NWP	Numerical Weather Prediction
PBL	Planetary Boundary Layer
Radar	Radio detecting and ranging

RAMS	Regional Atmospheric Modelling System
SALLJ	South American Low-level Jet
SALLJEX	South American Low-level Jet experiment
SLP	Slope
Sodar	Sonic detecting and ranging
USDA	United States Department of Agriculture
USGS	United States Geological Survey
UTC	Universal Time Coordinate
VAL	Valley
VAL2	Valley with Along Valley Inclination
WRF	Weather Research and Forecasting

List of Symbols

Symbol	Meaning	Units
α	Slope angle	$^\circ$
α_g	Albedo	
β	Along-valley angle	$^\circ$
γ	Lapse rate	$\mathrm{K{\cdot}m^{-1}}$
BRN	Bulk Richardson Number	
C_{dm}	Drag coefficient	
C_{dh}	Heat exchange coefficient	
$CAPE$	Convective Available Potential Energy	$\mathrm{J{\cdot}kg^{-1}}$
CIN	Convective inhibition	$\mathrm{J{\cdot}kg^{-1}}$
DIV	Divergence field	$\mathrm{s^{-1}}$
E	Entrainment coefficient	
E_g	Evaporation of soil surface	$\mathrm{(kg{\cdot}m^{-2}){\cdot}s^{-1}}$
E_r	Canopy water evaporation	$\mathrm{(kg{\cdot}m^{-2}){\cdot}s^{-1}}$
E_{tr}	Transpiration	$\mathrm{(kg{\cdot}m^{-2}){\cdot}s^{-1}}$
F	Frontogenetic function	
g	Gravitational force	$\mathrm{m{\cdot}s^{-2}}$
G	Ground heat flux	$\mathrm{W{\cdot}m^{-2}}$
h	Inversion depth	m
H	Sensible heat flux	$\mathrm{W{\cdot}m^{-2}}$
K_{hh}	Horizontal mixing coefficient	
K_{hv}	Vertical mixing coefficient	
LCL	Lifting Condensation Level	Pa
LE	Latent heat flux	$\mathrm{W{\cdot}m^{-2}}$
LFC	Level of Free Convection	Pa
LI	Lifted Index	
MC	Moisture convection	$\mathrm{(g{\cdot}kg^{-1}){\cdot}s^{-1}}$
pt	Potential temperature	K
$pprt$	Perturbation pressure	Pa
R_A	Incoming longwave radiation	$\mathrm{W{\cdot}m^{-2}}$
R_d	Gas constant	$\mathrm{(J{\cdot}mol^{-1}){\cdot}K^{-1}}$
Rn	Net radiation flux	$\mathrm{W{\cdot}m^{-2}}$
R_{sw}	Shortwave radiation	$\mathrm{W{\cdot}m^{-2}}$
T_s	Ground surface temperature	K
T	Temperature at first level above ground	K

Symbol	Meaning	Units
θ	Potential temperature	K
θ_e	Equivalent-potential temperature	K
θ_{env}	Ambient potential temperature	K
θ_{par}	Potential temperature of parcel	K
θ_0	Potential temperature at surface	K
t	Time	s
T_{LCL}	Temperature at lifting condensation level	K
T_{BB}	Temperature of black body	°C
TKE	Turbulent kinetic energy	$m^2 \cdot s^{-2}$
TW	Total condensed water	$g \cdot kg^{-1}$
σ	Stefan-Boltzmann constant	$(W \cdot m^{-2}) \cdot K^{-4}$
s	Slope distance	m
U	Downslope motion	$m \cdot s^{-1}$
u	Wind in u-direction	$m \cdot s^{-1}$
u'	Turbulent component of u	$m \cdot s^{-1}$
V	Wind speed	$m \cdot s^{-1}$
v	Wind in v-direction	$m \cdot s^{-1}$
v'	Turbulent component of v	$m \cdot s^{-1}$
w	Wind in w-direction	$m \cdot s^{-1}$
w'	Turbulent component of w	$m \cdot s^{-1}$
w_v	Mixing ratio of water vapour mass per mass of dry air	$g \cdot kg^{-1}$
z_{EL}	Height of EL	m
z_{LFC}	Height of LFC	m
z_{sfc}	Surface level	m

1 Introduction

Clouds and their resulting precipitation are part of the hydrological cycle. They represent important meteorological factors influencing energy, water and matter cycles in ecosystems (O'Brien, 2006). This allows them to greatly impact the zonation of flora and fauna. Hence, understanding clouds and rainfall formation is a key aspect in understanding the structure and functionality of an ecosystem and its biodiversity. Unfortunately, knowledge on cloud and rainfall dynamics is scarce, particularly in biodiversity hotspot areas of tropical mountains, such as the Andes of Ecuador (see figure 3.2).

In the tropics, most of the cloud formation over land is dominated by the diurnal cycle of solar radiation with a short time lag generating organised convection (Mapes et al., 2003; Poveda et al., 2004). Moisture convection is a key process in thermal energy dissipation and has remarkable effects on the tropical climate by affecting the global circulation as well as the local release of latent heat.

In the diurnal cycle, the incoming solar radiation causes land surface heating by diabatic processes, which lead to a destabilisation of the atmosphere and sufficient positive buoyancy, reaching its maximum in the afternoon. In order to dissipate this additional thermal energy, adiabatic processes initiate strong upward motion for the vertical transport of heat and moisture. With sufficient moisture in the atmosphere, convective clouds develop due to condensation processes. Thus, a rainfall peak in the late afternoon and evening, respectively, occurs in most instances (Gray and Jacobson, 1977; Kousky, 1980; Meisner and Arkin, 1987; Marengo, 1995; Yang and Slingo, 2001; Machado et al., 2002; Sato et al., 2009).

Beyond that, the cloud development and precipitation behaviour in South America is highly affected by the Amazon basin and the north-south oriented Andean mountain range. Large scale circulation patterns in the lower troposphere advance warm moist air into the Amazon basin, representing a great source of moisture (Garreaud, 1999). During the diurnal solar cycle, convective clouds develop in the afternoon with sufficient moisture in the atmosphere. When the atmosphere is very unstable, several isolated cumulus clouds merge into a cloud cluster. These so called mesoscale convective systems (MCS) persist for two to three days and produce strong rainfalls (Gray and Jacobson, 1995). They may be transported westwards if low and middle tropospheric easterlies prevail. In addition, besides this moisture transport into the Amazon, large scale circulation is the main contributor for the rainfall on the eastern Andean slopes. The low-level trade winds from the equatorial Atlantic with an easterly direction are deflected by the Andes to a northerly / northwesterly

direction and form the South American low-level jet (SALLJ) (Campetella and Vera, 2002; Gandu and Geisler, 1991; Virji, 1981; Marengo et al., 2002; Vera et al., 2006). The Andean mountains act as a barrier for the current, which is accelerated along the eastern flanks. In its exit region, MCSs are frequently generated due to a convergence of the wind field, which results in atmospheric instabilities and sufficient buoyant energy (Valesco and Fritsch, 1987).

Apart from these considerations, the air current also produces an increase of convective precipitation at the eastern flank of the Andes due to an enhancement of orographic lifting of air (Smith and Evans, 2007). Kirshbaum and Smith (2009) demonstrated the influence of the terrain on impinging trade winds. The orography forces conditionally unstable air to rise, initiating and intensifying strong convection. Vaile and Norte (2009) also point to the occurrence of strong low-level cross-barrier flows, which cause heavy orographic precipitations.

Furthermore, there are some modifications based on the local topographical situation. Killeen et al. (2007) investigated the relationship between the topography, wind field and precipitation in the eastern Andes. The author differentiated three spatially separate regions, a super-humid, humid and a dry region, which result from the atmospheric circulations and the local circulations created by the complex topography. The very steep slopes and valleys of the Andes cause spatially varying heating effects, which induce thermally-driven local circulation patterns such as mountain-valley breezes and luv-lee effects (Garreaud and Wallace, 1997; Lenters and Cook, 1995). Those small-scale features, determined by an interaction of the complex Andean terrain and solar radiation, yield a higher variability in the spatial cloud formation and precipitation distribution.

During the day, the insolation produces differentially heated slopes, which cause local boundary-layer convergences. An ascending of air along these slopes enhances convective processes, which result in cloud generation and precipitation peaks at higher elevations in the late afternoon. During the night time, however, descending of air occurs due to radiation loss, inducing cold pools and the formation of ground fog. Since the downslope of cold air creates an inversion layer near the surface, convective activities are usually inhibited (Defant, 1949; Barry, 2008; Whiteman, 2000). However, strong nocturnal precipitation events as a result of nocturnal convective processes occur in the tropics, but are often not exactly defined and hitherto poorly investigated.

1.1 Motivation

The biodiversity of a megadiverse ecosystem in the eastern Andes of South Ecuador in the Rio San Francisco Valley is examined in the framework of an ecological research project, the DFG Research unit 816. Ecuador, which is located on the northwest coast of South America and traversed by the central Andes (see figure 3.2), is a rich biological region and known as a hotspot for biodiversity (Myers et al., 2000).

The high incoming solar radiation as well as the moisture transport from the Amazon, which ensures a high amount of water availability, offer outstanding conditions for vegetation growth. In addition, the great altitudinal gradient at the eastern slopes, with a maximum height difference of approximately 4000 m between the Amazon and the mountains, adds further diversity along the height gradient. The climate in Ecuador, which significantly affects all biotic and abiotic factors in the ecosystem, is mainly determined by the previously described interaction between the complex terrain of the Andes and the Amazon basin. For this reason, several climate parameters were measured in our study area to observe their behaviour on the eastern flanks of the Andes. Precipitation measurements were made and are continued using automatic climate stations and an X-band local area rain radar (LAWR) system (Rollenbeck and Bendix, 2006a) to understand the rainfall dynamics and their influence on the vegetation in such complex terrain.

The observed data exhibit the typical diurnal cycle of tropical rainfall, with maximum precipitation in the late afternoon and evening. However, several studies also point to regional differences in this diurnal cycle (Bendix et al., 2006a, 2008b,a). In consideration of different exposed slopes and valleys, small scale circulation patterns develop in connection with insolation. Richter (2003) showed differentiated precipitation distributions according to luv-lee effects and mountain-valley breezes in the area of the Rio San Francisco Valley. Rollenbeck et al. (2006); Rollenbeck and Bendix (2006b) presented impacts on the spatial variability of rainfall by interactions of the orography with the prevailing winds. The studies illustrated that the complex Andean mountains significantly affect the spatial cloud formation and rainfall distribution, with special regards to the altitudinal gradient.

Moreover, monitoring the climate system in the Rio San Francisco Valley revealed an unexpected precipitation event. In addition to the late afternoon peak, the measurements recorded a secondary rainfall peak, which occurs in the early morning hours around 11:00 to 12:00 UTC (Bendix et al., 2006b). An analysis of the maximum rain rates suggested convective or mixed rain events. The peak was identified as a strong pre-dawn precipitation occurrence rather than nocturnal stratiform rainfall. These events were traced back to mesoscale instabilities southeast of southern Ecuador on the basis of two case studies. Visual analysis of Geostationary Operational Environmental Satellite (GOES) infrared (IR) satellite data revealed the appearance of an MCS in the adjacent Peruvian Amazon basin. An additional analysis of the corresponding cloud top heights was made using NOAA-AVHRR data. They disclosed a maximum height of over 8 km, which lead to the conclusion that the peak is produced by strong nocturnal convection. Furthermore, the nocturnal occurrence of the MCS at the eastern foothills of the Andes southeast of South Ecuador was verified using cloud-top temperature distributions of the GOES-IR images (Bendix et al., 2009). The frequency of their formation is captured in a statistical study on the basis of typical characteristics, which are detectable in the satellite data. Additionally, a relation between the nocturnal MCS and the measured early morning

rainfalls in the Rio San Francisco Valley is detected. Nevertheless, the atmospheric processes accounting for the MCS generation are not available and only assumed.

Some authors who also detected such nocturnal rainfall made the connection between nocturnal rainfalls and low tropospheric flow systems. Garreaud and Wallace (1997) pointed out that nocturnal rainfall presumably occurs due to enhanced low-level convergence as a result of the nocturnal circulation between the Andes and the Amazon region. Mapes et al. (2003) found evidence that gravity waves radiating eastwards from a stable stratified Andean mixed layer promote nocturnal precipitation in the foothill area. Angelis et al. (2004) described the convergence of cold katabatic flows from the Andes and the Amazon warm pool, where katabatic flows induce low-level instability by acting as a cold front. In the scope of the South American Low Level Jet experiment (SALLJEX), the formation of MCSs at the exit region of the SALLJ (20° - 40° S) were examined. However, LLJs in the eastern Andes occur north of the equator, bringing warm moist air from the tropical Atlantic and the western Caribbean sea close to the equator (Vernekar et al., 2003). Nevertheless, the processes responsible for the strong nocturnal convection in a rather stable, as opposted to an unstable atmosphere, resulting in the pre-dawn rainfalls in our research area, are still unexplained.

1.2 Aims and Outlines

The purpose of the presented work is to investigate the underlying processes resulting in nocturnal clouds in the eastern Andes of South Ecuador mentioned in section 1.1. With reference to the presented context of observed nocturnal cloud formations and low-tropospheric flow systems, one feasible explanation is an interaction of nocturnal cold air drainage from the Andean slopes and valleys with the Amazonian warm pool. Those interactions account for an atmospheric destabilisation in the foothills. Given that there is sufficient moisture in the atmosphere, convective clouds develop. Furthermore, the specific terrain configuration in the cloud formation area with its quasi-concave geometry adds an additional factor to this condition. It reinforces the destabilisation of the atmosphere by additional low-level convergence, which facilitates an ascending of air. Apart from this contemplation, another low-tropospheric current is considered: a nocturnal low-level jet, which frequently evolves with the eastern Andes acting as a barrier. At their exit region they also enhance low-level convergence, resulting in atmospheric instabilities that are beneficial for deep convection. Based on these presumptions, the central theses of this study are:

H1 Katabatic flows from the east Andean slopes and valleys confluence at the foothills due to the geometry of the Andean terrain

H2 Katabatic flows induce a local surface cold front in the Peruvian Amazon basin

H3 Due to the Andean terrain configuration, a convergence induces moisture convection and the generation of convective clouds; a low-level jet at the eastern flanks of the Andes fosters this cloud formation process

Accordingly to the central thesis, the aims of the presented work are:

- To design a specific model of katabatic flows to analyse their modifications by the terrain
- To amplify this model for the analysis of katabatically induced cold fronts and compressional lifting with subsequent cloud cluster formation and to analyse the effects of a LLJ on cloud occurrence
- To demonstrate this final specific model in a case study of a chosen MCS event

Current difficulties in this investigation are:

- The highland-lowland interaction resulting in strong nocturnal convection is not fully understood, particularly in South Ecuador
- Until now, satellite data are the only source for validation data on the occurrence of the nocturnal MCS
- The cloud formation process is only available as a hypothesised procedure

The investigations of these nocturnal convective activities will be a useful and valuable advancement in understanding the functionality of a megadiverse mountain ecosystem. Figure 1.1 presents the structure of this work, starting in chapter 2 with the conceptual design. After a brief overview of detecting and analysis methods, the theoretical basis for the hypothesised mechanism is introduced with a review of numerical grid box models. Section 2.3 elaborates of the hypotheses of working packages, which follows their technical preparation.

The core of this study, i.e. the implementation of the working packages, is embedded in the following publications: First, the accurate simulation of katabatic flows and the impact of the terrain is embedded in 'Trachte, K., T. Nauss and J. Bendix, 2010: The Impact of Different Terrain Configurations on the Formation and Dynamics of Katabatic Flows: Idealised Case Studies, Boundary Layer Meteorology, 134, 2, 307-325' (chapter 3). The initiation of a cold front with subsequent MCS formation and the influence of a LLJ on cloud development is embedded in the manuscript 'Trachte, K., and J. Bendix: Katabatic Flows and Their Relation to the Formation of Convective Clouds - Idealised Case Studies', which is submitted to Journal of Applied Meteorology and Climatology (chapter 4). Finally, a first guess on the basis of model data compared with satellite data and a review of the hypothesised mechanism is presented in the publication 'Trachte, K., R. Rollenbeck, and J. Bendix, 2010: Nocturnal Convective Cloud Formation under Clear-sky Conditions at the Eastern Andes of South Ecuador, Journal of Geophysical Research, DOI:10.1029/2010JD014146' (chapter 5). Concluding remarks and summary are given in chapter 6, followed by a short outlook.

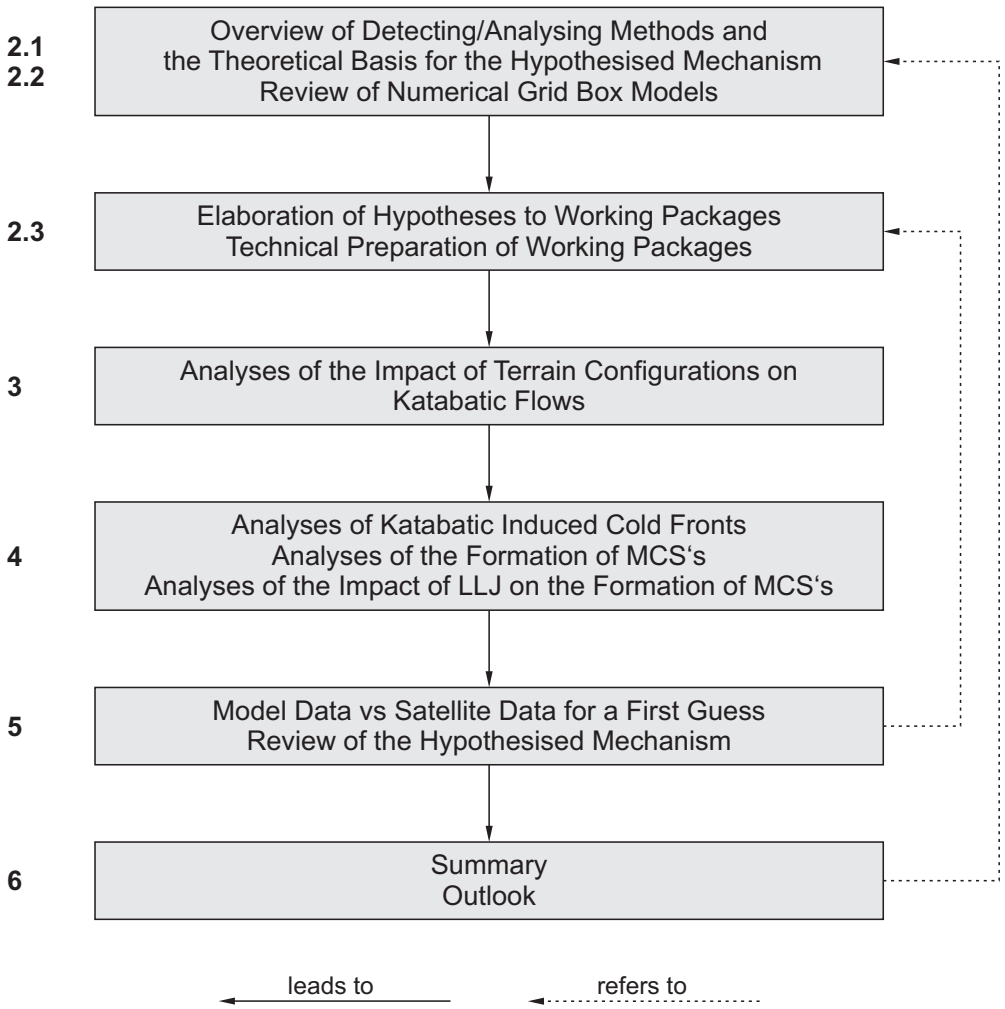

Figure 1.1: Outline of this work. Bold numbers on the left are chapter and section numbers

References

Angelis CF, McGregor GR, Kidd C (2004) A 3 year climatology of rainfall characteristics over tropical and subtropical south america based on tropical rainfall measuring mission precipitation radar data. Int J Climatol 24:385,399

Barry RG (2008) Mountain Weather and Climate. Cambridge University Press, University of Colorado, Boulder, 512 pp

Bendix J, Rollenbeck R, Goettlicher D, Cermak J (2006a) Cloud occurrence and cloud properties in ecuador. Clim Res 30:133 – 147

Bendix J, Rollenbeck R, Reudenbach C (2006b) Diurnal patterns of rainfall in a tropical andean valley of southern ecuador as seen by a vertical pointing k-band doppler radar. Int J Climatol 26:829–846

Bendix J, Fabian P, Emck P, Richter M, Beck E (2008a) Temporal heterogeneties - climate variability. Gradients in a tropical mountain ecosystem of Ecuador, Ecol Stud 198:281–290

Bendix J, Richter M, Fabian P, Emck P (2008b) Gradual changes along the altitudinal gradients - the climate. Gradients in a tropical mountain ecosystem of Ecuador, Ecol Stud 198:Springer, 63 – 73

Bendix J, Trachte K, Cermak J, Rollenbeck R, Nauss T (2009) Formation of convective clouds at the foothills of the tropical eastern andes (south ecuador). J Appl Meteorol 48:1682–1695

Campetella CM, Vera CS (2002) The influence of the andes mountains on the south american low-level flow. Geophys Res Lett 29

Defant F (1949) Zur theorie der hangwinde, nebst bemerkungen zur theorie der berg- und talwinde. Arch Meteorol Geophys Bioklim A1:421–450

Gandu AW, Geisler JE (1991) A primitive equations model study of the effect of topography on the summer circulation over tropical south america. J Atmos Sci 48:1822 – 1836

Garreaud RD (1999) Multiscale analysis of the summertime precipitation over the central andes. Mon Wea Rev 105:901 – 921

Garreaud RD, Wallace JM (1997) The diurnal march of convective cloudiness over the americas. Mon Wea Rev 125:3157 – 3171

Gray WM, Jacobson JRW (1977) Diurnal variations of deep cumulus convection. Mon Wea Rev 105:1171 – 1188

Gray WM, Jacobson JRW (1995) Diurnal variations of deep cumulus convection. Mon Wea Rev 105:1171 – 1188

Killeen TJ, Douglas M, Consiglie T, Jorgensen PM, Mejia J (2007) Dry spots and wet spots in the andean hotspot. J Biogeogr 34:1357 – 1373

Kirshbaum DJ, Smith RB (2009) Orographic precipitation in the tropics: Large-eddy simulations and theory. J Atmos Sci 66:2559 – 2578

Kousky VE (1980) Diurnal rainfall variations in northeast brazil. Mon Wea Rev 108:488 – 498

Lenters JD, Cook KH (1995) Simulation and diagnosis of the regional summertime precipitation climatology of south america. J Clim 8:2988 – 3005

Machado LA, Laurent H, Lima AA (2002) Diurnal march of the convection observed during trmm-wetamc/lba. J Geophys Res 107

Mapes BE, Warner TT, Xu M, Negri AJ (2003) Diurnal patterns of rainfall in northwestern south america. part i: Observation and context. Mon Wea Rev 131:799 – 812

Marengo JA (1995) Interannual variability of deep convection over the tropical south america sector as deduced from isccp c2 data. Int J Climatol 15:995 – 1010

Marengo JA, Douglas MW, Dias PLS (2002) The south american low-level jet east of the andes during the 1999 lba-trmm and lba-wet amc campaign. J Geophys Res 107:–

Meisner BM, Arkin PA (1987) Spatial and annual variations in the diurnal cycle of large-scale tropical convective cloudiness and precipitation. Mon Wea Rev 105:2009 – 2032

Myers N, Mittermeier RA, G MC, da Fonseca GAB, Kent J (2000) Biodiversity hotspots for conservation priorities. Nature 403:853 – 858

O'Brien EM (2006) Biological relativity to water-energy dynamics. J Biogeogr 33:1868–1888

Poveda CF, McGregor GR, Kidd C (2004) A 3 year climatology of rainfall characteristics over tropical and subtropical south america based on tropical rainfall measuring mission precipitation radar data. Int J Climatol 24:385,399

Richter M (2003) Using plant functional types and soil temperatures for eco-climatic interpretation in southern ecuador. Erdkunde 57:161 – 181

Rollenbeck R, Bendix J (2006a) Experimental calibration of a cost-effective x-band weather radar for climate ecological studies in southern ecuador. Atmos Res 79:296 – 316

Rollenbeck R, Bendix J (2006b) Variability of precipitation in the reserva biologica san francisco / souther ecuador. Lyonia 9:43 – 51

Rollenbeck R, Fabian P, Bendix J (2006) Precipitation dynamics and chemical properties in tropical mountain forests of ecuador. Adv Geosci 6:73 – 76

Sato T, Miura H, Satoh M, Takayabu YN, Wang Y (2009) Diurnal cycle of precipitation in the tropics in a global cloud-resolving model. Mon Wea Rev 22:4809 – 4826

Smith RB, Evans JP (2007) Orographic precipitation and water vapor fractionation over the southern andes. J Hydrometeor 8:3 – 19

Vaile M, Norte FA (2009) Strong cross-barrier flow under stable conditions producing intense winter orographic precipitation: A case study over the subtropical central andes. J Geophys Res 24:1009 – 1031

Valesco I, Fritsch JM (1987) Mesoscale convective complexes in the americas. J Geophys Res 92:9591 – 9613

Vera C, Baez MD, Emmanuel CB, Marengo J, Meitin J, Nicolini M, Nogues-Paegle J, Paegle J, Penalba O, Salio P, Silva Dias MA, Zipser E (2006) The south american low-level jet experiment. Bul Am Meteor Soc 87:63 – 77

Vernekar AD, Kirtman BP, Fennessy MJ (2003) Low-level jets and their effects on the south american summer climate as simulated by the ncep eta model. J Clim 16:297 – 311

Virji H (1981) A preliminary study of summertime tropospheric circulation pattern over south america estimated from cloud winds. Mon Wea Rev 109:599 – 610

Whiteman CD (2000) Mountain Meteorology. Oxford University Press, Oxford, 355 pp

Yang GY, Slingo J (2001) The diurnal cycle in the tropics. Mon Wea Rev 129:784 – 801

2 Conceptual Design

This chapter presents the conceptual design of the investigation of the hypothesised mechanism in the eastern Andes of South Ecuador and the northern Peruvian Amazon. The first section provides a brief overview of common methods for studying cloud appearances and katabatic flows. The overview is followed by a description of the applied method, the application of a numerical gridbox model to investigate the regarding processes. Finally, the working packages, including the essential simulations required to verify the hypotheses, are described.

2.1 Detecting and Analysing Methods

The assumed mechanism described in the three hypotheses introduced in chapter 1 consists of four main meteorological aspects: katabatic flows by radiative cooling, a cold front in the basin within the lower troposphere, the subsequent initiation of deep convection and the formation of a convective cloud cluster within the lower and middle troposphere. Several approaches are available in order to observe and analyse these processes.

Generally, remote sensing satellite data are used to monitor the appearance of various clouds such as MCS and track their movements. The data are also used for investigations of cloud properties. Modern retrieval techniques provide various information about clouds and their potential precipitation behaviour. A first appraisal of their characteristics can be obtained from the macrophysical cloud properties and classification algorithms (Bankert et al., 2009). The convective and stratiform regions of a cloud cluster can be differentiated using infrared (IR) blackbody temperatures. Microphysical properties (e.g. liquid water path, optical depth) can be derived with an approximation of radiation transfer models (Kuligowski, 2002; Trigo and Viterbo, 2003; Ba and Gruber, 2001). However, the detection of a convective cloud does not reveal the underlying processes resulting in its formation. In particular situations, the initiation of moisture convection is still unexplained, making it integral to retrieve these data from satellite data.

Further information on the vertical structure of the cloud can be obtained using cloud radar (radio detecting and ranging) systems. The radar affords information about cloud parameters such as cloud top and cloud base and offers additional insight into the cloud particles. But even radar does not disclose the reasons for the initiation of cloud formations.

More details on the atmospheric processes and conditions are provided by parameters such as air temperature, relative humidity and wind velocity, which can be obtained by a measuring network consisting of different instruments. A distinction is made between direct and indirect measuring methods, providing an extensive pool of information.

In the light of the hypothesised mechanism (section 1.2), the detection of katabatic flows and the analysis of the stability of the atmosphere's vertical structure is of great importance. The primary observational tool to observe katabatic flows is a sodar (sonic detecting and ranging) system (Doran and Horst, 1982; Gudiksen et al., 1992; Poulos and Bossert, 1995). It provides a continuous monitoring of the flow structure and records the twice daily thermally-induced transitions. Ambient atmospheric conditions, as well as its vertical structure are detected using a sequential tethered balloon ascent. They offer the determination of the height of the inversion, and thus that of the katabatic layer. Detailed information about the properties of the katabatic flow are achieved by micrometeorological towers placed along slopes and valleys, creating a trajectory. The tower mounted instruments measure wind velocity, temperature, relative humidity, and air pressure in the lower troposphere (Whiteman et al., 2010). The described observational tools, however, offer only point measurements, and thus have to be placed strategically along slopes and valleys. Additionally, the instruments depend on calibrations and services and need good quality control to obtain satisfying results. From that point of view, those tools provide the required data, but are difficult to operate and in place, especially in highly complex terrain.

In light of the introduced methods and their qualities, state-of-the-art atmospheric numerical gridbox models are useful tools to disentangle the reasons for specific cloud development in such a large and complex area (Behrens, 2006; Jacobson, 2005; Kalnay, 2002). They are based on the physical laws of the conservation of momentum, mass and thermal energy that are derived from empirical studies. The application of numerical gridbox models embraces processes across different spatio-temporal scales, and thus enables the investigation of the hypothesised mechanism.

2.2 Numerical Gridbox Models

Numerical gridbox models are available in a wide variety of spatial and temporal scales, making them useful in a variety of applications. Gridbox models can be used for analyses of large-scale as well as small-scale weather phenomena for restricted areas. For example, the radiation processes associated with surface energy fluxes affect local heating and cooling effects. This in turn may result in modifications of the horizontal wind field and the initiation of convective activities. The coherent estimations of the atmospheric processes are defined and conditioned by a three dimensional grid for a determined domain. This grid determines the resolution of the simulations and thus the explicitly and parameterised processes.

Due to their limited area, gridbox models require boundary conditions that define atmospheric conditions such as pressure, temperature, moisture and wind field. Because gridbox models simulate limited areas, comprehensive atmospheric processes can be considered. Features such as the terrain can be described in greater detail, depending on the horizontal resolution of the grid. This enables the consideration of regional to local atmospheric events that are of importance in the presented study. Primarily, the accuracy of a simulation depends on its parametrisation as well as the initial values, which can be provided by atmospheric soundings, coarser model results or defined conditions.

Generally, the application of a gridbox model affords the possibility to examine atmospheric processes in two types of approaches: ideal studies and real studies. Ideal simulations make it possible to analyze isolated atmospheric processes without considering the surrounding environment. The purpose of such investigations is the analysis of structures with determined processes while neglecting nonrelevant conditions. For example, Poulos et al. (2000) investigated the interaction of katabatic flows and mountain waves in an idealised study. The authors simulated the processes in isolated cases in order to identify both during their interaction. Petersen et al. (2003) simulated flows impinging on large idealised mountains to examine the impact of the mountain on the flow far downstream to explain resulting processes.

Real case simulations are intended to reproduce the atmosphere with the most exact approximate result. They are applied in real-time weather forecasts and as operational numerical weather prediction (NWP) systems.

In this study, a numerical gridbox model is used to investigate the underlying processes of the hypothesised mechanism. A range of state-of-the-art numerical models are available for atmospheric research, among others RAMS (Regional Atmospheric Modelling System, (Pielke, 1992)), CAM (Community Atmosphere Model, (Collins and Rasch, 2004)), WRF (Weather Research and Forecasting Model, (Skamarock et al., 2008)), and ARPS (Advanced Regional Prediction System, (Xue et al., 1995, 2000, 2001)).

2.2.1 Advanced Regional Prediction System (ARPS)

The numerical grid box model ARPS is an effective tool in studying atmospheric dynamics on the mesoscale (dx = 5 to 15 km, 0 to 12 hours), on the stormscale (dx = 1 to 3 km, 0 to 6 hours) and on the microscale (dx = 0.1 to 0.5 km, 0 to 1 hour), encompassing the atmospheric processes across these scales. It can be applied in basic atmospheric research and operational numerical weather prediction from the regional to the micro-scale. Further, ARPS is suitable for a wide range of idealised studies, such as analyses of mountain waves and storm development. Thus, it is designed to investigate atmospheric phenomena in both ideal and approximately real settings that require a flexible and general dynamic framework implemented as follows: ARPS has a terrain-following coordinate system equal in x- and y-direction

and a variable z-grid with several stretching option. The non-hydrostatic and fully-compressible equations are solved on an Arakawa C-grid. ARPS provides various options for lateral boundary conditions (e.g. periodic, rigid, zero-gradient, radiation open and externally-forced) as well as for the top and bottom boundaries (e.g. rigid, zero-gradient, top-radiation with Rayleigh sponge layer). For the dynamics a second- and fourth-order advection and a second- and fourth-order computational mixing is available. In addition, ARPS offers various sophisticated physics, some of them are addressed in table 2.1. Details are given in Xue et al. (1995, 2000, 2001). The model is chosen to investigate the reason for nocturnal cloud formation based on those summarized characteristics.

Table 2.1: Initial value settings and parametrisation schemes of ARPS

	Setting / Scheme
Initial atmospheric conditions	3D data fields, sounding
Microphysics	Kessler warm-rain, WRF WSM6 scheme, three-category ice Lin scheme
Cumulus	Kuo scheme, Betts-Miller-Janjic scheme, Kain-Fritsch scheme
Turbulence	Constant mixing coefficent, Smagorinsky mixing coefficient, 1.5-order TKE turbulent mixing
Soil	Two-layer and multi-layer soil model
Vegetation	Static land cover descriptors

2.3 Elaboration of Hypotheses to Working Packages

In order to validate the mechanism stated in section 1.2, the hypotheses H1, H2 and H3 (section 1.2) have to be elaborated to working packages required for the examination. An overview of the conceptual design of this work is given in figure 2.1, describing the coherency of the hypotheses and the respective working packages: the mechanism with and without location information, which implies neglecting the geographical reference to the eastern Andes and their environmental specifications for the right box of figure 2.1.

Several engaging processes of different temporal and spatial scales have to be taken into account in order to examine the hypotheses. A numerical study of the nocturnal formation of an MCS event in the eastern Andes can lead to difficulties in identifying the individual underlying processes and their relationship to the cloud cluster. A useful approach is the idealisation of respective phenomena, as mentioned in section 2.2. For the particular processes, optimal atmospheric and environmental conditions are created for each relevant aspect. In doing so, the location information is excluded, resulting in the following hypotheses:

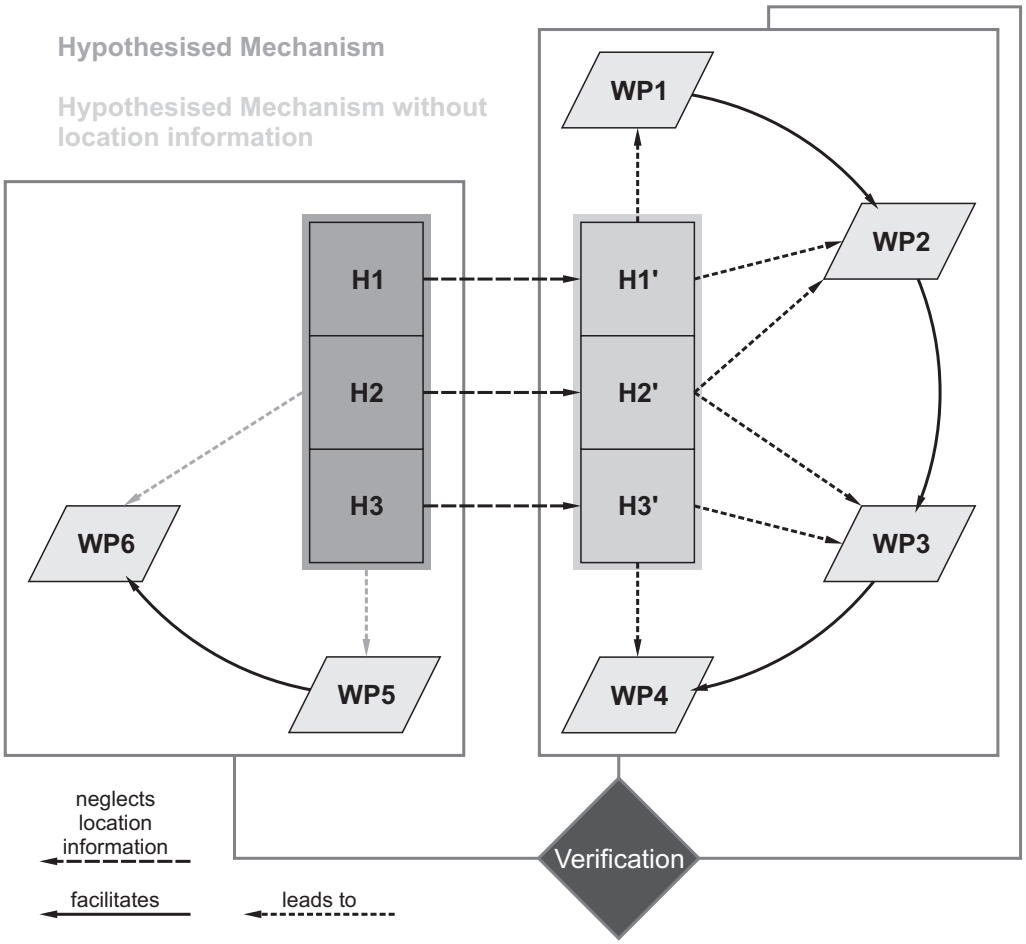

Figure 2.1: Conceptual design

H1' Katabatic flows from slopes and valleys confluence due to the geometry of the terrain

H2' Katabatic flows induce a surface cold front in a basin

H3' The terrain configuration causes a convergence to induce moisture convection and the generation of convective clouds; a low-level jet fosters this cloud formation process

The method enables general conclusions regarding the features involved and their interaction, which facilitates conclusions about the feasibility of the hypothesised procedures through a successive construction of the essential meteorological aspects.

Before elaborating the hypotheses on the respective working packages, the following preliminary considerations have to be taken into account. The driving atmospheric feature in the assumed mechanism describing the initiation of convection are katabatic flows, which implies it is curically important to accurately simulate

them. The flow develops only in the lowest one-hundred meters of the atmosphere in the nocturnal boundary layer (NBL) driven by turbulent surface fluxes. Convective cloud formation processes compared with this require an extension of the troposphere of approximately 18 km. Therefore, an adequate model framework has to be prepared to properly embrace this small-scale feature in the entire cloud formation process. The configuration of the terrain is another central aspect, because without an inclination, only stationary cold pools develop. The complex Andean terrain has to be abstracted, since a great height difference produces an overestimation of the wind field calculation (Bossert and Poulos, 1995) while using a very high vertical resolution near the surface and a correspondingly high horizontal resolution. The downslope motion is closely linked to an increase in the pressure field following the temperature gradient and has its maximum at the foot of the slope. The slope angle increases with increasing pressure, which finally results in unrealistic upward motions. To avoid these inaccuracies, which disguise the real process, simplified geometries are necessary.

As a result, the working packages to review H1', H2' and H3' are, respectively, as follows:

WP1 Design of a specific model for katabatic flows. This is to assure an accurate flow that is controlled by established theoretical definitions, measurement campaigns and model studies.

WP2 Analyses of the configuration of the terrain on the behaviour of katabatic flows. The objective is the demonstration of the confluence of the flow due to the shape of the terrain.

WP3 Analyses of the occurrence of a surface cold front and the consequent formation of a MCS. The aim is to prove that the katabatic flow induces an atmospheric gradient and that its confluence results in compressional lifting with moisture convection given, that sufficient water vapour is available.

WP4 Analyses of the influence of a LLJ on the formation of the MCS. The purpose is to determine whether the jet is the reason or an additional trigger function for MCS formation.

After successfully verifying the hypothesised mechanism without location information (see figure 2.1), the location is enabled. The mechanism (H1 to H3) is then analyzed in the eastern Andes of south Ecuador by using a test case, which is validated on the basis of a comparison of the modelled data with observed data and results of WP1 to WP4 to strengthen their evidence.

WP5 Analysis of a MCS event in the foothills of the Andes in the Peruvian Amazon basin. The aim of this test is to determine whether the hypothesised mechanism is maintained in the geographic area under approximately realistic conditions.

WP6 Evaluation of the results of the MCS event based on modelled and observed cloud properties. The objective of this step is to confirm the nocturnal cloud cluster in the eastern Andes driven by converging katabatic flows.

2.4 Technical Preparation of Working packages

The previous section elaborated the respective working packages. Figure 2.1 shows a clear separation between H1' to H3' and H1 to H3, demonstrating the mechanism without and with location information. Here, their technical preparation is described, as illustrated in figure 2.2. It shows the relevant aspects of the numerical study with its sequential construction, creating a 'circular' closure back to the beginning. The numerical study and its evaluation are clearly separated, so that WP6 is exclude in figure 2.2.

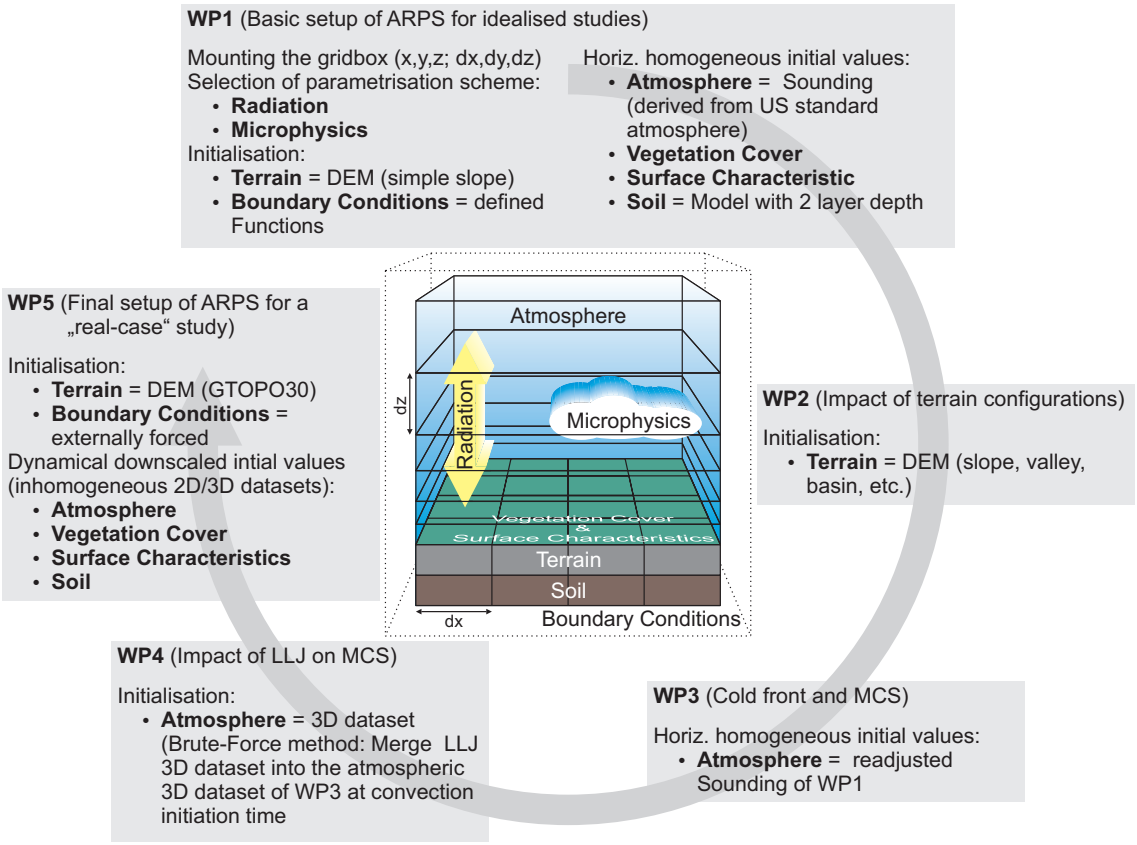

Figure 2.2: Workflow of the technical preparation for WP1 - WP5

WP1 Apart from a very high vertical resolution and an accordingly high horizontal resolution to design a model for katabatic flows, the selection of the parametrisation

schemes and the initialisation of ARPS are important issues (see Figure 2.2). Of particular interest are the radiation transfer, the soil and vegetation model as well as the surface characteristics. The boundary conditions are defined with determined functions. The initial values for the atmosphere to produce the flow, which are horizontally homogeneously arranged to the grid box, are provided by a sounding. Middle and upper wind fields and possible cloud developments are prevented by isolating the katabatic flow through a zero wind field and a zero atmospheric moisture content. Since a simple slope is the basic feature in studying katabatic flows, it is used to demonstrate the accurate simulation of the flow. Relevant criteria controlling the correctness of the simulation results are derived from the Manins and Sawford hydraulic model (Manins and Sawford, 1979) and descriptions of Petkovsek and Hocevar (1971) and Mahrt (1982), amongst others. The key aspect in this process is the objective evidence of the katabatic flow based on typical characteristics such as a jet-like wind profile, a surface inversion layer representing the katabatic layer and a net radiation loss creating a buoyancy deficit. If these qualifications are fulfilled, ARPS represents the appropriate processes accurately with the used model set-up.

WP2 The simple slope is replaced by different configurations in order to analyse the impact of the terrain on katabatic flows (figure 2.2). ARPS offers an idealised terrain configuration for the application in mountain breezes, but the implemented function generates only simply shaped mountains or slopes. Considering the complex features of the Andes, with their irregular structure, those terrain geometries are inadequate for this investigation. Therefore, simplified digital elevation models (DEMs) inspired by the real structures of the Andes in the target area are generated (see figure 3.3 in chapter 3). The impact of its geometry on the dynamic behaviour of the katabatic flow is simulating using a gradual increase of the terrain complexity. In addition to the simple slope (WP1), a simple valley is used to show the accumulation of cold air in the valley floor. A channelling effect is generated with an additional along-valley inclination. Thus, besides the cross-valley flow, the along-valley flow transporting cold drainage air into the basin can be presented. To illustrate the influence of the terrain on the confluence of the flow, a ridgeline forming a uniform basin is used. Finally, the concave ridgeline is interrupted by six valleys to demonstrate the confluence despite a drainage system regime directed into the basin.

WP3 After the effectual demonstration of H1' with WP1 and WP2, the subsequent formation of a surface cold front and the formation of an MCS are analysed (figure 2.2) using the most complex terrain model from the previous study. This enables the analysis of the impact of specific relevant aspects, such as the effectiveness of moisture in the atmosphere. The initialising sounding applied in WP1 and WP2 returns sufficient water vapour for potential microphysical activities. First,

the katabatically induced cold front is controlled with typical features such as a temperature / density gradient, a horizontal convergence zone and an inclination of isotherms. The subsequent initiation of moisture convection through a compressional lifting due to the shape of the terrain is revelaed by characteristics such as a buoyant plume with accelerating wind velocities and the organisation of convective cells in an ensemble. These relevant criteria are obtained from established studies from (Eliassen, 1959; Maddox, 1983; Rutledge, 1991; Houze, 2004) amongst others and are used to evaluate the simulation results.

WP4 In order to examine the influence of a LLJ on the formation of the MCS, a method has to be developed combining both a katabatically induced cold front and the occurrence of a LLJ. This is realised by merging a 3-D data set of a LLJ into the existing 3-D data set of WP3 just before the convective initiation time. Since there are several definitions for the development of nocturnal LLJs (Blackadar, 1957; Holton, 1967; Bonner, 1968), only the occurrence of this low-tropospheric current is included. Characteristics such as maximum wind velocity and vertical wind shear are considered. The influence of the jet on MCS development is examined by comparison with the previous results.

WP5 After the hypothesised mechanism has been reproduced without location information, the validity of H1', H2' and H3' is analysed on the basis of a sample situation of a nocturnal MCS event in the target area (figure 2.2). The properties and findings of the idealised study are assigned to the geographical area to be examined, i.e. the eastern Andes of Ecuador. In this instance, the designed model framework is substituted with an approximately realistic model setting using the same adjusted physics. The prepared optimal conditions of WP1 to WP4 are replaced by measurement data and parameters: the simplified DEM is changed by suitable terrain data such as the GTOPO30 data representing the Andes. The atmospheric initial values are provided by reanalysis data consisting of a 2- and 3-D data set that is inhomogeneously arranged to the grid box through dynamic downscaling. Thus they represent the externally-forced lateral boundary conditions, while the top and bottom boundaries remain unchanged. For the consideration of the soil and vegetation the two-layer soil model is used, initialised with suitable data such as the USGS input data.

WP6 Finally, the results of WP 5 are verified with remote sensing satellite data. A first appraisal of the simulated cloud occurrence is given by comparing satellite-observed brightness temperatures from the GOES-E imagery with the modelled data. In doing so, criteria such as the size of the cluster, the minimum brightness temperature of the interior area and the orientation of the MCS are of particular interest. Beyond that, the knowledge gained in the idealised study afford a basis for comparison. Determined features crucial for the corresponding process derived

from the previous study are used to identify the corresponding small scale processes. For example, katabatic flows and their correct representation are controlled by their typical characteristics and their thermal inducement is proved by the surface heat budget as in WP1. Based on such a backtrace, the converging katabatic flow can be confirmed as the driving mechanism behind the cloud formation. Thus, the idealised study of the hypothesised mechanism without a spatial location represents an additional reference for the evaluation of the underlying process in the real-case study.

References

Ba MB, Gruber A (2001) Goes multi-spectral rainfall algorithm (gmsra). J Appl Meteorol 40:1500 – 1514

Bankert RL, Mitrescu C, Miller SD, Wade RH (2009) Comparison of goes cloud classification algorithms employing explicit and implicit physics. J Appl Meteorol Climatol 48:1411 – 1421

Behrens J (2006) Adaptive Atmospheric Modeling: Key Techniques in Grid Generation, Data Structures, and Numerical Operations with Applications (Lecture Notes in Computational Science and Engineering). Springer, Berlin, 214 pp

Blackadar AK (1957) Boundary layer wind maxima and their significance for the growth of nocturnal inversions. Bull Amer Meteorol Soc 38:283 – 290

Bonner WD (1968) Climatology of the low-level jet. Mon Weather Res 96:833 – 850

Bossert JE, Poulos GS (1995) A numerical investigation of mechanisms affecting drainage flows in highly complex terrain. Theor Appl Climatol 52:119–134

Collins WD, Rasch PJea (2004) Description of the NCAR Community Atmosphere Model (CAMÂ 3.0), Technical report NCAR/TN-464+STR. National Center for Atmospheric Research, Boulder, Colorado, 210 pp

Doran JC, Horst TW (1982) Observations and models of simple nocturnal slope flows. J Atmos Sci 40:708–717

Eliassen A (1959) On the formation of fronts in the atmosphere. In: Bolin B (ed) The atmosphere and the sea in motion., University press, Oxford, pp 227–287

Gudiksen PH, Leone MJJ, King CW, Ruffieux CW, Neff WD (1992) Measurments and modeling of the effects of ambient meteorology on nocturnal drainage flows. J Appl Meteorol 31:1023–1032

Holton JR (1967) The diurnal boundary layer wind ascillation above sloping terrain. Tellus 19:199 – 205

Houze RA (2004) Mesoscale convective systems. Rev Geophys DOI 10.1029/2004RG000150

Jacobson MZ (2005) Fundamentals of Atmospheric Modeling. Camebridge University Press, 2nd edition 828 pp

Kalnay E (2002) Atmospheric modeling, Data Assimilation and Predictability. Camebridge University Press, 364 pp

Kuligowski RJ (2002) A self-calibrating goes rainfall algorithm for short-term rainfall estimates. J Hydrometeorol 3:112 – 130

Maddox RA (1983) Large-scale meteorological conditions associated with midlatitude mesoscale convective complexes. Int J Climatol 111:1475–1493

Mahrt L (1982) Momentum balance of gravity flows. J Atmos Sci 39:2701–2711

Manins PC, Sawford BL (1979) A model of katabatic winds. J Atmos Sci 36:619–630

Petersen GN, Olafsson H, Kristjansson JE (2003) Flow in the lee of idealized mountains and greenland. J Atmos Sci 60:2183–2195

Petkovsek Z, Hocevar A (1971) Night drainage winds. Arch Meteorol Geophys Bioklim 20:353–360

Pielke RAea (1992) A comprehensive meteorological model system - rams. Meteorol Atmos Phys 49:69 – 91

Poulos GS, Bossert JE (1995) An observational and prognostic numerical investigation of complex terrain dispersion. J Appl Meteorol 34:650–669

Poulos GS, Bossert JE, McKee TB, Pielke RA (2000) The interaction of katabatic flow and mountain waves. part i: Observations and idealized simulations. J Atmos Sci 57:1919–1936

Rutledge SA (1991) Middle latitude and tropical mesoscale convective systems. Rev Geophys pp 88–97

Skamarock WC, Klemp JB, Dudhia J, Gill DO, Barker DM, Wang W, Powers JG (2008) A description of the Advanced Research WRF Version 3. Technical report. NCAR, USA

Trigo IB, Viterbo P (2003) Clear-sky window channel radiances: A comparison between observations and the ecmwf model. J Appl Meteorol 42:1463 – 1479

Whiteman CD, Hoch SW, Lehner M, Haiden T (2010) Nocturnal cold air intrusions into a closed basin: Observational evidence and conceptual model. J Appl Meteorol Clim DOI 10.1175/2010JAMC2470.1

Xue M, Droegemeier KK, Wong V, Shapiro A, Brewster K (1995) Advanced Regional Prediction System (ARPS) version 4.0 user's guide. Center for Analysis and Prediction of Storms, University of Oklahoma, 380 pp

Xue M, Droegemeier KK, Wong V (2000) The advanced regional prediction system (arps) - a multiscale nonhydrostatic atmospheric simulation and prediction tool. part i: Model dynamics and verification. Meteorol Atmos Phys 75:161–193

Xue M, Droegemeier KK, Wong V, Shapiro A, Brewster K, Carr F, Weber D, Liu Y, Wang DH (2001) The advanced regional prediction system (arps) - a multiscale nonhydrostatic atmospheric simulation and prediction tool. part ii: Model physics and applications. Meteorol Atmos Phys 76:134–165

3 Impact of Terrain Configuration on Katabatic Flows

This chapter is published in *Boundary Layer Meteorology*, 134, 2, 307-325, 2010.
Received: 28 January 2009 / Accepted: 2 November 2009

The Impact of Different Terrain Configurations on the Formation and Dynamics of Katabatic Flows - Idealised Case Studies

Katja Trachte [1], Thomas Nauss [2] and Jörg Bendix [1]

[1] Laboratory for Climatology and Remote Sensing (LCRS), Faculty of Geography, Philipps-University Marburg, Marburg, Germany
[2] Faculty of Geography, University of Bayreuth, Bayreuth, Germany

Abstract Impacts of different terrain configurations on the general behaviour of idealised katabatic flows are investigated in a numerical model study. Various simplified terrain models are applied to unveil modifications of the dynamics of nocturnal cold drainage of air as a result of predefined topographical structures. The generated idealised terrain models encompass all major topographical elements of an area in the tropical eastern Andes of southern Ecuador and northern Peru, and the adjacent Amazon. The idealised simulations corroborate that (i) katabatic flows develop over topographical elements (slopes and valleys), that (ii) confluence of katabatic flows in a lowland basin with a concave terrainline occur, and (iii) a complex drainage flow system regime directed into such a basin can sustain the confluence despite varying slope angles and slope distances.

Keywords Confluence, Katabatic flows, Numerical simulation, Terrain configuration

3.1 Introduction

Katabatic flows are atmospheric boundary layer phenomena that form in hilly and mountainous regions worldwide. They develop on calm, clear nights by radiative cooling of the surface, generating a horizontal temperature gradient to the ambient air at the same height. Wind speed is conditioned by the cooling rates and the vertical temperature gradient, the surface roughness and the angle of elevation. Therefore the atmospheric conditions, the surface characteristics (i. e. the current land cover) as well as the terrain represent the essential factors that affect the development of katabatic flows (Prandtl, 1942; Defant, 1949; Shapiro and Fedorovich, 2007).

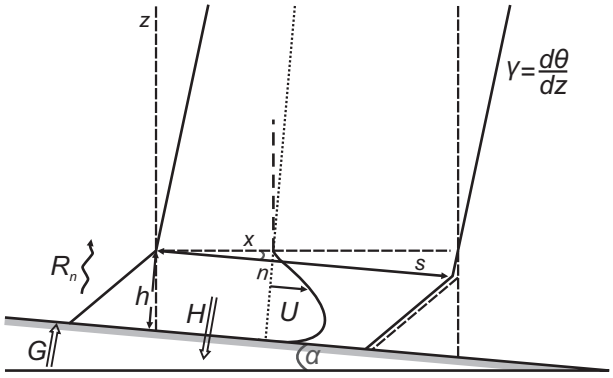

Figure 3.1: Schematic of an idealised katabatic flow (after Manins 1992)

Figure 3.1 shows an idealised flow along a slope with an angle α (after Manins 1992). As a result of longwave emission into the atmosphere a sensible heat flux H from the atmospheric boundary layer towards the surface develops, cooling the air. This radiative divergence (R_n) associated with the heat fluxes (H) into the ground leads to the development of an inversion with depth h. In addition, horizontal temperature and pressure gradients are generated between the ambient air over the slope and the air away from the slope at the same height. As a consequence of this horizontal density difference a downslope motion U of cold air as a function of the angle α and the slope distance occurs. The flow starts with the typical jet-like profile and persists by steady cooling of the surface layer, sustaining the density gradient and creating a buoyancy deficit. The shape of the wind profile results from ground friction retarding the streaming air directly over the ground and a pressure gradient decreasing with increasing height in the inversion layer h.

Because of their drainage effect, katabatic flows ensure an efficient nocturnal ventilation of the slopes. Normally, they affect local weather by inducing a stabilisation of the atmosphere within the nocturnal boundary layer which has been consistently examined over the few decades (Fleagle, 1950; Thyer, 1966; Gutman, 1983; Smith and Skyllingstad, 2005; Poulos et al., 2007; Yu and Cai, 2006). Such investigations comprised measurement campaigns as well as model studies for a better comprehension of their characteristics and more realistic prediction of their occurrence.

Horst and Doran (1986) investigated the initial phase of nocturnal slope flows in the Geysers Geothermal Resource Area of northern California with different topography and vegetation. Clements et al. (1989) showed the mean structure of the drainage flow down the Brush Creek valley of western Colorado. Skyllingstad (2003) used a large-eddy simulation model to study the structure and evolution of katabatic flows over simple slopes.

For the current study, the impact of different topographical geometries on the formation and dynamics of katabatic flows is examined. For this reason, two different areas are of interest: the eastern Andes of southern Ecuador and the adjacent Peruvian Amazon (see figure 3.2 right).

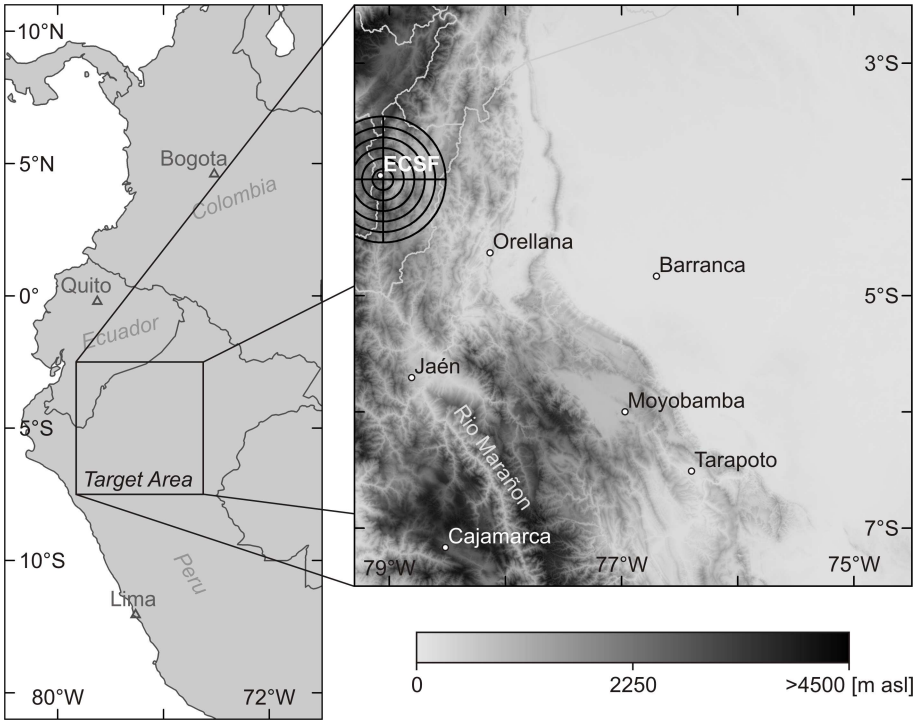

Figure 3.2: Study area (left), target area (right) with coverage of the local area weather radar

In the Andean highlands (Bendix et al., 2006) found a nocturnal rainfall maximum in the Rio San Francisco Valley (ECSF (Estacion Cientifica San Francisco) in figure 3.2). Precipitation measurements from automatic climate stations and vertical pointing rain radar revealed a significant and quite constant early morning rainfall maximum within this study area. An analysis of corresponding GOES satellite imagery shows the nocturnal formation of mesoscale convective systems (MCS) in the second region, the Andean foothills south-east of the Rio San Francisco Valley (figure 3.2) (Bendix et al., 2009). It was hypothesised that the generation of the cloud cluster and, thus, the nocturnal rainfall on the slopes could be associated with

nocturnal cold air drainage flow from the Andean slopes and valleys: (i) The cold air confluences due to the concave-shaped Andean terrain in the foothill region, (ii) where it converges with the warm moist air of the Amazon basin. This process could lead to low-level instabilities and to the formation of the MCS.

Here, we attempt the analysis of the first process of the hypothesis stated above, i. e. the analysis of the influence of different terrain shapes on the occurrence of idealised katabatic flows with special interests on their lowland confluence. The geometry of the topography exerts a strong effect on the general behaviour of the flow, with a concave lined slope the air is forced to confluence indicated by an additional mass contribution.

Due to unavailable measurements in the cloud formation region, the most appropriate tools to disentangle these processes are numerical models. The development of models to simulate katabatic flow systems extends from linear hydraulic models (Ball, 1956; Manins and Sawford, 1979; Mahrt, 1982; Fitzjarred, 1984; Kondo and Sato, 1988) to numerical model studies considering the development and the forecast of the flow (Garrett, 1983; Lalaurette and Andre, 1985; Doran, 1990b; Heilman and Takle, 1991; Gudiksen et al., 1992).

In this study, a numerical model has been used to examine, (i) the confluence of the flow with a uniform concave lined terrain shape, and (ii) the impact of a drainage system on the confluence considering the orographical situation in the second study area. To do so, simplified terrain models are used, which highlight the main features of the real terrain while simultaneously avoiding, for example, very steep valleys leading to problems in the wind field computation (Chow et al., 2006). Since the Peruvian east Andean slopes of the target area consist of an irregular ridgeline forming a concave shaped basin carved by several valleys, the most complex terrain model also consists of a basin with surrounding mountain tops and draining valleys with special reference to lowland cold air confluence. In addition, less complex terrains are used in our study to analyse the principle alteration of momentum and energy fluxes due to an evolving katabatic flow. By increasing the complexity of the terrain models between the different simulation runs, the role of different orographic features on the development of katabatic flows and their impact on the structure and propagation of the flow can be revealed.

The next section gives an overview of the model set-up and the idealised terrain models. Afterwards, the different idealised profiles demonstrate their impact on the general flow dynamics concerning a lowland confluence of cold air due to a concave terrain configuration.

3.2 Model Set-up

The mesoscale model Advanced Regional Prediction System (ARPS) was used to analyse the impact of different terrain shapes on the dynamics of idealised katabatic flows. ARPS was developed at the Center for Analysis and Prediction of Storms (CAPS) at the University of Oklahoma, and is a three-dimensional, non-hydrostatic model with a generalised terrain-following coordinate system and a vertically stretched grid. For more details, see Xue et al. (1995, 2000, 2001).

The idealised simulations of the katabatic flows are calculated on two different domains: three runs using a domain with 120 x 120 grid points and another two runs using a domain with 402 x 402 grid points. Both domains have a horizontal resolution of 250 m. The vertical grid was stretched with a hyperbolic function, with a resolution of 10 m near the ground and 500 m at the top of the domain. In the lower domain, 30 of the 55 vertical layers are located to engage the development of a downslope motion in the nocturnal boundary layer.

3.2.1 Topography

In order to analyse the effects of various topographical geometries on the behaviour of the propagation of katabatic flows, the main features of the target area have been simplified. Therefore, five simplified terrain configurations with increasing complexity have been used (figure 3.3).

The basic topography to simulate katabatic flows is a simple slope (figure 3.3a), used to demonstrate the essential characteristics inducing a downslope flow, i. e. the vertical temperature distribution, the wind field, the net radiation and the surface fluxes. The slope angle α has a value of approximately 5°. By mirroring the simple slope, a simple valley is generated, leading to an accumulation of the cold drainage air in the valley floor (figure 3.3b). Drainage of the accumulated air is obtained by creating an additional along-valley inclination angle β of approximately 1° (figure 3.3c). Thus, besides the cross-valley flows, the along-valley flow draining the cold air into the basin can be represented. To examine the confluence of katabatic flows as a result of a topographical shape, a terrain model forming a uniform concave ridgeline was used (figure 3.3d). The slope angle α is close to the previous terrain models. With this orographical shaping, the general behaviour concerning the confluence is disclosed. Since the eastern slopes of the Ecuadorian / Peruvian Andes in the target area shown in figure 3.2 form a quasi-concave shaped basin surrounded by several mountain tops and draining valleys, the most complex terrain model consists of a concave ridgeline carved by several valleys (figure 3.3e). They form an extensive drainage system directed towards the basin, and it enables the analysis of both the inflow of cold air into the basin due to the valleys and its confluence.

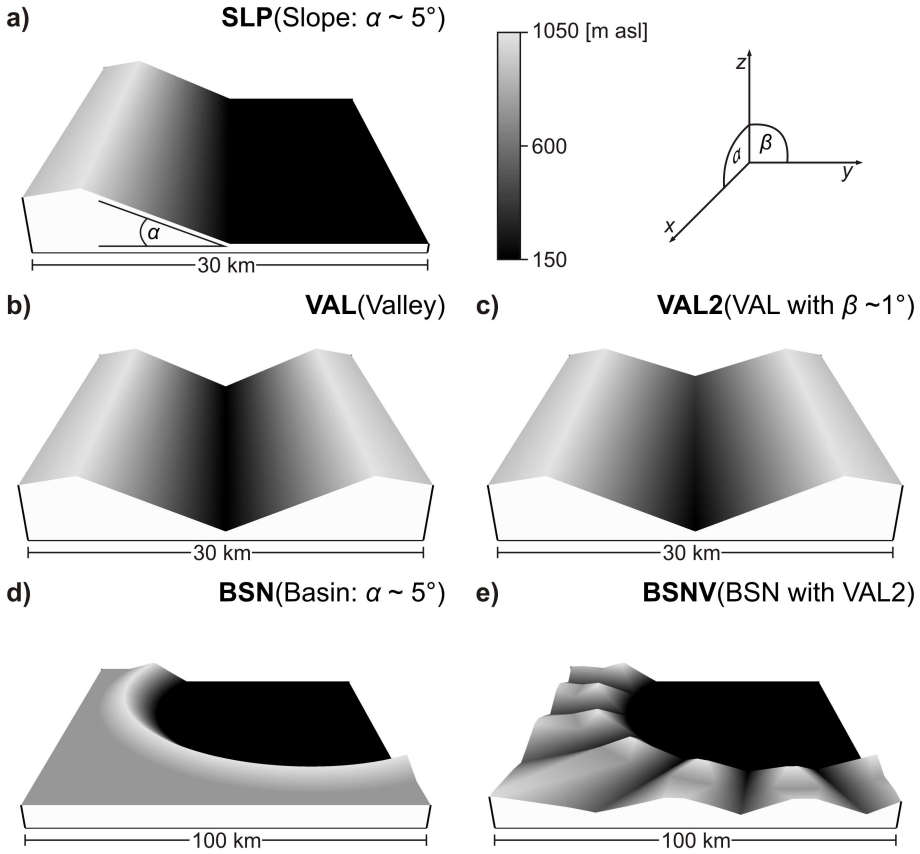

Figure 3.3: Simplified terrain models: a) simple uniform slope (SLP), b) simple uniform valley (VAL), c) simple valley with an additional along-valley height gradient (VAL2), d) basin (BSN), e) basin with a drainage system (BSNV)

3.2.2 Initialisation and Boundary Conditions

The initial values for the atmospheric conditions representing the situation at sunset are provided by an idealised sounding, and are derived from a tropical model atmosphere (McClatchey et al., 1972), and adjusted with an approximately neutral temperature stratification in the lower atmosphere and a lightly stable profile in the upper atmosphere. The initial potential temperature starts with 300 K at the surface and increases by 0.5 K·km^{-1} up to a height of 3000 m. Above this level, the potential temperature increases by 4 K·km^{-1}. To avoid any stream flows overlaying the thermally induced flow at the beginning of the simulation, the windfield is set to zero. Water was considered in the simulation for the calculation of the surface fluxes only.

The boundary conditions of each domain have been set to a rigid wall at the top with a damping layer at two-thirds of the atmosphere with five friction absorbing layers to prevent unrealistic reflection. At the lateral boundaries, open radiation

conditions with the Klemp and Wilhelmson type (Klemp and Wilhelmson, 1978) for the constant phase speed, which is computed and applied at each time step on the four lateral sides, have been used.

3.2.3 Physics

ARPS was used with the following physics packages: for the turbulence parametrisation the 1.5-order turbulent kinetic energy *(TKE)* with the Deardorff closure scheme was used (Deardorff, 1972). The time-dependent *TKE* is solved by a prognostic equation and determines the mixing length and velocity scale. It consist of terms for advection, potential-kinetic energy conversion, shear production, dissipation and diffusion of *TKE* (Xue et al., 1995, 2000).

The surface fluxes are responsible for the mass and heat exchange with the atmosphere. In ARPS they are computed by a stability and roughness-length dependent surface-flux model (Businger et al., 1971; Byun, 1990). The fluxes are solved on the basis of the similarity theory of Monin and Obukhov. The surface momentum fluxes are defined by

$$\tau_{13}|_{surface} \equiv -\left[\overline{\rho u'' w''}\right]_{surface} = \rho C_{dm} V u \,, \tag{3.1}$$

$$\tau_{23}|_{surface} \equiv -\left[\overline{\rho v'' w''}\right]_{surface} = \rho C_{dm} V v \,. \tag{3.2}$$

, involving the drag coefficient C_{dm} and the wind speed V, with components u and v . The sensible and latent heat fluxes that account for heat exchange are described by

$$H = \overline{\rho} C_{dh} C_p V \left(T - T_s\right) \,, \tag{3.3}$$

$$LE = L \left(E_g + E_{tr} + E_r\right) \,, \tag{3.4}$$

with the sensible and latent heat flux H and LE, the heat exchange coefficient C_{dh}, the air temperature T taken at the first level above ground and the ground surface temperature T_s. Consequently, the direction of the sensible heat flux is dependent on the temperature gradient near the surface. The latent heat flux is the sum of the evaporation of the soil surface E_g, the transpiration E_{tr} and the fluxes from canopy water evaporation E_r. In the present simulations the surface fluxes are calculated with stability-dependent drag coefficients and the bulk Richardson number as the stability parameter. For more details, see Xue et al. (1995, 2001).

Soil-model general surface characteristics such as soil and vegetation types are provided by a force-restore two-layer soil and vegetation model (Noilhan and Planton, 1989). It solves five prognostic equations for the soil temperature and soil moisture, where the vertical thickness of the soil layer is separated into a thin upper layer (0.01 m) and a deep layer (1 m). The surface layer interacts with the atmosphere, affecting its temperature, whereas the deep layer acts as a temperature reservoir affecting its thermal energy rather slowly. The input parameters for the soil type and the vegetation is based on USDA (United States Department of Agriculture)

textural classes. ARPS provides 13 soil types (including water and ice) and 14 vegetation classes. Each run in the current study is initialised with loam and rain forest considering the conditions in Ecuador.

The radiative cooling (see figure 3.1) necessary for the thermally driven flow is considered through atmospheric radiation transfer parametrisations. It is the primary force of the heat energy budget (5) and includes the net radiation, sensible heat flux and ground heat flux into the surface. The net radiative flux is given by

$$R_n = R_{sw}\,(1-\alpha_g) + \epsilon_g \left(R_A - \sigma T_s^4\right) , \tag{3.5}$$

with the shortwave radiation R_{sw}, albedo α_g, ground surface emissivity ϵ_g, incoming longwave radiation R_A and emitted longwave radiation from the ground surface σT_s^4 with σ for the Stefan-Boltzman constant. If R_{sw} becomes zero and the second term becomes larger, the net radiation becomes negative.

3.3 Results

The simplified terrain models presented above have been used to examine the development and modification of an idealised katabatic flow as a result of different topographical geometries. Potential temperature distributions (colour) and wind field patterns (vectors) show general characteristics of the cold drainage air. With the ground surface fluxes, the driving force of the flow is illustrated. In order to demonstrate the impact of slope geometry on the occurrence of the flow, horizontal divergence fields and mass fluxes will be discussed in the context of flow confluence.

3.3.1 Development of Katabatic Flows

Figure 3.4 shows the evolution of the katabatic flow along a simple slope in a vertical cross-section as a function of the potential temperature (colours) and wind field distribution (vectors). In the beginning the potential temperature is horizontal stratified, changing to a slope-parallel distribution during the simulation. The decrease in air temperature develops first in the lower atmosphere and generates a temperature gradient to the ambient air at the same height. This process produces a temperature inversion near the ground, i.e. a katabatic layer as seen in figure 3.1. At the same time, the horizontal thermal gradient causes temperature advection, balancing the energy budget. Shortly after the start of the simulation, air temperature decreases by 1 K to 299 K (figure 3.4a). The heat transfer is balanced by the temperature advection of cold air flowing down the slope and a growing inversion layer. The cold drainage air accumulates at the foot of the slope, forming a cold pool. In the ongoing simulation, the katabatic layer grows through the continuous cooling of the surface (figure 3.4b). The air temperature adjacent to the ground cools by an additional 2 K to 297 K after 6900 s. When the cold air arrives at the lateral boundary of the domain, it converges and is also propagated to upper layers.

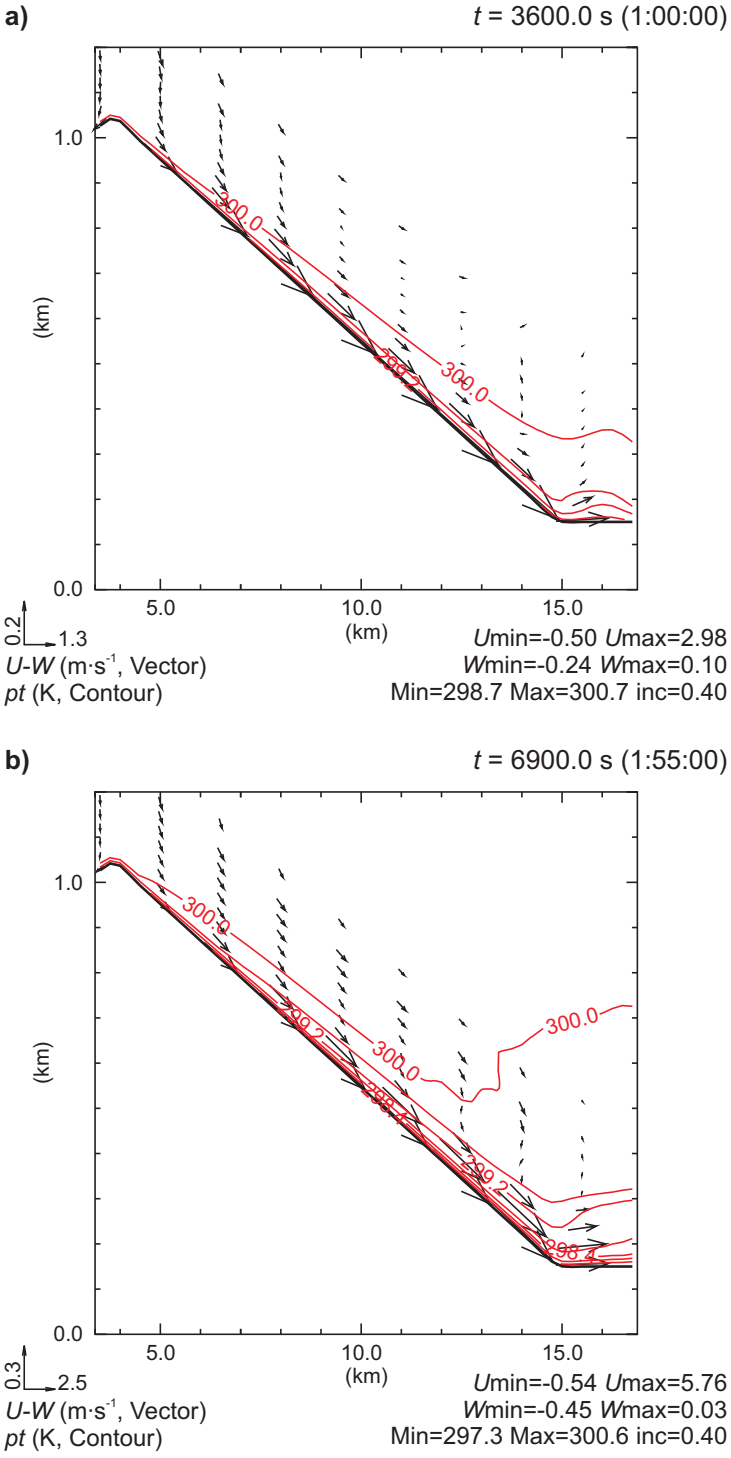

Figure 3.4: Vertical cross-section (xz-plots from $x = 3.0$ km, $y = 15.0$ km and $x = 17.0$ km, $y = 15.0$ km) of the potential temperature (pt, contour, K) and the wind field in u-w direction (vectors, m·s^{-1}) of SLP for time steps of (a) 3600 s and (b) 6900 s

The wind vectors in figure 3.4 show a typical katabatic flow structure. Driven by an increasing buoyancy deficit the velocity of the katabatic flow increases with increasing slope length. The wind speed grows linearly in time until it reaches its maximum value of 5.8 m·s^{-1} after 6900 s simulation time.

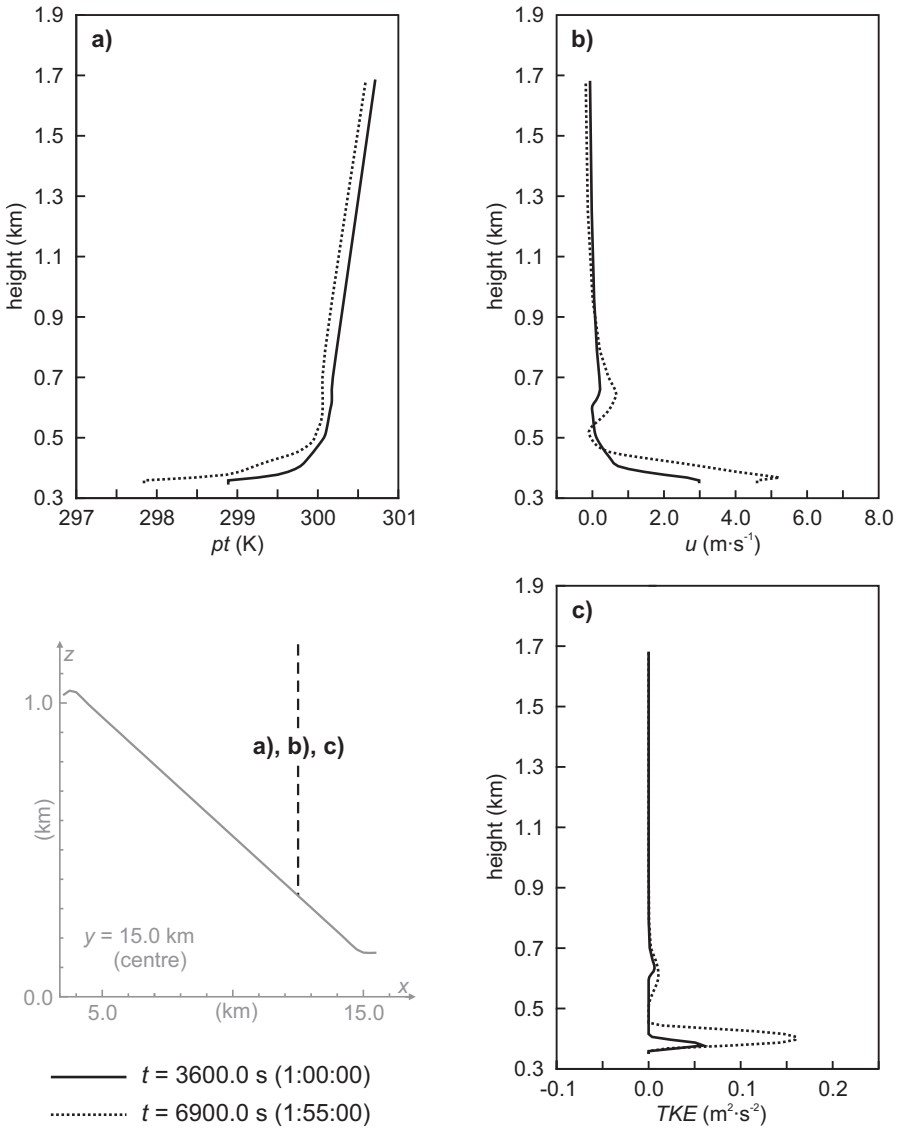

Figure 3.5: Profiles of (a) the potential temperature (*pt)*, (b) the wind vector (u) and (c) the turbulent kinetic energy (TKE) for time steps of 3600 s and 6900 s taken at x = 12.5 km and y = 15.0 km

Typical characteristics of katabatic flows are displayed on figure 3.5, showing the vertical profile of the potential air temperature, the wind velocity in the u-direction and the TKE in the centre of the slope. The potential temperature shows the evolution of a positive temperature gradient in the lower atmosphere with 3

K·100 m^{-1}. Above this inversion, the temperature profile undergoes transition into an isothermal state that separates the katabatic layer from the free atmosphere. At this height, the buoyancy term is zero and the temperature adjacent to the ground equals the temperature of the ambient air at the same height. The wind profile forms the typical jet-like profile of a downslope flow shown in figure 3.1 with maximum wind speeds (5.8 $m \cdot s^{-1}$) near the ground level, where the influence of the positive temperature gradient is strongest. Above and below this level, the velocity decreases because of increasing ground friction (below) and a decreasing positive temperature gradient (above). At higher levels, the latter leads to a decline in wind speeds to values around zero. In addition to mechanical turbulences induced by ground friction, the vertical wind shear is the second main source of *TKE* in a stable atmosphere such as this. The maximum of the *TKE* is near the maximum of the mean wind speed and reaches values of 0.16 $m^2 \cdot s^{-2}$ at levels where the vertical wind shear has its maximum (Horst and Doran, 1986; Heilman and Takle, 1991).

A comparison of the strength of the katabatic layer with an estimation of the Manins and Sawford hydraulic model (Manins and Sawford, 1979) (figure 3.1) has been made to show that the vertical resolution does not affect the flow. The estimation of their model describes the depth h as a function of slope distance s and slope angle α with the entrainment coefficient E and is defined as follows (see Horst and Doran, 1986):

$$h = 0.75Es \tag{3.6}$$

$$E = 0.05(\sin \alpha)^{2/3} \tag{3.7}$$

After this calculation the simulated katabatic layer is supposed to achieve a depth of 88 m. Compared to the simulation results in figure 3.4, a depth of 121 m is obtained. Thus, our results of an idealised katabatic flow with the model set-up presented above approximates the estimated flow depth after the Manins and Sawford model. With a higher vertical resolution near the surface, it could be improved. But as the focus of this study is on the modification of the flow by topographical configurations, the outcome is sufficient and further adjustments were not considered necessary.

The driving mechanism of the katabatic flow is the buoyancy deficit, which develops due to radiation divergence (equation 3.5) associated with the ground heat fluxes (equations 3.1, 3.2, 3.3, 3.4) resulting from mechanically induced *TKE* and the latent and sensible heat fluxes. ARPS solves the surface fluxes responsible for the cooling of the surface on the basis of the similarity theory (equations 3.1, 3.2). The soil temperature reduces to a value below the adjacent air temperature followed by the sensible heat flux (equation 3.3) from the atmospheric boundary layer to the earth surface balancing the heat loss. The surface acts as a sink for the thermal energy. The result is a cooling of the lower atmosphere and a development of a positive temperature gradient. A negative net radiation *(R_n)* was observed during the simulation (figure 3.6), which indicates that the second term on the right-hand side of equation 3.5 is overbalanced. In the first hour, the net radiation decreases slightly, but remains constant afterwards at values around 100 $W \cdot m^{-2}$.

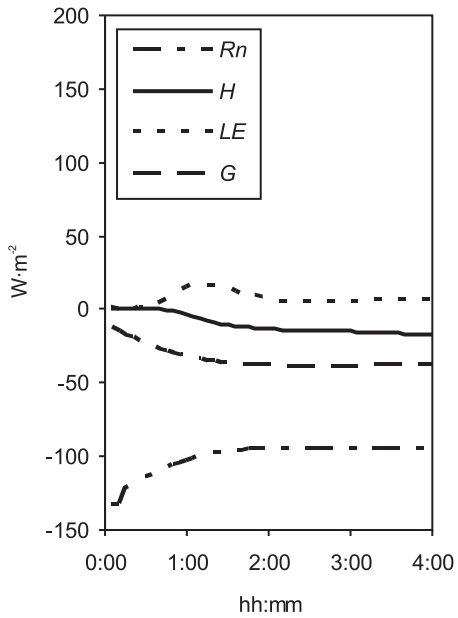

Figure 3.6: The heat energy fluxes in $W \cdot m^{-2}$ with the net radiation (Rn), the sensible heat flux (H), the latent heat flux (LE) and the ground heat flux (G) as a function of simulation time between 0 and 4 hours taken at $x = 12.5$ km and $y = 15.0$ km

Hence, the buoyancy deficit is determined by the flow velocity and the slope angle. The sensible heat flux H in the first hour of the simulation is almost zero, indicating less development, and afterwards H becomes negative as well and stays constant throughout the simulation. So an energy flux from the atmosphere to the surface layer exists (figure 3.6). The atmospheric boundary layer is constantly cooled, as indicated by the net radiation and ground surface fluxes, and cold air is constantly transferred to the upper layers. Thus, the temperature deficit between the atmosphere and the surface decreases, causing a constant sensible heat flux from the atmosphere to the surface. The katabatic flow is sustained as long as the net radiation is negative. The distribution of the heat energy fluxes in figure 3.6 shows the thermally driven mechanism of the downslope flow. Correlated with the temperature and windfield patterns in figure 3.4, their profiles in figure 3.5 and the the estimation of the katabatic layer, one can conclude that ARPS produces feasible katabatic flows with chosen initial values and model set-up.

The cold drainage flow into a uniform valley (VAL), and into a valley with an additional along-side inclination (VAL2), was simulated as well. The VAL terrain model consist of two identical slopes, which have the same slope angle as SLP presented above. Due to several studies of katabatic flows along simple valleys, the results are summarised and the simulations not shown. As expected, an accumulation of the cold drainage air occurs in the VAL case due to the lack of an along-valley inclination. The valley cross-flow increases to maximum values around 3.6 $m \cdot s^{-1}$. Its values are minor compared to SLP due to the converging flow from the sidewalls with resulting upward motion. With an additional along-valley inclination, the cold drainage air is able to develop as an outflow, which obtains maximum velocities of approximately 1.8 $m \cdot s^{-1}$. Compared to previous studies, (e. g., Doran et al., 1990a),

the katabatic flow shows similar dynamics, e. g. the inversion depth down the valley is lower than at the higher sidewalls, which produces smaller flow velocities.

3.3.2 Impact of Topography

The impact of the topography on the occurrence of katabatic flows regarding its confluence is demonstrated with the terrain models BSN and BSNV (figure 3.3). BSN represents the first approximation of the concave-lined Andean terrain forming a basin in the target area. With potential temperature (colour) and corresponding wind field (vectors) patterns, the regime of the cold drainage air is indicated. Horizontal divergence fields illustrate the confluence and mass contribution inside the basin. Finally, BSNV describes the Andean orography with its complex drainage system. The impact of several mountain tops and a draining valley system, as it appears in the target area, on katabatic flows is examined. Also, horizontal divergence fields and mass changes show the influence of the katabatic flows.

Basin

For the analysis of the confluence of the katabatic flow, we begin with a uniformly concave curved slope creating a basin.

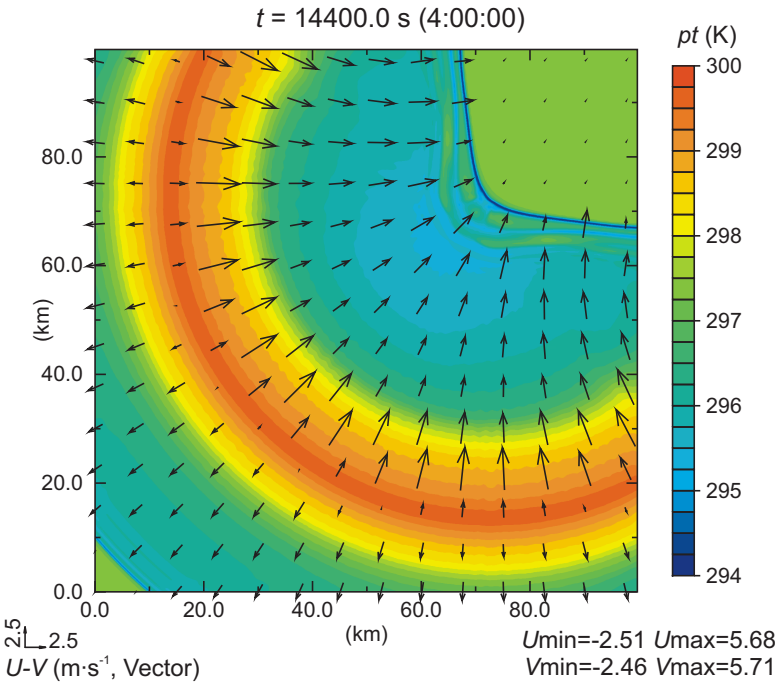

Figure 3.7: Horizontal cross-section (xy-plot at $z = 50$ m above ground level) of the potential temperature (pt, shaded, K) and the wind field in u-v direction (vectors, $\mathrm{m{\cdot}s^{-1}}$) of BSN for time step 14,400 s

The following Figures 3.7, 3.8, 3.9 show the results of the simulation in a height of 50 m above ground. In figure 3.7 the general behaviour of the flow is shown on the basis of the potential temperature distribution (colour) and the wind field patterns (vectors) at time step 14,400 s.

A basic katabatic flow generated by radiative cooling has developed. The cold drainage air flows down the curved slope; velocity increases with slope distance. A large horizontal temperature gradient causes the propagation of the air throughout the basin. Along the curved slope, the drainage air rapidly accelerated with distance to its maximum values around 5.8 $m \cdot s^{-1}$ as seen in SLP. At the foot, the drainage air decelerates to a minimum around 2 $m \cdot s^{-1}$. This is the result of the buoyancy deficit's decreasing influence. Driven by a large horizontal temperature gradient, the cold air advances further into the basin. There, as expected, the terrain configuration forces the flow to confluence, as shown by the accumulation of cold air in the centre of the basin with minimum potential temperature of 294.75 K. Inside the basin, the velocity remains nearly constant until it reaches the convergence zone, where the temperature gradient reaches its maximum. There the velocities rise again to reach maximum values of 4 $m \cdot s^{-1}$.

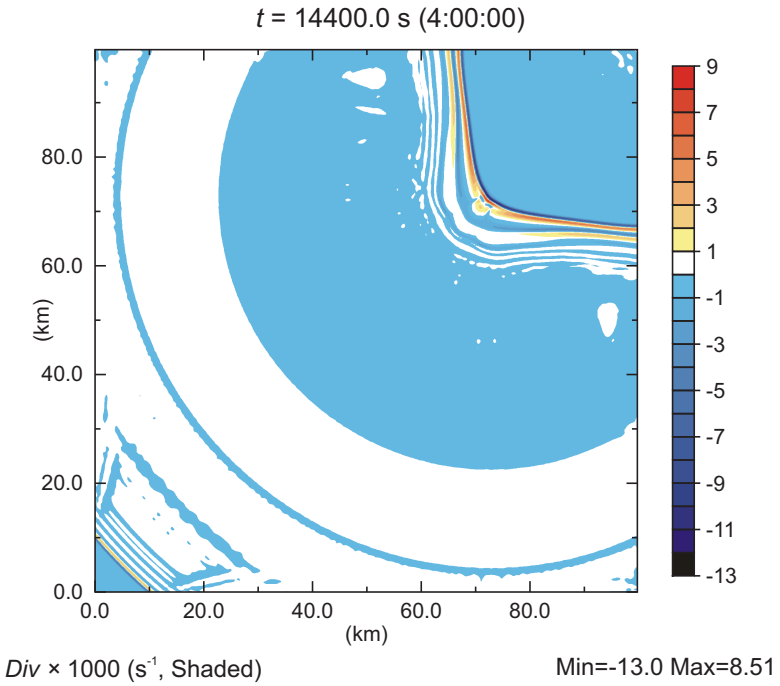

Figure 3.8: Horizontal cross-section (xy plot at $z = 50$ m above ground level) of the divergence field (DIV, shaded, s^{-1} amplified by a factor of 1000) of BSN for time step 14,400 s

The confluence of the horizontal wind field can be illustrated in terms of horizontal divergences. In doing so, negative values describe convergences and positive

values represent divergence of the horizontal wind field. The results in figure 3.8 are shown with an amplification factor of 1000. Inside the basin, a continuous horizontal convergence has developed, until the cold air reaches its maximum. In this zone, an explicit divergence line with maximum 8.5 s^{-1} alternates with an explicit convergence line of 13 s^{-1}, indicating frontal structures.

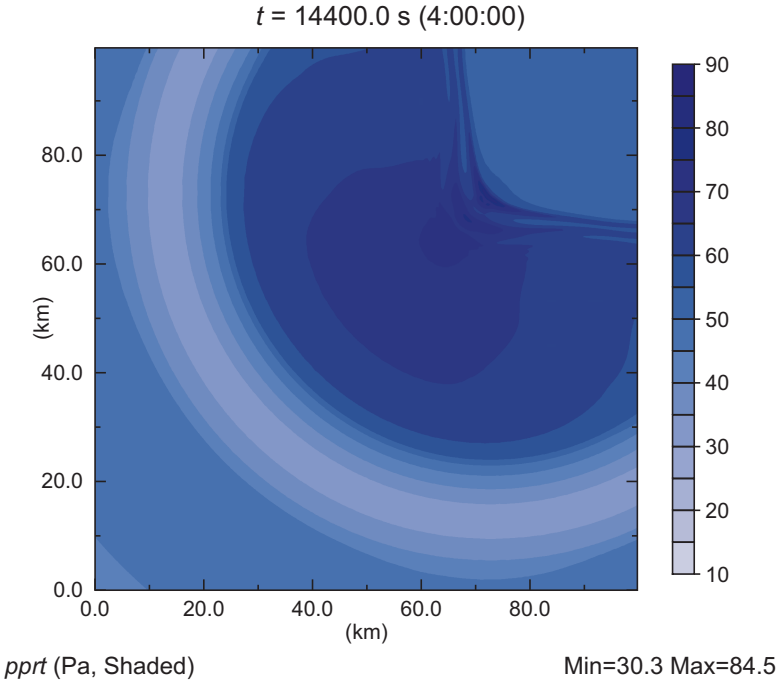

Figure 3.9: Horizontal cross-section (*xy* plot at $z = 50$ m above ground level) of the pressure perturbation field (*pprt*, shaded, Pa) of BSN for time step 14,400 s

However, to analyse the confluence of the cold drainage air due to the shape of terrain, we investigate the mass contribution as well. Since a confluence of the horizontal wind field near the surface is closely linked to changes in the mass field, the perturbation of pressure (*pprt*) is displayed in figure 3.9. At the slope, the pressure increases uniformly with distance by around 40 Pa, whereas inside the basin the largest perturbation is concentrated with a maximum 84.5 Pa. Most of the mass contribution is located there, particularly in the middle of the convergence zone. An accumulation of mass has taken place, which strengthens the issue of confluencing katabatic flows forced by the concave shape of the terrain configuration.

Drainage System

Finally, variations in the flow dynamics are analysed with a concave curved slope interrupted by several valleys generating a complex drainage system. The terrain model that was used describes the main features of the topography in the target area. The results of the simulation at a height of 50 m above the surface are displayed in

figure 3.10, 3.11, 3.12. The general occurrence is also shown in terms of the potential temperature distribution (colour) and wind vectors (figure 3.10).

As in BSN, a general katabatic flow along the slopes has developed through radiative cooling. The cold drainage air flows down the mountain into various valleys and directly into the basin. At the valley floors, maximum cooling with a potential temperature of 294 K occurs. Forced by the inclination of the valleys, the cold surface air drains into the basin. In their exit regions the cold air can spread, but as it advances further into the basin it undergoes confluence, forced by the concave topographical geometry. In BSN, a large horizontal temperature gradient was generated, causing this propagation.

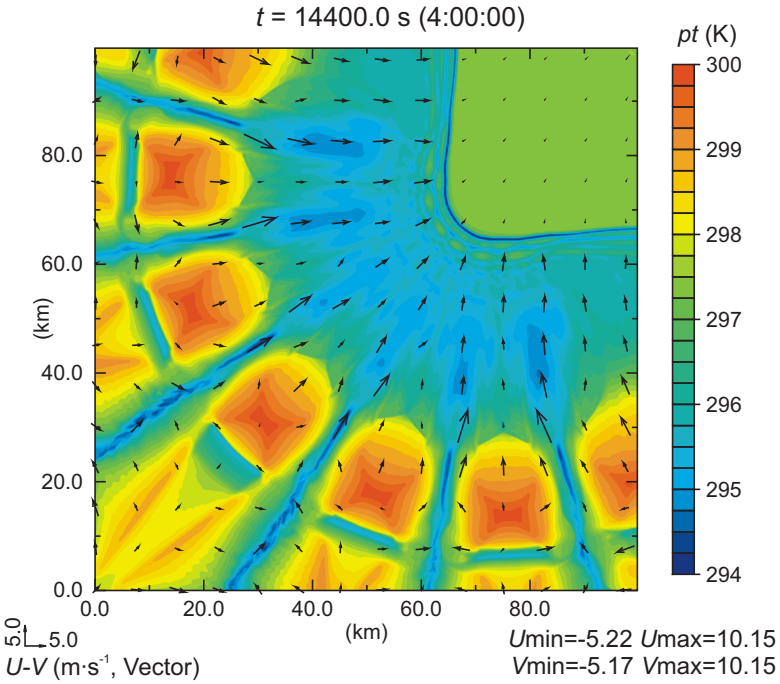

Figure 3.10: Horizontal cross-section (xy plot at $z = 50$ m above ground level) of the potential temperature (pt, shaded, K) and the wind field in u-v direction (vectors, m·s^{-1}) of BSNV for time step 14,400 s

The velocities of the katabatic flow differ slightly from BSN as a result of the drainage system. Along the slopes the flow accelerates with increasing distance to a maximum of 5.8 m·s^{-1} as with BSN and SLP. Inside the basin the flow too decelerates due to the decreasing influence of the buoyancy deficit, but not consistently. The impact of the drainage system is evident. The draining valleys add an additional driving force, accelerating the flow. With increasing distance along the valley floors, the cold air velocities increased to values around 9.5 m·s^{-1}. This is a combined result of the inclination and the channelling effect of the valleys. In their exit regions, the flow obtains a further acceleration to its maximum values of 10 m·s^{-1}. The flow

decreases with increasing distance from the exit regions, but accelerates again to 4 $m \cdot s^{-1}$ when it is close to the confluence zone where the temperature gradient reaches its maximum.

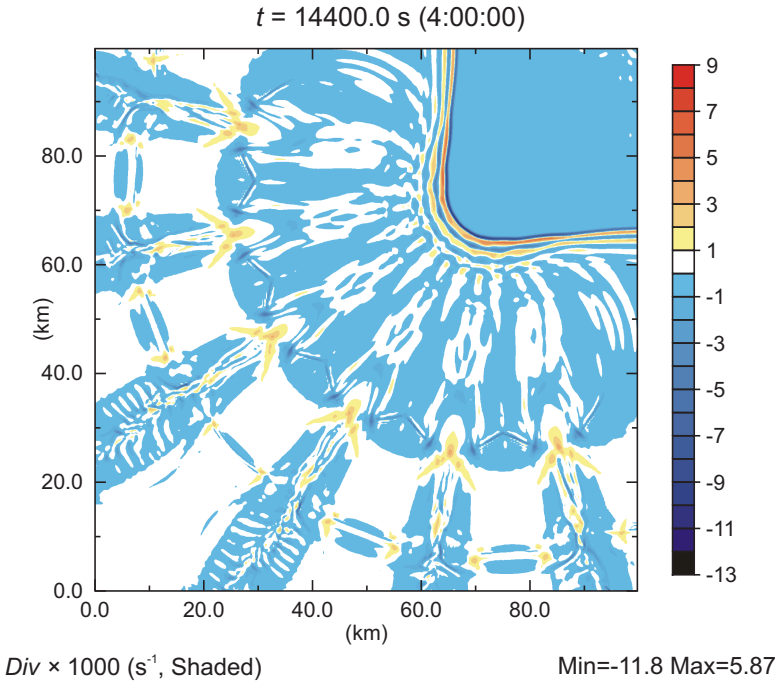

Figure 3.11: Horizontal cross-section (*xy* plot at $z = 50$ m above ground level) of the divergence field (*DIV*, shaded, s^{-1} amplified by a factor of 1000) of BSNV for time step 14,400 s

The horizontal divergence field (values are amplified by a factor of 1000) and pressure perturbation are also used to evaluate the confluencing katabatic flow (figure 3.11). The uniform convergence is divided by additional divergence patterns at the exit region of each valley caused by the cold drainage air advancing into the basin. The convergences reach values around 5.8 s^{-1}, whereas the divergences achieve 4 s^{-1}. Inside the basin the convergences decrease to values around 1 s^{-1}, as BSN, divided by calm regions. In the valleys the flow from the slopes initially converges, inducing an along-valley flow afterwards, as seen in the divergence field.

The corresponding pressure perturbation (*pprt*) field (figure 3.12) shows more details of the confluence of the cold drainage air mass. It is evident that the valley drainage into the basin contributes the greatest increase in mass, with a maximum of 77.2 Pa, which is created by the converging air from the surrounding mountain tops. Inside the basin, the pressure rises 67.5 Pa, but is unevenly allocated. However, the greatest mass increase occurs in the centre of the basin indicating the confluence of the cold drainage air due to the terrain configuration.

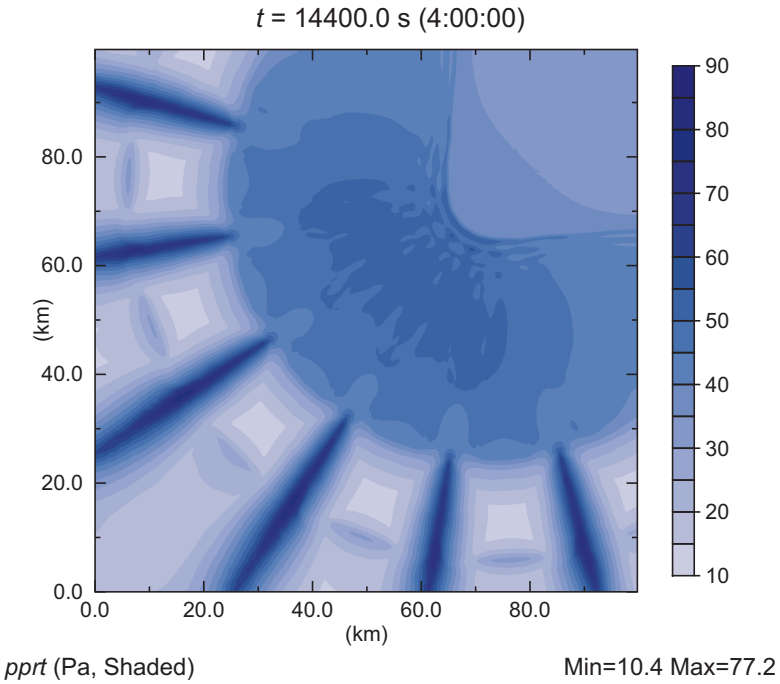

Figure 3.12: Horizontal cross-section (*xy* plot at $z = 50$ m above ground level) of the pressure perturbation field (*pprt*, shaded, Pa) of BSNV for time step 14,400 s

To take a closer look at this convergence zone, a cross-section through its middle has been made. Convergence of the horizontal wind field near the surface not only implies mass contribution, it is also related to vertical motion. Accordingly, the vertical divergence field overlayed with wind vectors in the *u*-*w* direction is shown in figure 3.13. The ambient atmosphere is calm, without any vertical motions, as already seen with previous figures. However, the region of interest shows an alternating convergence and divergence line associated with upward (maximum 1.2 $\mathrm{m{\cdot}s^{-1}}$) and downward (maximum 0.66 $\mathrm{m{\cdot}s^{-1}}$) motion, indicating a deformed wind field, which points to a frontal zone (Eliassen, 1959).

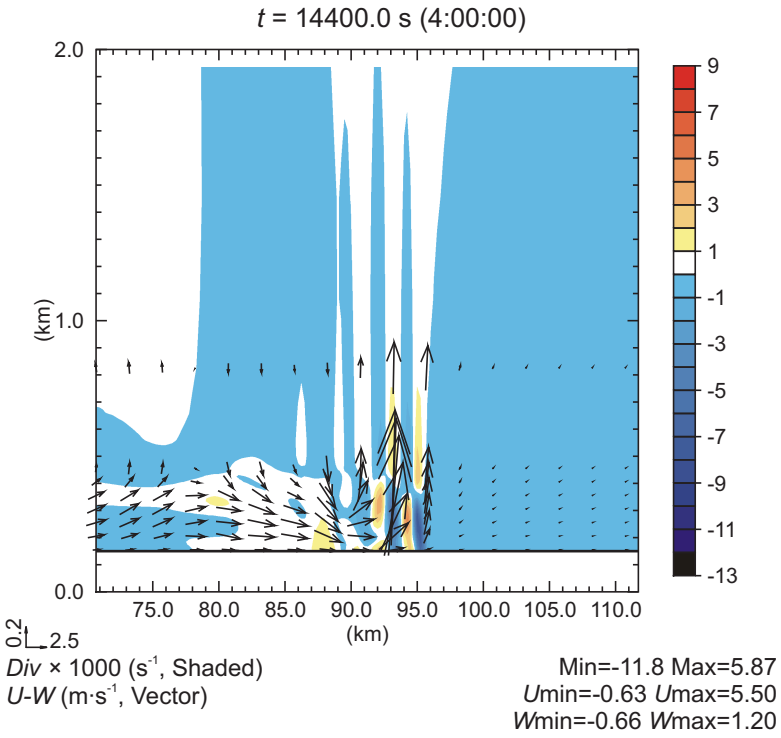

Figure 3.13: Vertical cross-section (xz plot from $x = 50.0$ km, $y = 50.0$ km to $x = 79.0$ km, $y = 79.0$ km) of the divergence field (DIV, shaded, s^{-1} amplified by a factor of 1000) and the wind field in u-w direction (vectors, $m \cdot s^{-1}$) of BSNV for time step 14,400 s

3.4 Discussion

As expected, the geometry of topography has strong effects on the general behaviour of katabatic flows. Particularly the concave terrain configuration shown herein demonstrates the topography's influence regarding the confluence of the cold drainage air over low terrain. With the simplified terrain models BSN and BSNV (figure 3.3), the main orographical features of the Andes of southern Ecuador / northern Peru are covered and are used to explore the occurrence and modification of the cold drainage air.

First, BSN as a uniformly concave terrain configuration was used to show the principle modification of a general katabatic flow concerning its confluence. The results of the simulations (figure 3.7) illustrate the common development of a thermally induced downslope with increasing wind velocity along the slope distance. The cold surface air drains into the basin, where it consistently advances through the basin as a result of the regular slope configuration. Forced by the topography, a convergence zone following the concave terrain line developed.

Interrupting the basic geometry of BSN with several valleys forming a complex drainage system into the basin, the complex structure of the Andean orography has been captured. Just as with BSN, BSNV was used to examine the confluence of the katabatic flow, but with a marked drainage system. As seen in figure 3.10, a steady flow was generated by the terrain configuration. The results of the simulation also show the development of a katabatic flow. However, this time a downslope motion occurs along every existing slope of the terrain model separating the regular inflow of cold air and its steady confluence. This follows the drainage system, induced by the six large valleys, causing variations of the cold air inflow. Thus, in the exit region the cold drainage air propagates faster into the basin as the air from the slopes directed towards the basin. Compared to the continuous concave line terrain, an unsteady inflow of cold air developed due to an irregular configuration of topography. The effect of slope angle and slope distance on the occurrence of katabatic flows, as described in the Manins and Sawford (1979), is demonstrated by the various slope angles forming the drainage system, as shown in figure 3.1.

An analysis of the horizontal divergence field in BSN and BSNV as shown in Figures 3.8 and 3.11 contributed to this result. In BSN, the basin is calm and undisturbed with a permanent convergence of approximately 2 s^{-1} until it reaches the zone of maximum horizontal temperature gradient. There, the cold drainage air converges with the less cold air from the basin. However, this convergence zone is arranged linearly following the concave lined terrain, and caused the mentioned acceleration in wind speed in the katabatic flow (Parish, 1982; Bromwich and Kurtz, 1984). With the perturbed pressure distribution, we can take a closer look to the confluence of cold air. As seen in figure 3.9, the greatest mass increase is concentrated in the middle of the basin, which indicates a confluencing katabatic flow on the basis of a concave lined slope.

The concave curved slope is interrupted by an extensive drainage system, which has consequent effects on the mass contribution to the basin (see figure 3.12). Since the valleys add an additional driving force, which generates an increase in the velocity compared to the downslope flowing directly into the basin, the inflow is discontinued. It is evident, especially in the exit region of each valley, that this acceleration leads to a modification of the cold air mass distribution. At the exit regions the flow can spread, which is made clear by the horizontal divergence field of the flow. The results are alternating patterns of divergences and convergences in the basin, which differ clearly from BSN. However, despite these variations in cold surface flow dynamics, a net confluence of the flow developed, as seen by the mass contribution in figure 3.12. As in BSN, the greatest mass increase took place in the centre of the basin, although the mass contribution is less due to the drainage system. A convergence line following the basic structure of the concave terrain line also developed, just as in BSN.

The vertical cross-section in figure 3.13 shows the formation of a typical frontal zone with upward and downward motions. However, the vertical velocities are rather

low, which results from insufficient moisture in the atmosphere. It must be pointed out that the simulations were primarily intended to show the occurrence of katabatic flows and to demonstrate their confluence as a result of the impact of terrain geometries. Nevertheless, the basic structures of a surface front are already visible and will be further analysed in future work with regard to the second hypothesis stated above.

3.5 Summary and Conclusions

In this paper the mesoscale model ARPS was used to investigate the impact of different terrain shapes on a katabatic flow in an idealised case study. The main subject of the analysis is the confluence of the flow due to a concave-lined terrain configuration. The target area is located at the eastern Andean slopes of southern Ecuador and the northern Peruvian Amazon basin. Due to the very steep slopes and valleys of the Andes, five different simplified terrain models representing the main characteristics of the topography in this area were used.

Using a simple slope model, it could be shown that a katabatic flow was generated. With the resulting potential temperature and wind field patterns the typical characteristics of cold drainage flows, such as the formation of a katabatic layer and the jet-like wind profile, were illustrated. Furthermore, it could be demonstrated that the surface heat fluxes, along with the associated cooling of the surface layer, act as main drivers for the katabatic flow. Hence, a typical thermally driven flow developed.

The impact of the topographical geometry with an uniformly concave-lined slope on katabatic flows was shown regarding its confluence. The cold drainage air was forced by the shape of the terrain to propagate into the centre of the basin. There it produced a large horizontal temperature gradient inducing a convergence line. As a result of the slope geometry the most pronounced horizontal divergence developed in the centre of the basin.

A complex drainage system captures the Andean orography of the target area. It changes the uniform concave slope structure with several valleys and mountain tops forming a complex drainage system regime. The results of the simulation show that the continuous flow structures of BSN were interrupted by the draining valleys, but the general flow behaviour was sustained. The effect of these properties is that, although no regular inflow of katabatic flow occurs due to various slope angles and distances, the cold drainage air confluenced because of the general concave geometry of the topography.

The results of the study at hand verify the initial hypothesis that nocturnal drainage air from slopes and valleys confluences due to a concave topography. A persistent thermally-driven flow advances through the basin, generating a convergence line that is largest in the centre. Thus, further work is required to verify the second hypothesis stated at the beginning, i.e. the formation of convective clusters

due to interaction in confluencing cold drainage air, shown herein with the warm moist air from the Amazon basin.

Acknowledgment
The authors are indebted to the German Research Foundation (DFG) for the funding of the work in the scope of the Research Unit RU816 'Biodiversity and Sustainable Management of a Megadiverse Mountain Ecosystem in South Ecuador', sub projects B3.1 and Z1.1 (BE 1780/15-1, NA 783/1-1).

References

Ball FK (1956) The theory of strong katabatic flows. Aust J Phys 9:373–386

Bendix J, Rollenbeck R, Reudenbach C (2006) Diurnal patterns of rainfall in a tropical andean valley of southern ecuador as seen by a vertical pointing k-band doppler radar. Int J Climatol 26:829–846

Bendix J, Trachte K, Cermak J, Rollenbeck R, Nauss T (2009) Formation of convective clouds at the foothills of the tropical eastern andes (south ecuador). J Appl Meteorol 48:1682–1695

Bromwich DH, Kurtz DD (1984) Katabatic wind forcing of the terra nova bay polynya. J Geophys Res 89:3561–3572

Businger JA, Wyngaard JC, Izumi Y, Bradley EF (1971) Flux-profile relationship in the atmospheric surface layer. J Atmos Sci 28:181–189

Byun DW (1990) On the analytic solutions of flux-profile relationships for the atmospheric surface layer. J Appl Meteorol 29:652–657

Chow FK, Weigel AP, Street RL, Rotach MW, Xue M (2006) High-resolution large-eddy simulations of flow in a steep alpine valley. part i: methodology, verification, and sensitivity experiments. J Appl Meteorol Climatol 45:63–86

Clements WE, Archuleta JA, Hoard DE (1989) Mean structure of the nocturnal drainage flow in a deep valley. J Appl Meteorol 28:457–462

Deardorff JW (1972) Parameterization of the planetary boundary layer for use in general circulation models. Mon Weather Rev 100:93–106

Defant F (1949) Zur theorie der hangwinde, nebst bemerkungen zur theorie der berg- und talwinde. Arch Meteorol Geophys Bioklim A1:421–450

Doran JC (1990b) The effects of ambient winds on valley drainage flows. Boundary-Layer Meteorol 55:177–189

Doran JC, Horst TW, Whiteman CD (1990a) The development and structure of nocturnal slope winds in a simple valley. Boundary-Layer Meteorol 52:41–68

Eliassen A (1959) On the formation of fronts in the atmosphere. In: Bolin B (ed) The atmosphere and the sea in motion., University press, Oxford, pp 227–287

Fitzjarred DR (1984) Katabatic wind in opposing flow. J Atmos Sci 41:1143–1158

Fleagle RG (1950) A theory of air drainage. J Meteorol 7:227–232

Garrett AJ (1983) Drainage flow prediction with a one-dimensional model including canopy, soil and radiation parameterizations. J Climate Appl Meteorol 22:79–91

Gudiksen PH, Leone MJJ, King CW, Ruffieux CW, Neff WD (1992) Measurments and modeling of the effects of ambient meteorology on nocturnal drainage flows. J Appl Meteorol 31:1023–1032

Gutman LN (1983) On the theory of the katabatic slope wind. Tellus, Series A (Dynamic Meteorology and Oceanography) 35A:213–218

Heilman WE, Takle ES (1991) Numerical simulation of the nocturnal turbulence characteristics over rattlesnake mountain. J Appl Meteorol 30:1106–1116

Horst TW, Doran JC (1986) Nocturnal drainage flow on simple slopes. Boundary-Layer Meteorol 34:263–286

Klemp JB, Wilhelmson RB (1978) The simulation of three-dimensional convective storm dynamics. J Atmos Sci 35:1070–1096

Kondo J, Sato T (1988) A simple model of drainage flow on a slope. Boundary-Layer Meteorol 43:103–123

Lalaurette F, Andre JC (1985) On the integral modelling of katabatic flows. Boundary-Layer Meteorol 33:135–149

Mahrt L (1982) Momentum balance of gravity flows. J Atmos Sci 39:2701–2711

Manins PC (1992) Vertical fluxes in katabatic flows. Boundary-Layer Meteorol 60:169–178

Manins PC, Sawford BL (1979) A model of katabatic winds. J Atmos Sci 36:619–630

McClatchey RA, Fenn RW, Selby JEA, Volz FE, Garing JS (1972) Optical properties of the atmosphere (Third Edition), AFCRL-72-0497. Hanscom Air Force Base, Bedford, Massachusetts, 108 pp

Noilhan J, Planton S (1989) A simple parameterization of land surface processes for meteorological models. Mon Weather Rev 117:536–549

Parish TR (1982) Surface air flow over east antarctica. Mon Weather Rev 110:84–90

Poulos G, Bossert JE, McKee T, Pileke RAS (2007) The interaction of katabatic flow and mountain waves. part ii: Case study analysis and conceptual model. J Atmos Sci 64:1857–1879

Prandtl L (1942) Stroemungslehre (Flow studies). Vieweg und Sohn, Braunschweig, Germany, 648 pp

Shapiro A, Fedorovich E (2007) Katabatic flow along a differentially cooled sloping surface. J Fluid Mech 571:149–175

Skyllingstad ED (2003) Large-eddy simulation of katabatic flows. Boundary-Layer Meteorol 106:217–243

Smith CM, Skyllingstad ED (2005) Numerical simulation of katabatic flow with changing slope angle. Mon Weather Rev 133:3065–3080

Thyer NH (1966) A theoretical explanation of mountain and valley winds by a numerical method. Arch Meteorol Geophys Bioklim A15:318–348

Xue M, Droegemeier KK, Wong V, Shapiro A, Brewster K (1995) Advanced Regional Prediction System (ARPS) version 4.0 user's guide. Center for Analysis and Prediction of Storms, University of Oklahoma, 380 pp

Xue M, Droegemeier KK, Wong V (2000) The advanced regional prediction system (arps) - a multiscale nonhydrostatic atmospheric simulation and prediction tool. part i: Model dynamics and verification. Meteorol Atmos Phys 75:161–193

Xue M, Droegemeier KK, Wong V, Shapiro A, Brewster K, Carr F, Weber D, Liu Y, Wang DH (2001) The advanced regional prediction system (arps) - a multiscale nonhydrostatic atmospheric simulation and prediction tool. part ii: Model physics and applications. Meteorol Atmos Phys 76:134–165

Yu Y, Cai XM (2006) Structure and dynamics of katabatic flow jumps: Idealized simulations. Boundary-Layer Meteorol 118:527–555

4 Katabatic Flows and the Formation of Convective Clouds

This chapter was submitted 31 August 2010 to *Journal of Applied Meteorology and Climatology*.

Katabatic Flows and Their Relation to the Formation of Convective Clouds - Idealised Case Studies

Katja Trachte and Jörg Bendix

Laboratory for Climatology and Remote Sensing (LCRS), Faculty of Geography, Philipps-University Marburg, Marburg, Germany

Abstract A reduced terrain model representing the main features of the eastern Andes of southern Ecuador and northern Peru, and the adjacent Amazon basin was used to investigate the formation of a katabatic induced surface cold front and sequentially initiation of deep moist convection. The topographical elements included describe a concave ridgeline with several valleys directed into a basin, forming a large drainage system regime. The effects of the terrain configuration was studied with an idealised numerical model. Inside the basin, a surface front following the concave terrain line developed due to the propagating cold air, generating a density / temperature gradient. When the confluence of the cold air was strong enough, the air in the centre of the basin began to rise. On the basis of sufficient moisture in the atmosphere, a convective cloud system formed. As an additional trigger mechanism, a nocturnal low level jet intensified the atmospheric instabilities in the planetary boundary layer. The result was a more severe cloud cluster.

Keywords Cold front, Katabatic flows, Cloud cluster

4.1 Introduction

A density current is a flow that is sustained by a density difference between two fluids. They are a common feature in the atmosphere and frequently investigated (Simpson and Britter, 1980; Bischhoff-Gauss and Gross, 1989). An example of an atmospheric density current is a katabatic flow (Haase and Smith, 1989; Sun et al., 2002): The thermally-induced flow of colder and therefore denser air down a slope into a less dense, warmer fluid driven by a horizontal temperature gradient. Density currents have typical characteristics (Simpson, 1982): a head is located at their leading edge, which is substantially larger than the following tail. It provides intensive mixing and vertical velocities in an otherwise calm, ambient atmosphere. In a downslope motion, this head becomes larger with increasing distance along the slope. In a horizontal current a nose develops, which is a zone lifted some levels above ground. The exact shape of the density current head strongly depends on the ambient atmospheric conditions. At the interface of the two fluids, a typical frontal zone develops, in which the gradient reaches its maximum. This front can be an important factor in varying the dynamics of the current.

Several studies could find evidence that atmospheric density currents trigger lifting of air parcels, which, with sufficient moisture, results in condensation and cloud formation processes (Cunningham, 2007; Moncrieff and Liu, 1999). Pagowski and Taylor (1998) examined the thermal and mechanical effects of the boundary-layer on the occurrence of atmospheric fronts. Shapiro et al. (1985) presents that the head of a density current can trigger the development of mesoscale convective cloud systems. Seitter (1986) shows that the lifting of air by the head leads to these processes in the lower atmosphere, but a further trigger is necessary to induce deep convection.

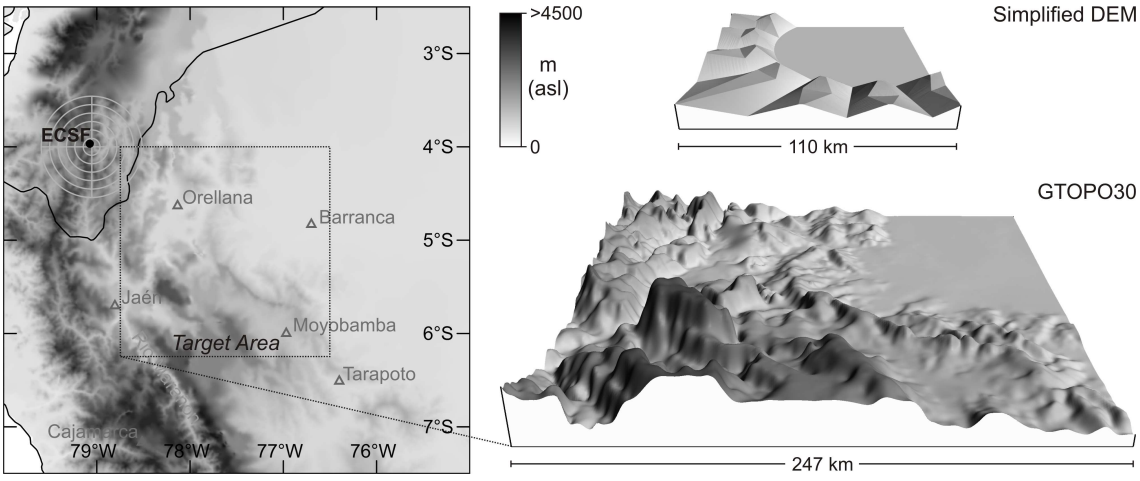

Figure 4.1: Topographical map (GTOPO30 data) of Southern Ecuador and the adjacent Peruvian Amazon basin displaying the target area and the location of the rain radar (left), a 3D view of the target area (lower right) and a 3D view of the simplified terrain (upper right)

The area of interest (see figure 4.1), for the current study covers southern Ecuador and the adjacent northern Peruvian Amazon basin. In the highlands of southern Ecuador, Rio San Francisco valley, precipitation measurements with automatic stations and vertical rain radar revealed a significant and quite constant early morning rainfall maximum (Bendix et al., 2006). Cloud analyses from corresponding GOES-E satellite data indicate a nocturnal formation of mesoscale weather systems at the foothills of Rio San Francisco valley in the Peruvian Amazon basin (Bendix et al., 2009).

It was hypothesised that the formation of the cloud cluster was a consequence of nocturnal cold air drainage from the Andean slopes and valleys into the Amazon basin. There it converges with the warm, moist Amazonian air, so that the katabatic flow acts as a local cold front inducing low-level instabilities (see De Angelis et al., 2004). Furthermore, as a result of the special orographic structure in this region, the katabatic flow confluences, increasing the lifting of air and therefore fostering deep convection. Additionally, a nocturnal low-level jet (LLJ) enhancing the atmospheric instabilities in the planetary boundary layer (PBL).

With an idealised case study, Trachte et al. (2010) examined the modification of katabatic flows by the shape of terrain with the approximated terrain model shown in the upper right part of figure 4.1. The structure of the topography in the target area displayed by the 3D view reveals a concave, irregular ridgeline carved by multiple, very steep valleys draining into the Amazon basin (figure 4.1 lower right). Based on this configuration the terrain's main features were simplified (figure 4.1 upper right). The author could show that a thermally-induced current develops and the concave geometry forces the air to confluence despite the extensive drainage system. The aim of the study at hand is (i) to present the evolution of a surface cold front as a result of katabatic flows, (ii) the consequential development of convective clouds when the air is lifted to its condensation level and (iii) the impact of a nocturnal LLJ as an additional trigger mechanism for deep convection. A numerical grid box model was used to analyse the hypothesised development of a convective weather system described above.

The next section gives a brief review of frontogenesis followed by a description of the model settings that was used. Afterwards, the results of the formation of the katabatic induced surface front and the development of convective cloud systems are discussed.

4.2 Methods

4.2.1 Frontogenesis

An atmospheric front is defined by a gradient of a scalar attribute such as the potential temperature (Θ). It can be described as a discontinuity in density / temperature and the wind velocity. Frontogenesis is the strengthening of this gradient with time

and can be induced by means of thermally-induced processes in the PBL, such as the net radiation loss. Thermal differences result in dynamic effects such as deformation of the horizontal wind field, which activates a secondary vertical circulation with convergences and divergences. Each front which develops in the PBL has the character of a cold front. They occur due to a temperature gradient in the lower troposphere while the upper atmosphere is undisturbed. For example, such a situation can occur in hilly regions on clear, calm nights, when a katabatic flow develops due to radiative cooling. The flow induces the necessary temperature difference through the transport of cold, dense air down the slope into warmer and less dense air. But such a surface front is short-lived and disintegrates due to smoothing of the local gradient by conversion processes or due to incoming solar radiation at sunrise. The formation of each frontogenesis is defined by the frontogenetic function **F** (after Miller 1948):

$$\mathbf{F} = \frac{d}{dt} |\nabla \Theta| \tag{4.1}$$

Frontogenesis can be derived from the conservation equation of thermal energy with respect to x:

$$\frac{d}{dt}\left(\frac{\partial \Theta}{\partial x}\right) = -\frac{\partial u}{\partial x}\frac{\partial \Theta}{\partial x} - \frac{\partial v}{\partial x}\frac{\partial \Theta}{\partial y} - \frac{\partial w}{\partial x}\frac{\partial \Theta}{\partial z} + \frac{\partial}{\partial x}\nabla H \tag{4.2}$$

∇H is the divergence of the turbulent sensible heat flux:

$$\nabla H = \frac{\partial H_1}{\partial x} + \frac{\partial H_2}{\partial y} + \frac{\partial H_3}{\partial z} \tag{4.3}$$

with:

$$H_1 = \bar{\rho} K_{Hh} \frac{\partial \bar{\Theta}}{\partial x},\ H_2 = \bar{\rho} K_{Hh} \frac{\partial \bar{\Theta}}{\partial y},\ H_3 = \bar{\rho} K_{Hv} \frac{\partial \bar{\Theta}}{\partial z} \tag{4.4}$$

The first term on the right hand side describes the horizontal deformation, the second one the horizontal shearing and the vertical shear is represented by the third term. Due to the thermally driven density current, we consider the diabatic heating with the last term on the r. h. s., which is induced by the turbulent exchange of sensible heat (H) between the surface and the lower levels of the atmosphere. The horizontal K_{Hh} and vertical K_{Hv} mixing coefficient is determined by the 1.5 order turbulent kinetic energy (TKE) based closure scheme. With an increase of the first term on the r. h. s. the deformation increases and hence the temperature gradient as well. This leads to an enhancement of the vertical shearing and stronger inclined isotherms, which strengthen the frontogenesis ($\mathbf{F} > 0$). Turbulent and convective processes induce the disintegration of the front while smoothing the gradient through the vertical release of heat and momentum ($\mathbf{F} < 0$).

4.2.2 Model Set-up

For the simulation of an idealised surface front and subsequent formation of convective cloud systems, the Advanced Regional Prediction System (ARPS) was used. It was developed at the Center for Analysis and Prediction of Storms (CAPS) at the University of Oklahoma. ARPS is a fully-compressible, non-hydrostatic numerical model with a generalised terrain-following coordinate system and vertical stretched grid. For more details, see Xue et al. (1995, 2000, 2001).

A 108 km model domain with a horizontal resolution of 500 m, which is sufficient to resolve explicit simulations of moist convection (Xue and Martin, 2006) was used. The 65 vertical layers have an average spacing of 250 m and are stretched to a minimum of 15 m near the ground with a hyperbolic function. The minimum vertical grid spacing is maintained for the lowest 300 m in order to engage the formation of a thermally-induced density current in the PBL. An idealised terrain model was used to simulate a katabatic induced surface front. It features the main structures of the Andes in the target area, e. g. a concave formed ridgeline disconnected by several mountain peaks and a drainage system into a basin (see figure 4.1 upper right).

The top boundary conditions of the domain were set to a rigid wall with a radiative damping layer at 15000 m to prevent unrealistic reflections. The lateral sides had radiation-open conditions of the Klemp and Wilhelmson type (Klemp and Wilhelmson, 1978) for constant phase speed, that was computed and applied at each time step. The simulations were initialised with an ideal sounding derived from a tropical model atmosphere (McClatchey et al., 1972), and adjusted with an approximately neutral temperature stratification in the lower atmosphere and a lightly stable profile in the upper atmosphere containing sufficient moisture for cloud development. To avoid any stream flows overlaying the thermally-induced flow at the beginning of the simulation, the windfield is set to zero. The radiative cooling necessary for the katabatic flow is considered through atmospheric radiation transfer parametrisation. It is the primary force of the heat energy budget and includes the net radiation, sensible heat flux and ground heat flux into the surface.

A detailed model setup of the physics used for the katabatic flow can be found in (Trachte et al., 2010). An essential modification to the initialisation of the model is the use of an explicit microphysic parametrisation scheme (Lin et al., 1983). Six prognostic equations are solved for water vapour, cloud water, rain water, cloud snow, cloud ice and grauple. Due to the high horizontal resolution of the domain, no cumulus parametrisation scheme was used.

4.3 Results

An idealised terrain model was used to examine the development of a surface cold front and sequentially convective activities. The mesofront was induced by a density flow from the slopes and valleys into a basin, where the cold air produced a horizon-

tal temperature gradient. First, the main characteristics of the density current and its relation to a katabatic flow are shown. The formation of a surface cold front on the basis of this current is demonstrated with cross-sections of the potential temperature overlayed with vertical velocities. Afterwards, the development of convective weather systems is analysed and discussed in the context of divergence fields and stability parameters.

4.3.1 Density Current and Surface Front

First we begin by identifying the density current. Figure 4.2 shows the cross-section of the horizontal wind speed with the *TKE* at time step 17100 s. The current flows down along a slope into the basin (see figure 4.1) with velocities around 3 m·s^{-1}. At its leading edge, the typical elevated region occurs called the head. It is larger than the following tail and the primary effect in the lifting of air (see Liu and Moncrieff, 2000). At the head, the velocities increase to values around 5.5 m·s^{-1}. The wind field appears clearly deformed caused by the density difference between two fluids. It is a region of intensive mixing, which is confirmed by the *TKE*.

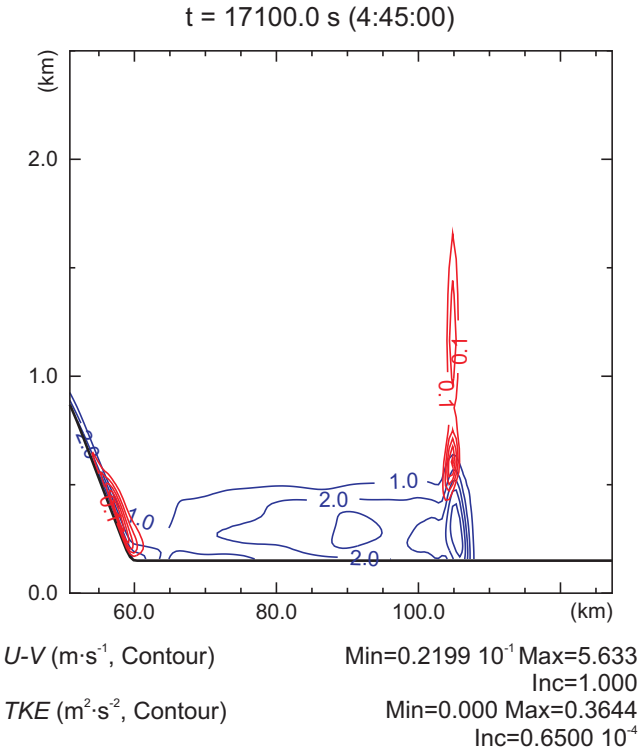

Figure 4.2: Vertical cross-section (xz plots from x = 36.0 km, y = 36.0 km and x = 100.0 km, y = 100.0 km) of the wind speed in *u*-*w* direction (contour, blue, m·s^{-1}) and *TKE* (contour, red, m^2·s^{-2}) for time step 17100 s

Above the head values of 0.3 $m^2 \cdot s^{-2}$ occurs reaching a height of 1.7 km. It results from the convergence zone opposing the tendency to generate a strong horizontal gradient. Along the slope a *TKE* of 0.3 $m^2 \cdot s^{-2}$ occurs as well. This mixing is induced by vertical wind shear due to the downslope current and develops only in the lowest levels.

The presented density current is a thermally-induced katabatic flow, which is demonstrated in the following figures (figures 4.3, 4.4). Typical features of the flow are presented in figure 4.3 for time step 4800 s and 17100 s: the potential air temperature profile (figure 4.3 a) shows the development of a positive temperature gradient in the lower atmosphere with 2 $K \cdot m^{-1}$ separating the katabatic layer from the free atmosphere. The wind velocity in u-direction (figure 4.3 b) forms the typical jet-like profile with maximum wind speeds of 4.3 $m \cdot s^{-1}$ near the ground level, where the influence of the temperature gradient is strongest. Above the katabatic layer decreasing of the temperature gradient leads to a decline in wind speeds. *TKE* (figure 4.3 c) is induced at levels where the vertical shear has its maximum and reaches values of 2.3 $m^2 \cdot s^{-2}$.

An indicator for the evolution of the katabatic flow is the heat energy budget, since the driving mechanism is a buoyancy deficit by radiation divergence associated with ground heat fluxes. Figure 4.4 shows a negative net radiation Rn during the simulation time that remains constant around 75 W m^2 after the first hour. Correspondingly a negative sensible heat flux H is observed indicating an energy flux from the atmosphere to the surface layer. Thus, the PBL is constantly cooled decreasing the temperature deficit between the atmosphere and the surface. As a result of this temperature deficit the ground heat flux G reaches negative values of 30 $W \cdot m^{-2}$ as well. The heat energy budget confirms the development of a thermally-induced katabatic flow in conjunction with its typical characteristics. The flow is sustained as long as the net radiation is negative. For more details on the development of the katabatic flow and its behaviour due to the shape of the terrain see Trachte et al. (2010).

So a current is initiated by radiative cooling, inducing a thermally driven flow along the slopes (figures 4.2, 4.3 and 4.4). The cold drainage air propagates into the basin (3 $m \cdot s^{-1}$), where it converges with less cold air, causing a horizontal temperature gradient. Due to the driving force of the surface fluxes, the velocities are only recognised in the lowest 500 m of the atmosphere; the ambient atmosphere is calm and undisturbed. The interface between the two fluids is a typical frontal zone with intensive mixing and vertical velocities (Eliassen, 1959). The katabatic flow causes a discontinuity in the density and potential temperature distribution inside the basin, which leads to modifications such as a deformed horizontal wind field and inclined isotherms, which foster the frontogenesis ($\mathbf{F} > 0$). The result is a secondary vertical circulation with upward and downward motion.

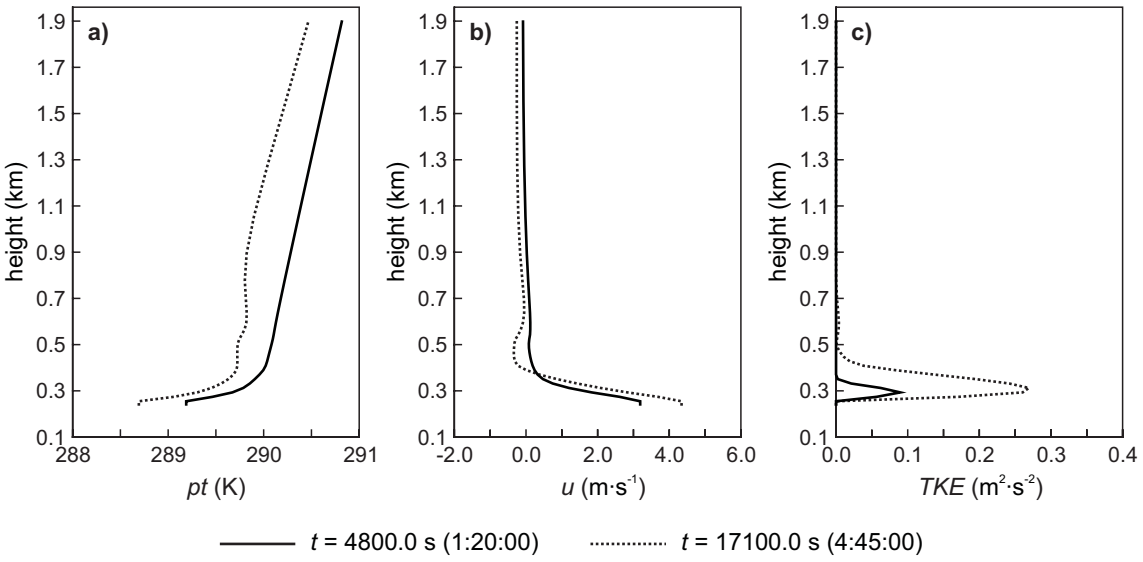

Figure 4.3: Profiles of (a) the potential temperature (*pt)*, (b) the wind vector (u) and (c) the turbulent kinetic energy (TKE) taken at x = 24.5 km and y = 78.0 km for the time steps 4800 s and 17100 s

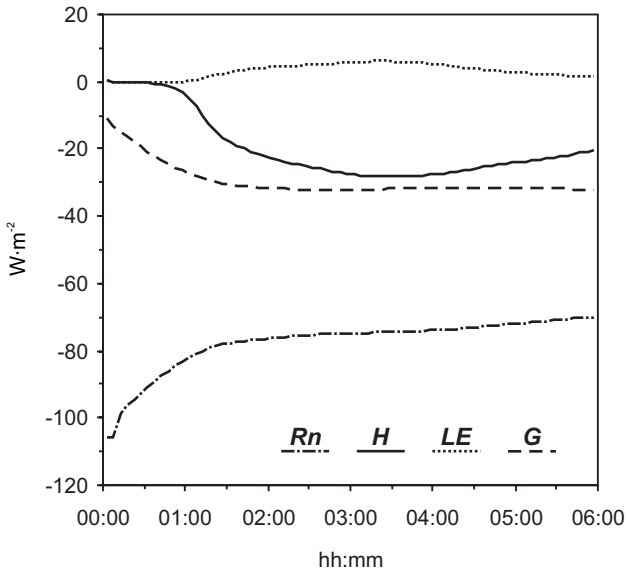

Figure 4.4: The heat energy fluxes in W·m^{-2} with the net radiation (Rn), the sensible heat flux (H), the latent heat flux (LE) and the ground heat flux (G) as a function of simulation time between 0 and 6 hours taken at x = 24.5 km and y = 78.0 km

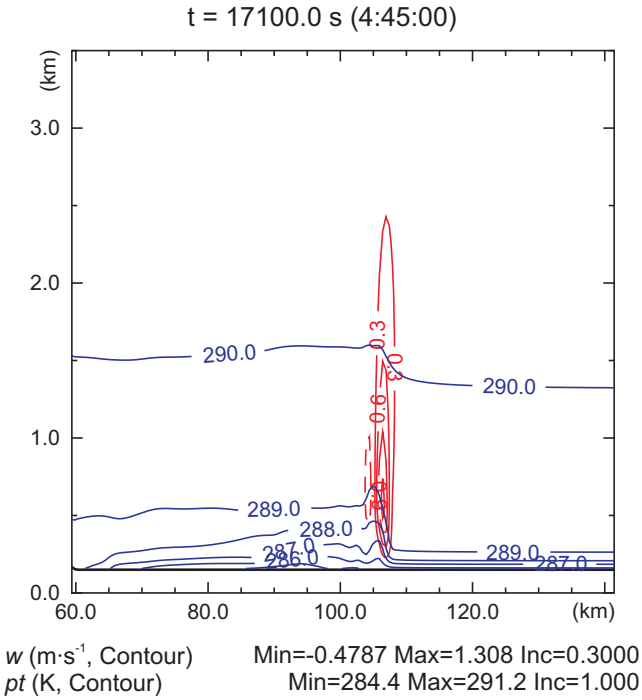

Figure 4.5: Vertical cross-section (xz plot from x = 42.0 km, y = 42.0 km and x = 100.0 km, y = 100.0 km) of the potential temperature (*pt*, contour, blue, K) and the wind field in *w* direction (contour, red, m·s^{-1}) for time step 17100 s

Fig 4.5 shows the cross-section of the potential temperature overlayed with the vertical wind field at time step 17100 s. In doing so, solid lines of the wind field represent ascending and dashed lines descending air. In the region where the head was located (106 km) the isotherms are tilted indicating the surface cold front. Also noticeable is the advance of cold air into the basin, creating a horizontal temperature gradient of approximately 2 K near surface. Because of the persistent flow, the propagation of cold air into the basin is sustained, increasing the temperature difference. It is a direct response to the constant heat sink due to the surface energy budget (see Thorpe et al., 1980). That, in turn, enhances the deformation of the horizontal wind field and stronger inclined isotherms, resulting in the strengthening of the frontogenesis (see equation 4.2). This implicates that the deformation of the wind field significantly contributes to the frontogenesis. At the leading edge, upward motion of approximately 1.3 m·s^{-1} developed. Behind the front, a descending branch of 0.47 m·s^{-1} formed coincide with the turbulent mixing in figure 4.2. It appears that the modifications of the thermal energy distribution result in dynamic effects, e.g. turbulent mixing and vertical motions as a counteracting process. However, the extent of the wind field in *w* direction is insignificant and not sufficient to initiate moist convection. It is instead a consequence of the development of a surface inversion through net radiation loss, which is demonstrated by the calm ambient at-

mosphere. This clearly shows that an additional trigger mechanism in the PBL is necessary to initiate stronger vertical motion with the formation of convective cloud systems, which is analysed in the following sections.

4.3.2 Atmospheric Environmental Parameters

Environmental parameters that determine whether the atmosphere induces convection are, e.g. convective inhibition (*CIN*) (Colby, 1984) and the convective available potential energy (*CAPE*) (Moncrieff and Miller, 1976). The *CIN* is the net work per unit mass required to lift a negative buoyant parcel from the surface to the level of free convection (*LFC*) and is defined by:

$$CIN = -\int_{z_{sfc}}^{z_{LFC}} g\left(\frac{\Theta_{par} - \Theta_{env}}{\Theta_{env}}\right) dz \tag{4.5}$$

with Θ_{par} as the potential temperature of the parcel lifted from the surface (z_{sfc}) up to the *LFC* (z_{LFC}) and Θ_{env} the ambient potential temperature. The *CAPE* is the net work per unit mass performed by the environment on a parcel which ascends from the *LFC* to the equilibrium level (EL) and is given by:

$$CAPE = \int_{z_{LFC}}^{z_{EL}} g\left(\frac{\Theta_{par} - \Theta_{env}}{\Theta_{env}}\right) dz \tag{4.6}$$

It describes the maximum energy available to an ascending air parcel and is an indicator for the potential instability of the atmosphere.

Table 4.1: Environmental parameters

	initial state	time step 18000 s
CAPE	2352 J·kg^{-1}	955 J·kg^{-1}
CIN	0 J·kg^{-1}	-71 J·kg^{-1}
LFC	591 (m AGL)	1461 (m AGL)
K-Index	30	33
LI	-10.9	-4.6

Table 4.1 represents the *CAPE* and *CIN* with some additional stability indices to examine atmospheric instability and the possibility to induce deep convection for the initial state and time step 18000 s. In the beginning, there is no negative buoyancy ($CIN = 0$ J·kg^{-1}) in the PBL, which must be overcome. The amount of *CAPE* is 2352 J·kg^{-1}, which is sufficient to initialise moist convection and generate a cloud cluster (Robee and Emanuel, 2001). The *K-Index* is an indicator for the potential of the formation of a thunderstorm. It is based on the lapse rate and the water

vapour content in the atmosphere. A value of 30 at the beginning of the simulation demonstrates the great potential for deep moist convection. Associated with the Lifted Index (LI) of -10,2, which characterised an extremely unstable atmosphere, the probability of the formation of a multi-cell thunderstorm is quite clear. The *LFC* is located at 591 m AGL (above ground level).

We used such an unstable idealised sounding to demonstrate the impact of the configuration of the terrain on the generation of convective clouds. After 18000 s simulation time, no convective activity occurred. The *CAPE* decreases considerably to an amount of 955 J·kg^{-1} with a simultaneous increase of the *CIN* to -71 J·kg^{-1}. It is based on the net radiation loss, which results in the formation of a surface inversion, inducing negative buoyancy (see figures 4.3 and 4.4). The LI also decreases (-4.6) due to the cooling, but the atmosphere remains unstable. The *K-Index* has a value of 33, further indicating the potential for the development of a severe cloud cluster. Nonetheless, at that time the atmosphere is calm and lacking any vertical motions as already shown in figures 4.2 and 4.5.

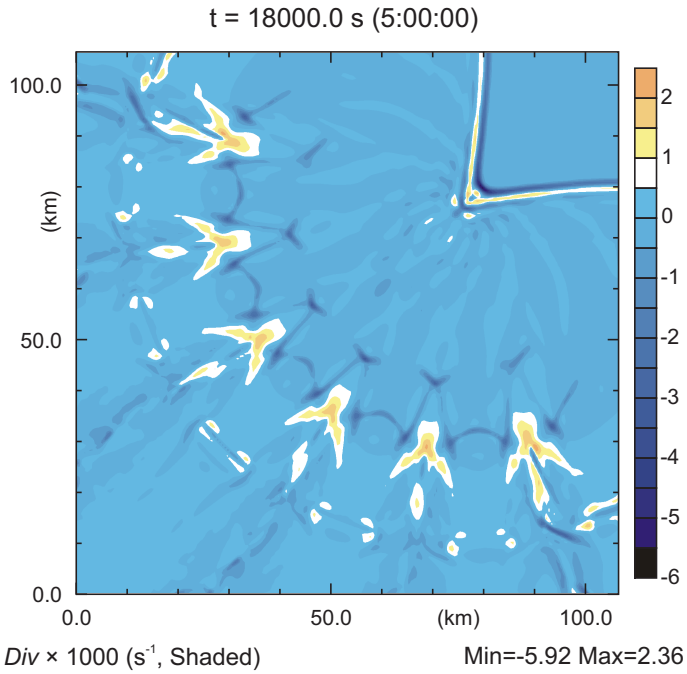

Figure 4.6: Horizontal cross-section (xy plot at z = 50 m above ground level) of the divergence field (*DIV*, shaded, s^{-1} amplified by a factor of 1000) for time step 18000 s

In addition to the presented environmental conditions, the initiation of convective activity is a function of the horizontal divergence field. Despite the already displayed vertical velocity in figure 4.5 we used this parameter to demonstrate the horizontal distribution considering the impact of the concave terrain. Convergence lines cause an increase in the mass field, which induces upward motion. To reach the *LFC* and initiate deep moist convection outside the nocturnal boundary layer (NBL), which

must be overcome, sufficient moisture in the atmosphere is required. In a NBL with an inversion near the ground, as developed in our simulations, an additional mechanism for trigger ascent is beneficial.

Figure 4.6 illustrates the horizontal divergence field (shaded) at time step 18000 s. Negative values describe convergences and positive values represent divergence of the horizontal wind field. At the exit regions of each valley, strong divergence patterns ($2.3*10^{-3}$ s^{-1}) develop. This is caused by the drainage flow, which can spread when it enters the basin. Further into the basin, the flow converges with values of $2.5*10^{-3}$ s^{-1}. Along the boundary of the potential temperature difference in the basin, as shown in figures 4.2 and 4.5, a zone with an alternating converging ($4*10^{-3}$ s^{-1}) and diverging field ($1.5*10^{-3}$ s^{-1}) developed. However, the strongest convergence with $5.9*10^{-3}$ s^{-1} occurred in the centre of the basin as a result of the confluence of the terrain configuration. Together with the other parameters presented above, it indicated that the concave geometry of the topography acts as a trigger for convective initiation and is further analysed in the next section.

4.3.3 Formation of Convective Clouds

Another parameter to analyse the atmospheric situation at hand is the Bulk Richardson Number (BRN) as an indicator for the convective storm type (Weisman and Klemp, 1982). Several types of convective clouds can be formed. The basic thunderstorm is a single cell, which is less strong. Severe thunderstorms are multi-cell formations such as MCS. They are defined by an organised ensemble of convective cells, develop worldwide and vary in size and shape (Bluestein and Jain, 1985; Jirak et al., 2003). The BRN is the ratio of $CAPE$ and the vertical wind shear, which is defined by one-half the square of the difference between the 6 km mean wind field and the mean surface layer (500 m) wind speed:

$$BRN = \frac{CAPE}{\frac{1}{2}[(\bar{u_6} - \bar{u_{0.5}}^2) + (\bar{v_6} - \bar{v_{0.5}}^2)]} \tag{4.7}$$

Low values (< 10) indicate that vertical shear dominates and inhibits convection. Values between 10 and 45 represent an unstable atmosphere, which fosters updraughts and favours strong convective cells. A BRN above 45 supports strong convective supercells. Along cold fronts, conditions are favourable for deep moist convection, so that MCS form particularly often in these regions (Bluestein and Jain, 1987).

In figure 4.7, the BRN (contours) is shown at time step 19800 s, 1800 s further in simulation time as shown before in table 4.1 and figure 4.6. The greatest values, reaching approximately 14, are generated in the centre of the basin. These values increase during the simulation. It is the same location where the strongest convergences occurred (see figure 4.6) and forms a quasi-radial pattern. Due to the high BRN, when the vertical wind shear is low compared to the , indicating deep

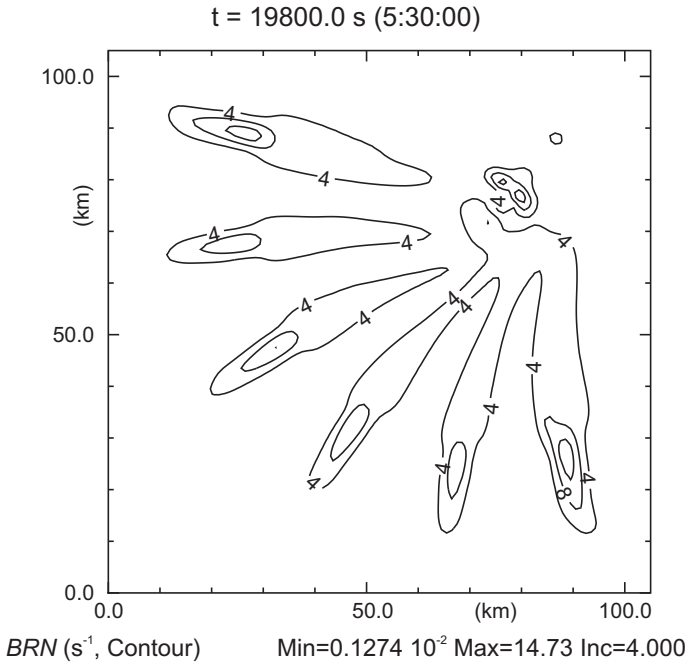

Figure 4.7: Horizontal cross-section (xy plot at z = 50 m above ground level) of the Bulk Richardson Number (*BRN*, contour) for time step 19800 s

moist convection, the formation of a strong thunderstorm is likely, particularly in view of the environmental parameters. Correspondingly high values occur at the exit regions of each valley, as already indicated by the horizontal divergence field in figure 4.6. But in those regions, the *BRN* ceases to grows.

In order to examine the occurrence of the cloud cluster in the basin, we take a closer look at its development in figure 4.8 a-d. Here we see the moisture convergence (shaded), the wind field in *uw* direction (vectors) and the total amount of condensed water (solid line) for the beginning and the three developing stages in a vertical cross-section. In figure 4.8 a at simulation time 18000 s, the described density current can be identified by the vectors in the PBL. The atmosphere is calm and lacking any strong vertical motion (0.66 $m \cdot s^{-1}$), as shown in previous figures and despite the high probability of convective activity that was analysed above. In the region where the surface front is located (x = 110.0 km), an intense convergence of moisture ($19.5*10^{-3}$ $(g \cdot kg^{-1}) \cdot s^{-1}$) has taken place in the lower levels of the atmosphere. In the next displayed time step (19800 s), this convergence forces a significant updraught with maximum values of 15.82 $m \cdot s^{-1}$ (figure 4.8 b). The lifting air parcels reach the *LFC* (1461 m AGL), which is made clear by their vertical acceleration. They achieve a height of 9 km. The strong vertical motions result in the formation of a tower in its cumulus stage, distinguishable by its buoyant plume. Entrainment of air occurs at the top of the cloud.

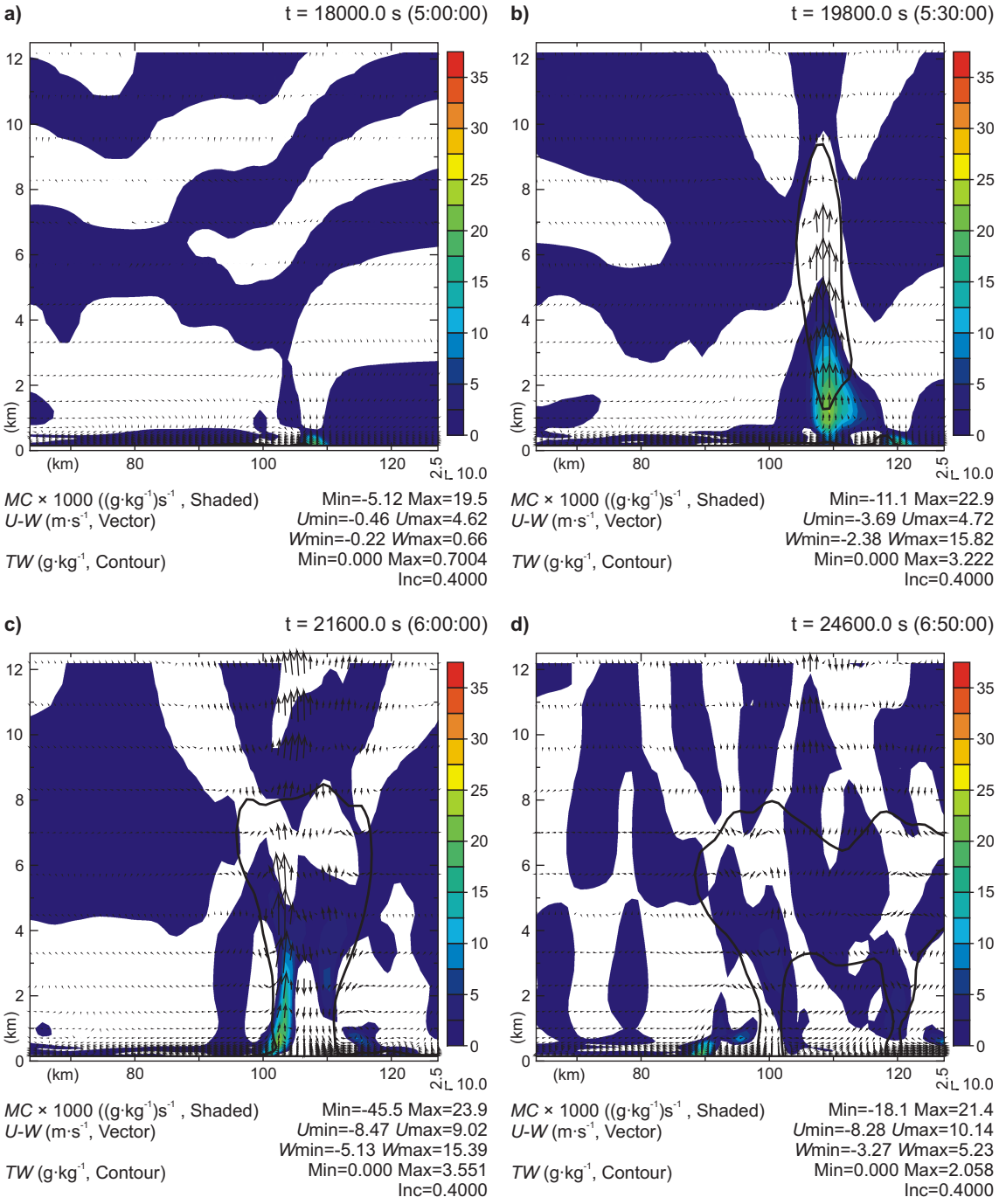

Figure 4.8: Vertical cross-section (xz plot from x = 45.0 km, y = 45.0 km and x = 100.0 km, y = 100.0 km) of moisture convergence amplified by a factor of 1000 (MC, shaded, $(\mathrm{g{\cdot}kg^{-1}}){\cdot}\mathrm{s^{-1}}$), the wind field in u-w direction (vectors, $\mathrm{m{\cdot}s^{-1}}$) and the total condensed water (TW, solid line, $\mathrm{g{\cdot}kg^{-1}}$) for time steps a) 18000 s, b) 19800 s, c) 21600 s, d) 24600 s

It should be stated, that the purpose of the idealised case study at hand is to demonstrate the impact of the terrain configuration on convective initiation: it is for this reason that we used an extremely instable sounding, producing such vertical motions.

In the ongoing simulation time (21600 s), the cumulus tower grows in depth and develops into a multi-cell thunderstorm in its mature stage (figure 4.8 c), which achieves a vertical height of 8 km. The moisture convergence reveals two cores in different conditions, interrupted by downbursts (5.13 $m \cdot s^{-1}$) of cold air in the central portion of the cloud system, particularly in the lower region. We find an old dissipating core on the frontside of the cloud, characterised by local updraughts and strong downdrafts, which result in the formation of an extensive precipitation pattern and a gust front at the leading edge. At the rear, cell regeneration occurs, strengthening the cloud cluster due to surface convergence of moisture. It is added into the basin as a result of the drainage system regime. The new cell manifests itself with intense moisture convergence of $23.9*10^{-3}$ $(g \cdot kg^{-1}) \cdot s^{-1}$ and significant updraughts with maximum values of 15.39 $m \cdot s^{-1}$. Also, entrainment of air is enhanced and located now at the sides and top of the cloud system. After additional 50 minutes of simulation time (24600 s), the cloud cluster begins to dissipate (figure 4.8 d). The strong updraughts are replaced by local upward motions in the upper part of the cloud with values of 4 $m \cdot s^{-1}$. The lower area is dominated by downward motions, which have velocities of approximately 2 $m \cdot s^{-1}$. Two separate precipitation patterns are visible through the condensed water reaching the ground. The release of latent heat results in the smoothing of the temperature gradient caused by the thermally driven katabatic flow. Due to the lack of moisture convergence in the PBL, the updraughts are no longer triggered and the dissipation of the cloud cluster and the frontolysis ($\mathbf{F} < 0$) takes place.

Impact of a Low Level Jet

Nocturnal LLJ are low tropospheric currents, which benefit from the formation of a surface inversion such as that shown in our simulation results. They have a great impact on moisture transport and are involved in nocturnal convective activities. At their nose they increase the low-level convergence, which can induce the rise of air and moist convection and the development of MCS (Valesco and Fritsch, 1987; Gandu and Geisler, 1991; Marengo et al., 2002).

In order to investigate the impact of a nocturnal LLJ on the occurrence of a katabatic induced cloud system represented above, we initialise this simulation with an additional regional wind field. The LLJ in our simulations is approximated as a fast moving current in the lower troposphere with velocities of approximately 10 $m \cdot s^{-1}$, a strong vertical shear and a horizontal extension of 5 km. Apart from the horizontal width, we consider its common characteristics (Bonner, 1968).

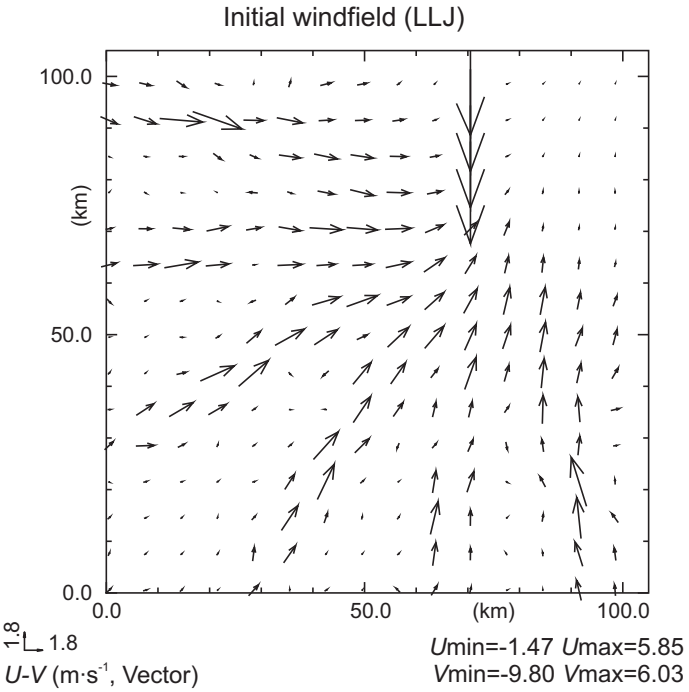

Figure 4.9: Horizontal cross-section (xy plot at z = 200 m above ground level) of the initial wind field in u-v direction (vectors, m·s^{-1})

Figure 4.9 shows the initial wind field (vectors) for the simulations. Here we see the simulated katabatic flow at time step 18000 s, together with a local LLJ. The jet is clearly distinguishable by the stronger southerly current focused on the centre of the basin. Its direction is derived form the situation in the Amazon basin and the eastern Andes, where the terrain acts as a barrier that diverts forming jets to the south. In the analysis of the interaction between the katabatic induced convective activity and the exit region of a LLJ, we were confronted with the problem that we were unable to develop both flow systems in one simulation at two different time intervals in an idealised run. Therefore, we placed the jet into the katabatic wind field shown in the results above (see figures 4.2 - 4.8,) by merging of two soundings. As a result of this approach we obtain a data set with the initial wind field shown on figures 4.9 and the ambient conditions of the katabatic influenced atmosphere presented above. This brute force of putting the jet into the model is to demonstrate its impact on the initiation of convection rather than the examination of the development of the jet itself.

In figure 4.10 the *BRN* is displayed at time step 2700 s, which corresponds with the time step of the previous simulation. As with the simulation without the LLJ, the highest values of *BRN* occur in the centre of the basin. There, two semicircular areas opposite each other are arranged with convective zones. This location also correlates with the region of strong convergences in the wind field (see figure 4.6)

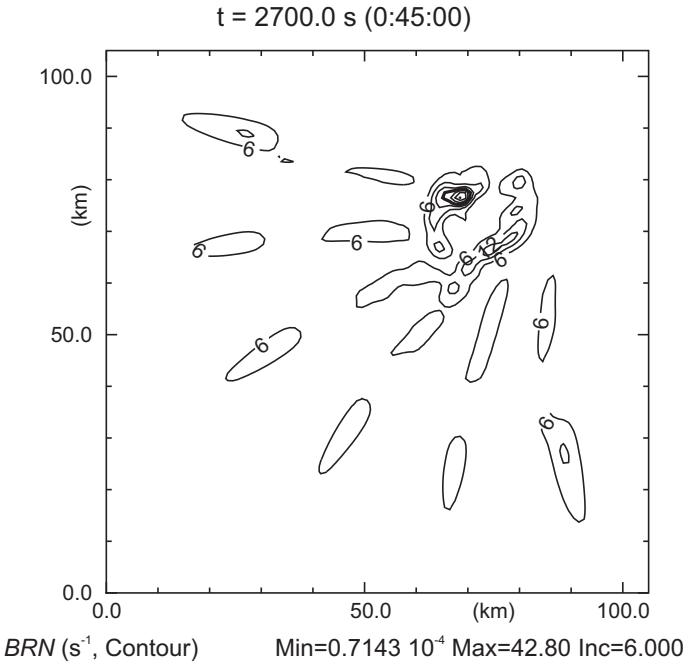

Figure 4.10: Horizontal cross-section (xy plot at z = 50 m above ground level) of the Bulk Richardson Number (*BRN*, contour) for time step 2700 s

and additionally with the exit region of the LLJ. However, in this simulation the *BRN* achieves values of 42, which suggests the formation of a severe multi-cell. The probability of the formation of a multi-cell thunderstorm is especially high in comparison with the previous *BRN* of 14. The faster development is driven by stronger convergences and more advection of moisture, which intensifies the lifting of air. Hence, more convective cells are initiated.

The formation of these convective cells is shown in figure 4.11 a-c, comparable to figure 4.8 b-d. Here we see the moisture convergence (shaded), the vertical velocities in *u*-*w* direction (vectors) and the condensed water (solid line) as well. Figure 4.11 a shows two regions with strong moisture convergences ($35*10^{-3}$ $(g \cdot kg^{-1}) \cdot s^{-1}$) in the lower atmosphere close to the region of the surface front. The more mature convergence zone is located at x = 104.0 km. It forces a significant updraught of 30 $m \cdot s^{-1}$, which is 10 $m \cdot s^{-1}$ greater than before (see figure 4.8 b). These strong vertical motions were already indicated by the high *BRN* of 42 (see figure 4.10). They generate a convective tower, which reaches a height of 10 km AGL. The second moisture convergence zone at the surface develops at x = 96.0 km. It starts to grow and reaches a height of approximately 3.5 km. Vertical velocities of 15 $m \cdot s^{-1}$ are obtained. Thus both convective cells are in their cumulus stage, as shown by the small buoyant plume. After further 25 minutes of simulation time the separated cumulus cells combine to a cloud cluster in its mature stage (figure 4.11 b) reaching a height around 10 km.

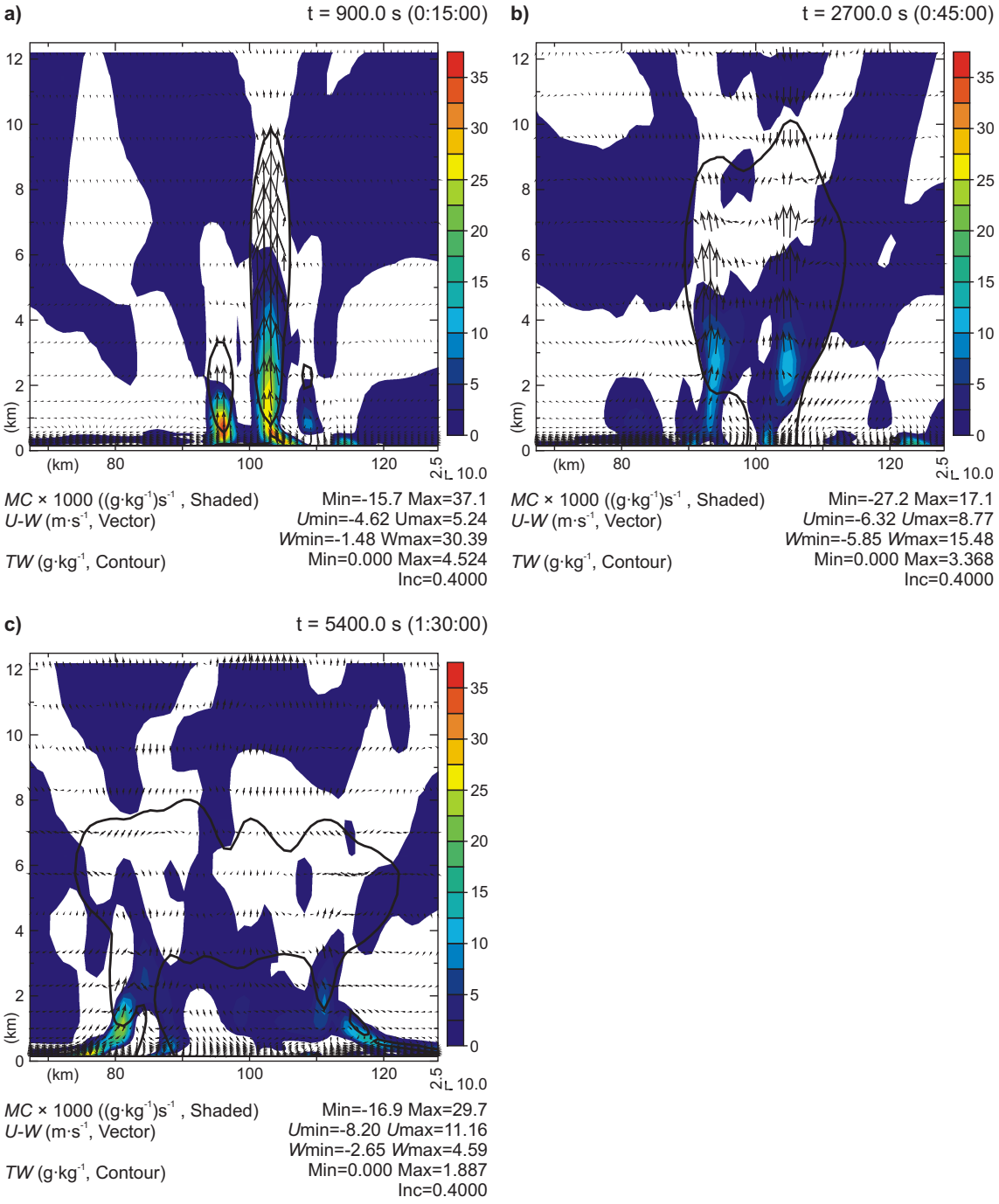

Figure 4.11: Vertical cross-section (xz plot from x = 45.0 km, y = 45.0 km and x = 100.0 km, y = 100.0 km) of moisture convergence amplified by a factor of 1000 (MC, shaded, $(\mathrm{g{\cdot}kg^{-1}}){\cdot}\mathrm{s^{-1}}$), the wind field in u-w direction (vectors, $\mathrm{m{\cdot}s^{-1}}$) and the total condensed water (TW, solid line, $\mathrm{g{\cdot}kg^{-1}}$) for time steps a) 900 s, b) 2700 s, c) 5400 s

Two strong cores can be identified by the moisture convergences. The cloud is dominated by strong updraughts, which have velocities of 15 $m \cdot s^{-1}$. Downdrafts of 4.8 $m \cdot s^{-1}$ in the lower region result in precipitation patterns, as shown by the condensed water reaching the ground. Strong downbursts (5.8 $m \cdot s^{-1}$) are found at the leading edge, feeding the cell regeneration. A rearward inflow of moist air from the drainage system flow and the LLJ nourish the convective cells as well. Entrainment of air occurs at the top and the lateral sides. After 50 minutes of simulation time, a large cloud develops, but only reaches a height of 8 km AGL (figure 4.11 c). The strong updraughts are replaced by local upward motion, which have approximate velocities of a mere 4.5 $m \cdot s^{-1}$. In the lower atmosphere downward motions prevail. The main precipitation area is situated rearward, where strong moisture convergence ($29*10^{-3}$ $(g \cdot kg^{-1}) \cdot s^{-1}$) still occur. However, this advection can not prevent the dissipation of the cloud system, as shown by the rather weak vertical motions compared to the cumulus and mature stage in figure 4.11 a, b.

4.4 Discussion

As hypothesised above, the confluence of katabatic flows as a result of the configuration of the terrain leads to convective initiation, provided that sufficient moisture is present in the atmosphere. As a result of diabatic heating of the surface (see figure 4.4), which acted as the main driver for the frontogenesis, the air began to flow down the slopes and valleys into the basin. The characteristics of a density current and its reasons for development were revealed by a cross-section plot of the horizontal wind speed (see figure 4.2) and the typical features of a katabatic flow (figures 4.3, 4.4). At its leading edge, a head developed, clearly larger than its following tail, as well as a noticeable deformation of the wind field. Nevertheless, the vertical mixing, which developed in this region, was rather small, indicating the development of a surface inversion as a result of the radiative cooling of the lower atmospheric levels.

Inside the basin, the current generated a temperature / density difference due to the propagation of cold drainage air driven by the heat energy budget. The interface between both fluids was a typical frontal zone as demonstrated in figure 4.5. The features of the frontal zone were examined by the vertical distribution of the potential temperature. The isotherms showed their characteristic inclination, causing baroclinicity. The flow was persistent, which caused a continuous transport of cold drainage air into the basin and thus increasing the gradient. This in turn caused a more deformed horizontal wind field with more strongly inclined isotherms. Hence, the strengthening of the frontogenesis is implicated, whereas the deformation term (equation 4.2) of the frontogenetic function acted as a strong contributor. However, the consequentially induced ascending branch at the leading edge and the descending edge behind were rather shallow, as already indicated by the *TKE*, and no initiation of any lifting occurred to this point.

Considering that the simulation was initialised with a homogeneous state and that the environmental parameters (see table 4.1) revealed the high potential for deep moist convection, even after the development of a strong surface inversion, an additional trigger mechanism in the PBL must exist. This effect was also demonstrated by (Rasmussen and Blanchard, 1998), who made a classification for sounding-derived supercells. The authors had a large number of false alarms, which they related to the fact, that there are many factors influencing the formation of supercells, even when the sounding suggests its development.

In our case, the crucial factor for the initiation of deep convection is the confluence due to the concave terrain configuration. With the horizontal divergence field in figure 4.6 we were able to observe the development of a surface cold front along the concave terrain line inside the basin. But it was also evident that the terrain forced the katabatic flow to confluence in the centre of the basin, where the strongest horizontal divergence values occurred. Indeed, at the time when the confluence was greatest in the basin, the air was lifted and moist convection initiated. The *BRN* in the same region showed values of 14 at this time step, which favoured the development of a multi-cell thunderstorm. The formation of such a storm was analysed by its developmental stages with the moisture convergence pattern, the wind field in *u*-*w* direction and the condensed water. A convective cell developed due to sufficient moisture in the atmosphere. It grew in depth and evolved a cloud cluster with several cores (figure 4.8). Additionally, the permanent inflow of cold moist air by the drainage system regime initiated more convective cells in the rear. In the ongoing simulation the cells dissipated as a result of the release of latent heat and the absence of further propagation of moisture due to the boundary conditions.

We examined the impact of a LLJ as an additional trigger mechanism in the PBL for the formation of cloud systems. To do this, we placed a fast moving current above our NBL in the simulated horizontal wind field just before convective initiation, so that we gain the atmospheric conditions of the previous run combined with a new wind field including the LLJ. A first comparison of the *BRN* of both simulations showed the differences. While the simulation without a LLJ reached a *BRN* of maximum 14 (figure 4.7), the LLJ produced a *BRN* of maximum 42 (figure 4.10). Particularly remarkable is the difference in the chronological order. The simulation without a LLJ needed more time to evolve a strong multi-cell with respect to the convective initiation time. At the beginning it formed only a single cumulus cell, which, as time progressed, resulted in a cloud cluster. The simulation with a LLJ developed to a severe multi-cell storm more rapidly, which is evident by the *BRN*. However, this high value is driven by a modification in the lower atmosphere, which affected the dynamic behaviour of the horizontal wind field. In particular, the LLJ caused additional moisture advection and enhanced low level convergence in its exit region. This process intensified the low level atmospheric instabilities, which foster lifting of air. In fact, the results of the simulation with a LLJ as an additional trigger mechanism showed the development of a stronger multi-cell which is at an

earlier stage (figure 4.11). The vertical velocities exceeded the values of the previous simulation by 10 $m \cdot s^{-1}$. This is the reason that a deeper cumulus tower arose at the beginning, which overshot the one in figure 4.8 by approximately 2.0 km. The horizontal extension is also outbalanced. Due to the greater extent of moisture contribution to the instability zone, an improved cell regeneration and initiation were affected.

But despite these facts, the vertical motion displayed in figure 4.8 was only initiated on the basis of the horizontal divergence field. There was no additional moist air mass contribution, which intensified the low level instabilities in the atmosphere. Nevertheless, a considerable cloud cluster, consisting of several convective cores, was generated, although its formation needed more simulation time. This leads to the conclusion that the development of an idealised multi-cell thunderstorm occurred primarily due to the concave configuration of the terrain.

4.5 Summary and Conclusions

The mesoscale model ARPS was used to investigate the development of a katabatic induced local cold front and the formation of convective cloud systems. We hypothesised that the formation is associated with the special topographical configuration in our target area, i.e. a concave terrain line. We used an idealised terrain model representing an approximation of the eastern Andes with a concave ridgeline divided by several valleys draining into a basin.

The horizontal wind field, the potential temperature profile and the heat energy budget were used in order to present the density current driven by radiative cooling of the surface and the resulting katabatic induced surface cold front. They illustrated characteristic features, such as a head at the leading edge, a jet-like profile and inclined isotherms. But they also demonstrated with their rather small vertical velocities and *TKE* values that an additional trigger mechanism is necessary to initiate deep convection. This effect was supported by the environmental conditions in the basin. They indicated a very unstable atmosphere, but no convection was initiated until the horizontal divergence field became stronger in the centre of the basin forcing the air to lift. In the same region the *BRN* reached values of 14, which is indicative for deep convection. Analyses of the moisture convergence, the wind field in *uw* direction and the condensed water confirmed this result. Convection was initiated in this area when a strong convergence of the horizontal wind field occurred and the *BRN* value gained a large value, respectively. This resulted in the development of a multi-cell thunderstorm due to the continuous propagation of moisture by the drainage system. In addition, the impact of a nocturnal LLJ was examined. The jet produced an intensification of the low level atmospheric instability with an additive moisture contribution. The results were stronger updraughts and the generation of a larger cloud system.

The approach presented above led to the conclusion that the concave geometry of the topography is responsible for extensive lifting of air based on strong convergences in the basin. It results in the formation of a convective cloud system, which is nourished by the thermally driven flow propagating moisture into the convective area. The presence of the LLJ as an additional factor fosters the occurrence of the cloud cluster and the development of a more severe thunderstorm. Hence, the results of the study at hand verify our above stated hypothesis, that katabatic flows act as a local cold front, inducing deep convection due to the concave configuration of the topography and that a nocturnal LLJ act as a catalyst for the given situation.

Acknowledgment
The authors are indebted to the German Research Foundation (DFG) for the funding of the work in the scope of the Research Unit RU816 'Biodiversity and Sustainable Management of a Megadiverse Mountain Ecosystem in South Ecuador', sub projects B3.1 and Z1.1 (BE 1780/15-1, NA 783/1-1).

References

Bendix J, Rollenbeck R, Reudenbach C (2006) Diurnal patterns of rainfall in a tropical andean valley of southern ecuador as seen by a vertical pointing k-band doppler radar. Int J Climatol 26:829–846

Bendix J, Trachte K, Cermak J, Rollenbeck R, Nauss T (2009) Formation of convective clouds at the foothills of the tropical eastern andes (south ecuador). J Appl Meteor 48:1682–1695

Bischhoff-Gauss I, Gross G (1989) Numerical studies on cold fronts. part i: Gravity flows in a neutral and stratified atmosphere. Meteor Atmos Phys 40:150–158

Bluestein HB, Jain MH (1985) Formation of mesoscale lines of precipitation: Severe squall lines in oklahoma during the spring. J Atmos Sci 42:1711–1732

Bluestein HB, Jain MH (1987) Formation of mesoscale lines of precipitation: Nonsevere squall lines in oklahoma during the spring. Mon Wea Rev 115:2719–2727

Bonner WD (1968) Climatology of the low level jet. Mon Wea Rev 96:833–850

Colby FPJ (1984) Convective inhibition as a predictor of convection during avesesame ii. Mon Wea Rev 112:2239–2252

Cunningham P (2007) Idealized numerical simulations of the interactions between buoyant plumes and density currents. J Atmos Sci 64:2105–2115

De Angelis CF, McGregor GR, Kidd C (2004) A 3 year climatology of rainfall characteristics over tropical and subtropical south america based on tropical rainfall measuring mission precipitation radar data. Int J Climatol 24:385,399

Eliassen A (1959) On the formation of fronts in the atmosphere. In: Bolin B (ed) The atmosphere and the sea in motion., University press, Oxford, pp 227–287

Gandu AW, Geisler JE (1991) A primitive equations model study of the effect of topography on the summer circulation over tropical south america. J Atmos Sci 48:1822 – 1836

Haase SP, Smith RK (1989) The numerical simulation of atmospheric gravity currents. part i: Neutrally-stable environments. Geophys Astrophys Fluid Dyn 46:1–33

Jirak IL, Cotton WR, McAnelly RL (2003) Satellite and radar survey of mesoscale convective system development. Mon Wea Rev 131:2428–2449

Klemp JB, Wilhelmson RB (1978) The simulation of three-dimensional convective storm dynamics. J Atmos Sci 35:1070–1096

Lin YL, Farley RD, Orville HD (1983) Bulk parameterization of the snow filed in a cloud model. J Clim Appl Meteor 22:1065–1092

Liu C, Moncrieff MW (2000) Simulated density currents in idealized stratified environments. Mon Wea Rev 128:1420–1437

Marengo JA, Douglas MW, Dias PLS (2002) The south american low-level jet east of the andes during the 1999 lba-trmm and lba-wet amc campaign. J Geophys Res DOI 10.1029/2001JD001188

McClatchey RA, Fenn RW, Selby JEA, Volz FE, Garing JS (1972) Optical properties of the atmosphere (Third Edition), AFCRL-72-0497. Hanscom Air Force Base, Bedford, Massachusetts, 108 pp

Moncrieff MW, Liu C (1999) Convection initiation by density currents: Role of convergence, shear, and dynamical organization. Mon Wea Rev 127:2455–2464

Moncrieff MW, Miller MJ (1976) The dynamics and simulation of tropical cumulonimbus and squall lines. Quart J Roy Meteor Soc 102:373–394

Pagowski M, Taylor PA (1998) Fronts and the boundary layer - some numerical studies. Bound-Layer Meteor 89:469–506

Rasmussen EN, Blanchard DO (1998) A baseline climatology of sounding-derived supercell and tornado forecast parameters. Wea Forecasting 13:1148–1164

Robee DD, Emanuel JE (2001) The effect of vertical wind shear on radiative-convective equilibrium states. J Atmos Sci 58:1427–1445

Seitter KL (1986) A numerical study of atmospheric density current motion including the effects of. J Atmos Sci 36:619–630

Shapiro A, Hampel T, Rotzoll D, Mosher F (1985) The frontal hydraulic head: A micro-α scale (1km) triggering mechanism for mesosconvective weather systems. Mon Wea Rev 113:1166–1183

Simpson JE (1982) Gravity currents in the laboratory, atmosphere, and ocean. Ann Rev Fluid Mech 14:213–234

Simpson JE, Britter RE (1980) A laboratory model of an atmospheric mesofront. Quart J Roy Meteor Soc 106:485–500

Sun J, Burns SP, Lenschow DH, et al (2002) Intermittent turbulence associated with a density current passage in the stable boundary layer. Bound-Layer Meteor 105:199–219

Thorpe AJ, Miller MJ, Moncrieff MW (1980) Dynamical models of two-dimensional downdraughts. Quart J Roy Meteor Soc 100:463–484

Trachte K, Nauss T, Bendix J (2010) The impact of different terrain configurations on the formation and dynamics of katabatic flows - idealized case studies. Bound-Layer Meteor 134:307–325

Valesco I, Fritsch JM (1987) Mesoscale convective complexes in the americas. J Geophys Res 92:9591 – 9613

Weisman ML, Klemp JB (1982) The dependence of numerically simulated convective storms on vertical wind shear and buoyancy. Mon Wea Rev 110:504–520

Xue M, Martin WJ (2006) A high-resolution modeling study of the 24 may 2002 dryline case ihop. part i: Numerical simulations and general evolution of the dryline and convection. Mon Wea Rev 134:149–171

Xue M, Droegemeier KK, Wong V, Shapiro A, Brewster K (1995) Advanced Regional Prediction System (ARPS) version 4.0 user's guide. Center for Analysis and Prediction of Storms, University of Oklahoma, 380 pp

Xue M, Droegemeier KK, Wong V (2000) The advanced regional prediction system (arps) - a multiscale nonhydrostatic atmospheric simulation and prediction tool. part i: Model dynamics and verification. Meteor Atmos Phys 75:161–193

Xue M, Droegemeier KK, Wong V, Shapiro A, Brewster K, Carr F, Weber D, Liu Y, Wang DH (2001) The advanced regional prediction system (arps) - a multiscale nonhydrostatic atmospheric simulation and prediction tool. part ii: Model physics and applications. Meteor Atmos Phys 76:134–165
/bibliography/jamc

5 Nocturnal Convective Clouds at the Eastern Andes of South Ecuador

This chapter is published in *Journal of Geophysical Research - Atmosphere*, 115, D24203, 2010.
Received: 9 March 2010 / Accepted: 15 October 2010

Nocturnal Convective Cloud Formation under Clear-sky Conditions at the Eastern Andes of South Ecuador

Katja Trachte, Rütger Rollenbeck and Jörg Bendix

Laboratory for Climatology and Remote Sensing (LCRS), Faculty of Geography, Philipps-University Marburg, Marburg, Germany

Abstract The formation of nocturnal convective clouds at the eastern Andes of South Ecuador and the adjacent Peruvian Amazon basin was investigated in a numerical model study. Their formation is expected to be an interactive procedure of nocturnal downslope flows in the Andean terrain, which forms a concave drainage system in the target area. Satellite imagery were used for both the identification of a sample case with a nocturnal cold cloud appearance and for the verification of the simulated results. The cloud patterns were distinguished on the basis of IR temperatures. A comparison of the data demonstrated the occurrence of a cold cloud shield in the target area, although the modeled cluster is significantly smaller. Further analysis of the development of the convective cells confirmed the assumed underlying processes. A strong current in the lower atmosphere, presumably a drainage flow, was recognisable in association with strong moisture convergence using a cross section through the cluster. Their presence was confirmed on the basis of their characteristic features and the surface energy fluxes as the driving force for thermally-induced downslope flows.

Keywords Nocturnal convective clouds, Downslope winds, Eastern Andes

5.1 Introduction

The formation of convective clouds in the tropics over land is dominated by the diurnal cycle of solar radiation with a rainfall maximum in the late afternoon (Mapes et al., 2003; Poveda et al., 2004). In regions such as South Ecuador, which is located in the north-west of South America, the diurnal course of precipitation is modified by the complex terrain of the Andes. The high mountains induce modifications in the atmospheric circulation (e.g. effects of windward and lee side) and regional circulation systems such as mountain-valley breezes. This results in higher spatio-temporal variability in rainfall occurrence (Rickenbach, 2004; Sato et al., 2009).

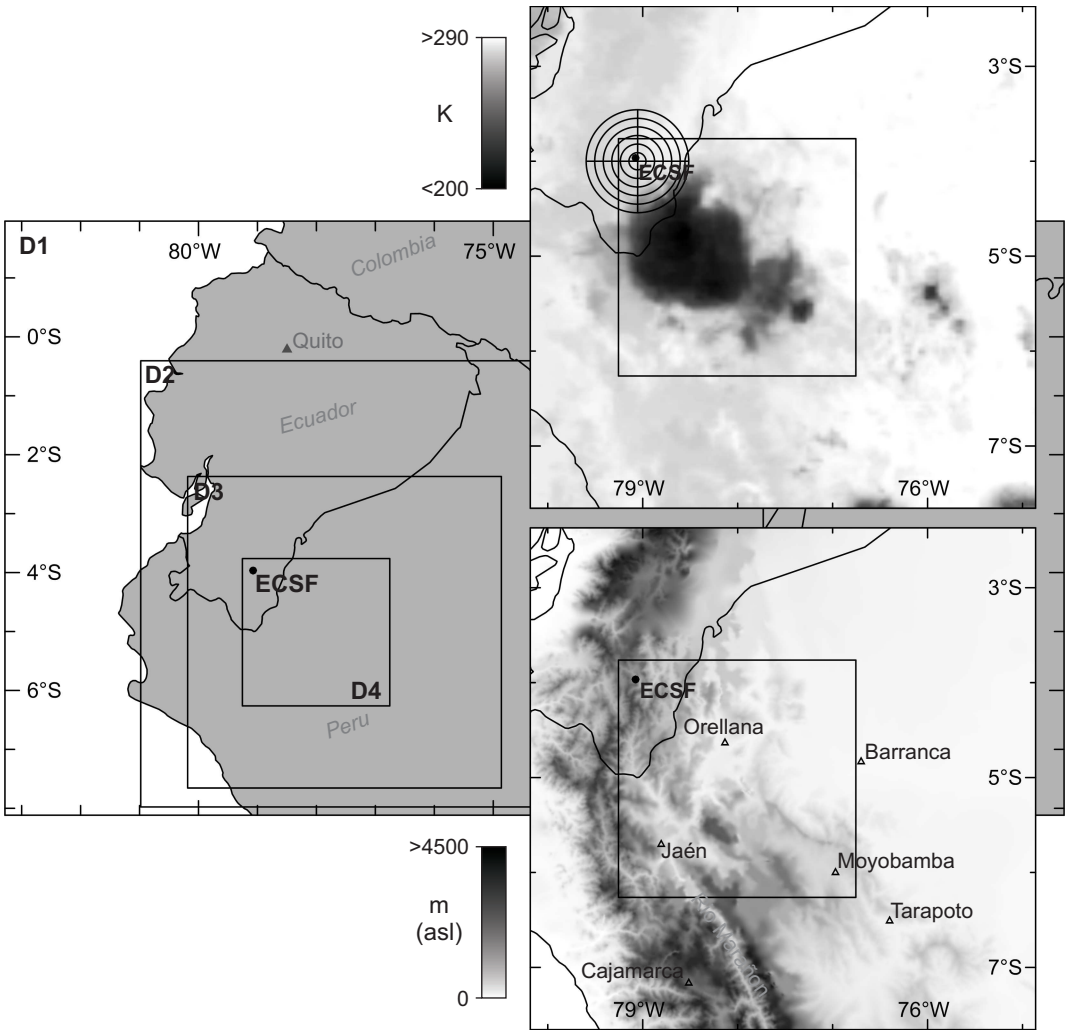

Figure 5.1: South Ecuador and the adjacent Peruvian Amazon basin with the nested domain configuration (left), GOES-E image and location of the LAWR (upper right) and terrain of the study area (lower right)

In our study area, the eastern Andes of South Ecuador (see figure 5.1), precipitation measurements with automatic climate stations and local area weather radar (LAWR) revealed an unexpected early morning rainfall peak at the Estacion Cientifica de San Francisco (ECSF at latitude 3°58'18" S, longitude 79°4'45" W, altitude 1,860 m asl) (Bendix et al., 2006). An analysis of cloud-top temperature distributions from corresponding Geostationary Operational Environmental Satellite (GOES) imagery showed the nocturnal occurrence of mesoscale convective systems (MCS) in the region of the Andean foothills south-east of southern Ecuador in the Peruvian Amazon basin (Bendix et al., 2009), which might be related to the formation of nocturnal rainfall. The generation of the MCS was hypothesised to be a consequence of an interaction between nocturnal drainage air from the Andean slopes and valleys and the warm moist air of the Amazon basin. In doing so, the katabatic flows act like a local cold front, resulting in a destabilisation of the lower atmosphere.

The correlation between nocturnal convective clouds and low tropospheric flow systems has already been demonstrated by other authors. Lopez and Howell (1967) was the first to reference katabatic flows in the tropical Andes and describe the effects of katabatic winds on the eastern slopes, as well as an associated convection initiating hydraulic jump. Garreaud and Wallace (1997) observed that nocturnal rainfall presumably occurs due to enhanced low-level convergence resulting from nocturnal circulation between the Andes and the Amazon region. Angelis et al. (2004) described the convergence of cold air drainage from the Andes and warm, moist air from the Amazon, where the katabatic flows induce low-level instability by acting as a cold front.

Although several phenomenological studies have been conducted on MCS formation and the correlation between convective cloud and cold air drainage flows, evidence for MCS formation in the target area of southern Ecuador and northern Peru induced by nocturnal cold air drainage flow is hitherto lacking. In this context, Trachte et al. (2010) investigated the impact of the terrain on the dynamic behaviour of thermally-induced katabatic flows regarding their confluence due to concave geometry. Her work was based on an idealised case study with a simplified terrain which reduced the main features of the Andes to an extensive drainage system directed into a wide basin. In a second idealised modeling study (Trachte et al. 2010, submitted), the importance of sufficient moisture in the atmosphere for atmospheric instability in such a situation was examined, showing that the formation of a convective cloud cluster is possible due to the topographically induced confluence.

The study at hand encompasses the analysis of the development of such nocturnal convective clouds south-east of southern Ecuador in the Peruvian Amazon basin. Its aim is to describe the nocturnal cell formation in the context of a representative case study observed using satellite data. Previous studies showed that infrared (IR) satellite images are effective in analysing the occurrence of MCSs (Maddox, 1983; Cotton et al., 1989).

Machado et al. (2002) investigated the diurnal cycle of tropical convection using satellite images. Yang and Slingo (2001) also used brightness temperatures to construct a climatology for the diurnal cycle in convection and cloudiness for the tropics. Furthermore, several studies showed that the use of satellite data is beneficial for the validation of numerical models (Chevallier and Kelly, 1997; Morcrette, 1991; Sun and Rikus, 2004; Trigo and Viterbo, 2003). For this reason, the satellite data in this study are used to verify the simulated cloud occurrence by means of calculated brightness temperatures.

The paper is structured as follows: The following section gives an overview of the model setup and the satellite data that was used. The model is validated by comparing observed and modeled brightness temperatures in nocturnal clouds. Information on the reasons for nocturnal cloud formation is provided by an analysis of the area's thermodynamics. In the following section, an analysis of the development of the cloud cluster using a cross-section provides first evidence for the existence of downslope flows as the driving force of convective initiation. In the conclusion, the formation of convective clouds in conjunction with katabatic flows is discussed.

5.2 Data

Geostationary satellites provide atmospheric data with a high temporal and spatial resolution and are especially useful for cloud verifications of numerical model results. This is especially true for regions like the target area in the Ecuadorian / Peruvian Amazon (see figure 1), where no other observational data are available.

In the current study, GOES-East data are used to compare the observed and modeled brightness temperatures. The most important wavelengths are in the infrared (IR) spectrum (GOES-E channel 4 at 10.2 μm - 11.2μm), which is sensitive to clouds. They provide a spatial resolution of 4 km at nadir, which is sufficient to observe cloud features such as MCS. GOES-E originally provides image data with a repetition rate of 30 minutes. The data for this study were downloaded at the Marburg satellite station in the framework of the European Organisation for the Exploitation of Meteorological Satellites (EUMETSAT) Broadcast System for Environmental Data (EUMETCast) distribution system (Bendix et al., 2003). The temporal resolution is 3 h with available time slots for Ecuador at 1900, 2200, 0100, 0400, 0700, 1000, 1300, 1600 LST (LST Ecuador = UTC - 5 h). To complete lacking time slots, additional imagery are taken from the NOAA's Comprehensive Large Array-data Stewardship System (CLASS). For the presented case study, we used night images from 12 October to 13 October 2009 (sunset at 1900 LST and sunrise at 0700 LST) in the target area), because the imagery reveals a remarkable example of an MCS in the target area, which is representative for the case study.

5.3 Model Set-up

In the current study the Advanced Regional Prediction System (ARPS) from the Center for Analysis and Prediction of Storms (CAPS) at the University of Oklahoma is used. ARPS is a fully-compressible, non-hydrostatic numerical model with a generalised terrain-following coordinate system and vertical stretched grid. For more details, see Xue et al. (1995, 2000, 2001).

For our study we used multiple one-way nested grids with an increment of 36 km with 57 x 33 points, 12 km with 99 x 72 points, 4 km with 150 x 150 points and finally 1 km with 300 x 300 grid points (see figure 5.1 and table 5.1). The first domain (D1 in figure 5.1) covers Ecuador, southern Colombia, northern Peru and the western part of Brazil. Domain 2 (D2) and 3 (D3) cover South Ecuador and the adjacent Peruvian Amazon. The smallest domain (D4) was focused on the cloud formation area identified from the satellite data. The vertical grid of both, domain D3 and D4 has 55 layers with an average spacing of 350 m. Near the ground the grid is stretched with a hyperbolic function to a minimum of 20 m vertical resolution for the lowest 500 m to capture the development of thermally-induced downslopes in the planetary boundary layer (PBL). The 2.5° x 2.5° resolved NCAR/NCEP DOE Reanalysis II data (Kanamitsu et al., 2002) were used to initialised the outer domain. The terrain of each domain is represented by the USGS GTOPO30 data, which have a horizontal resolution of approximately 1 km. For the inner domain (D4) a 9-point smoother was applied 10 times to reduce outliers occurring in the terrain data, e.g. point to point height difference of 1000 meters.

Table 5.1: Grid configurations

Domain	dx, dy	dz_{avg}	dz_{min}	large time step	small time step	terrain
D1	36 km	600 m	300 m	12 s	3 s	30”
D2	12 km	500 m	150 m	6 s	3 s	30”
D3	4 km	350 m	20 m	1 s	0.5 s	30”
D4	1 km	350 m	20 m	1 s	0.5 s	30”

ARPS was applied with the Deardorff closure scheme physics package for turbulence parametrisation and the implementation of 1.5-order turbulent kinetic energy *(TKE)* (Deardorff, 1972). The surface fluxes are responsible for the mass and heat exchange with the atmosphere. In ARPS they are computed by a stability and roughness-length dependent surface-flux model (Businger et al., 1971; Byun, 1990). The fluxes are solved on the basis of the similarity theory by Monin and Obukhov. In the present simulations, the surface fluxes are calculated with stability-dependent

drag coefficients and the bulk Richardson number as the stability parameter. For more details, see Xue et al. (1995, 2001).

A force-restore two-layer soil and vegetation model was used to provide soil-model general surface characteristics (Noilhan and Planton, 1989). The input data for the soil type and the vegetation are derived from the USGS global input data with a horizontal resolution of approximately 1 km. Radiative processes are considered by the Goddard shortwave and longwave atmospheric radiation transfer parametrisation (Chou, 1990, 1992; Chou and Suarez, 1994).

The convective parametrisation is disabled in both, domain D3 and the inner domain D4 due to the high horizontal resolution sufficient to initiate deep convection (Xue and Martin, 2006), so that convection is calculated directly as a response to the dynamics. An explicit microphysical parametrisation scheme was used for the simulation of the cloud properties, which solves six prognostic equations for water vapour, cloud water, rain water, cloud snow, cloud ice and grauple (Lin et al., 1983).

The brightness temperatures of the model are derived using the Community Radiative Transfer Model (CRTM) (Chen et al., 2008) using the same look-up tables as for GOES Variable format (GVAR) (Weinreb et al., 1997). The implementation of this retrieval is adapted from the Weather Research and Forecasting Post Processor software.

5.4 Results

The multiple nested domain setup presented above was used to examine the development of nocturnal convective clouds in the eastern Andes of South Ecuador. The simulated results are compared to observational data on the basis of brightness temperature distributions. Further analyses of the atmospheric conditions show the impact of the horizontal and vertical resolution on the described nocturnal cloud formation mechanism. The development of convective clouds and the presence of a strong low-level flow as the driving force is illustrated with a cross section through the cloud formation area. Their specific features will be discussed in the context of the energy fluxes in order to demonstrate the occurrence of a downslope flow.

5.4.1 Convective Cloud Patterns

We begin with an evaluation of the mesoscale convective cloud appearance in the target area. Generally, MCS are defined as an ensemble of convective elements with a time scale of at least 3 hours Houze (1995). They differ from an individual cumulonimbus by their duration and spatial extension. A typical feature of MCS are their upper cirriform cloud shield combining several convective cells into an organised cloud system. They consist of both convective regions with intense vertical velocities and stratiform regions with a more uniform texture, which leads to more complex dynamics (Houze, 2004). MCS are divided into different classes, such as

the mesoscale convective complexes (MCC), by IR temperature (Bluestein and Jain, 1985, 1987; Jirak et al., 2003). MCCs are quasi-circular, long-lasting systems with an IR blackbody temperature T_{BB} <-52 °C over an area of 50,000 km^2 (Maddox, 1980). More definitions and thresholds are summarised in table 5.2 as defined by (Maddox, 1980), which are used to identify the nocturnal cloud cluster in the target area.

Table 5.2: Mesoscale convective complex definitions (as defined by Maddox (1980))

	Physical characteristics
Size	cloud shield with continuously low IR temperatures $\leq$ 220 K must have an area $\geq$ 50,000 km^2
Shape	eccentricity (minor axis/major axis) $\geq$ 0.7 at time of maximum extent
Duration	size definition must be met for a period $\geq$ 6 hours
Initiate	size definition is first satisfied
Terminate	Size definition is no longer satisfied

Figure 5.2 and 5.3 display GOES-E (10.2 - 11.2 μm) IR brightness temperature images and modeled data from 12 October 2009 to 13 October 2009 at different time intervals beginning at 2015 LST. The images show the nocturnal evolution of an MCS south-east of southern Ecuador. The occurrence of a convective cluster can be confirmed with cold cloud temperatures. The satellite data in the target area (figure 5.2 a, d, g) shows that low IR temperatures can be used as an indicator for the development of convective cells. They start in the early nighttime (2015 LST) and grow throughout the night (2215 LST) to a size of 5,000 km^2. Several close cells can be seen to possess minimum brightness temperatures of 220 K denoted by the white contour of 220 K. During the night, the cells merge to an organised quasi-circular system (0115 - 0315 LST, see figure 5.3), reaching brightness temperatures of 220 K over an area of 10,000 km^2, which characterises a cirriform cold cloud shield. Inside this shield further areas can be differentiated, revealing considerably colder temperatures below 220 K. These cold cores represent higher atmospheric regions, indicating intense convective regions with overshooting tops. At 0215 LST the interior of the cloud system reaches its maximum size, with a horizontal extension of 12,000 km^2. The clear-sky environment surrounding environment the clusters, which are sustained over the whole night, and the stationary appearance of the cold cloud are particularly noteworthy.

A comparison of the thresholds in table 5.2 shows that not all of the physical definitions for a MCC are fulfilled. Despite the low IR temperatures, the cold cloud shields extend over an area of 12,000 km^2, which is too small for an MCC.

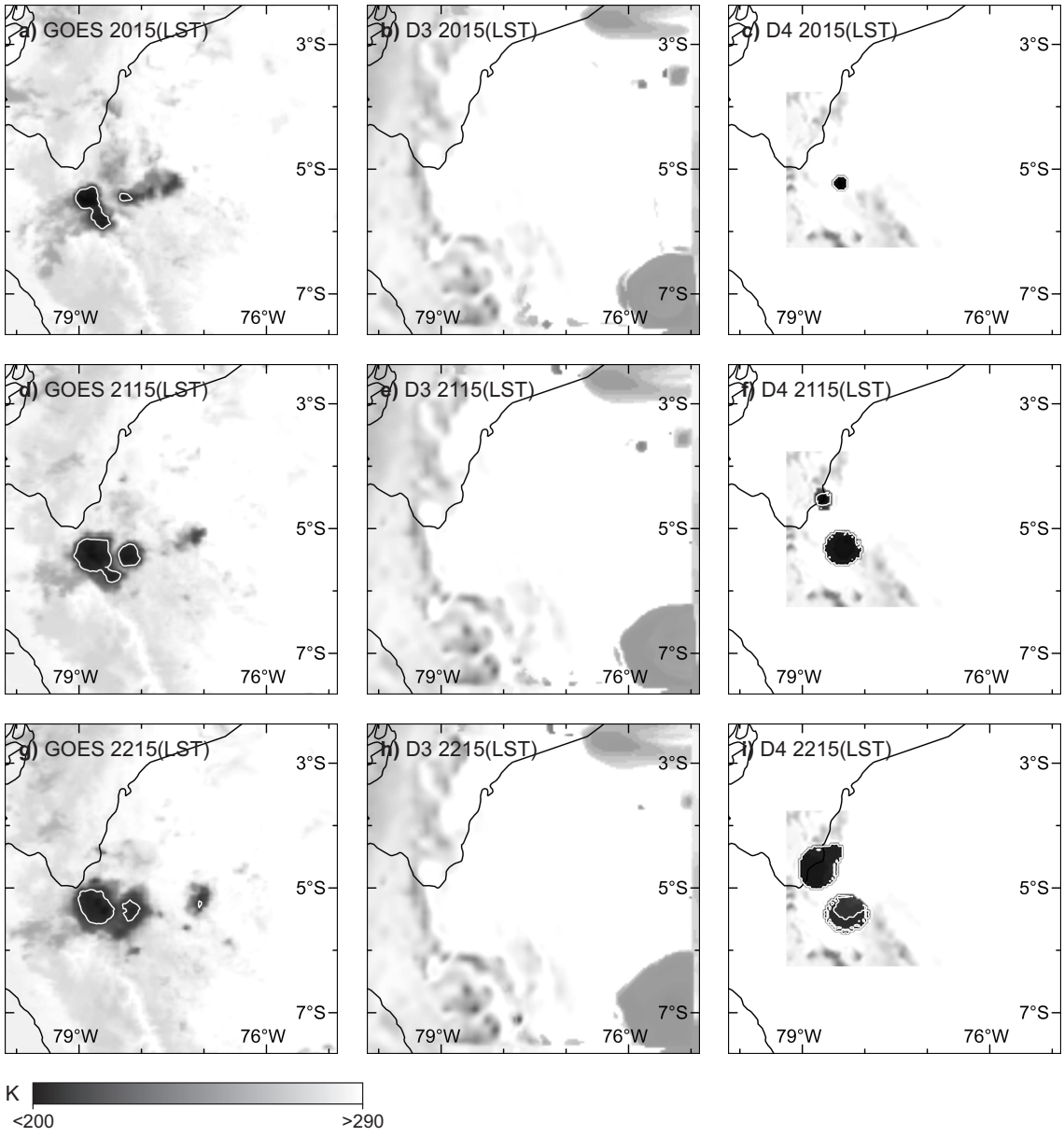

Figure 5.2: GOES-E brightness temperatures (10.2 - 11.2 μm, K) (a, d, g), ARPS brightness temperatures (K) (domain D3 b, e, h) ARPS brightness temperatures (K) (domain D4 c, f, i) with a white contour (220 K) for 2015 LST, 2115 LST and 2215 LST

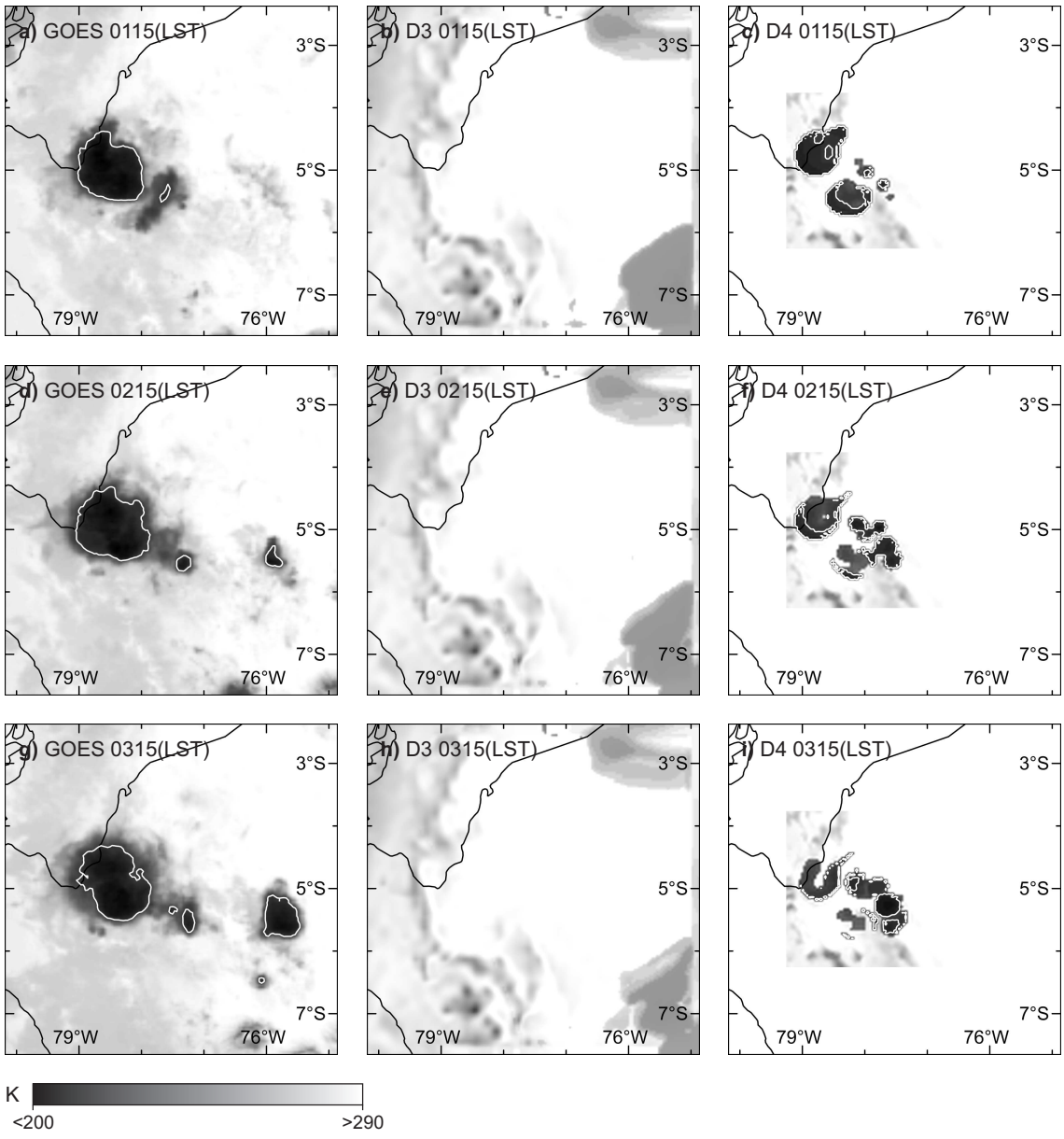

Figure 5.3: GOES-E brightness temperatures (10.2 - 11.2 μm, K) (a, d, g), ARPS brightness temperatures (K) (domain D3 b, e, h) ARPS brightness temperatures (K) (domain D4 c, f, i) with a white contour (220 K) for 0115 LST, 0215 LST and 0315 LST

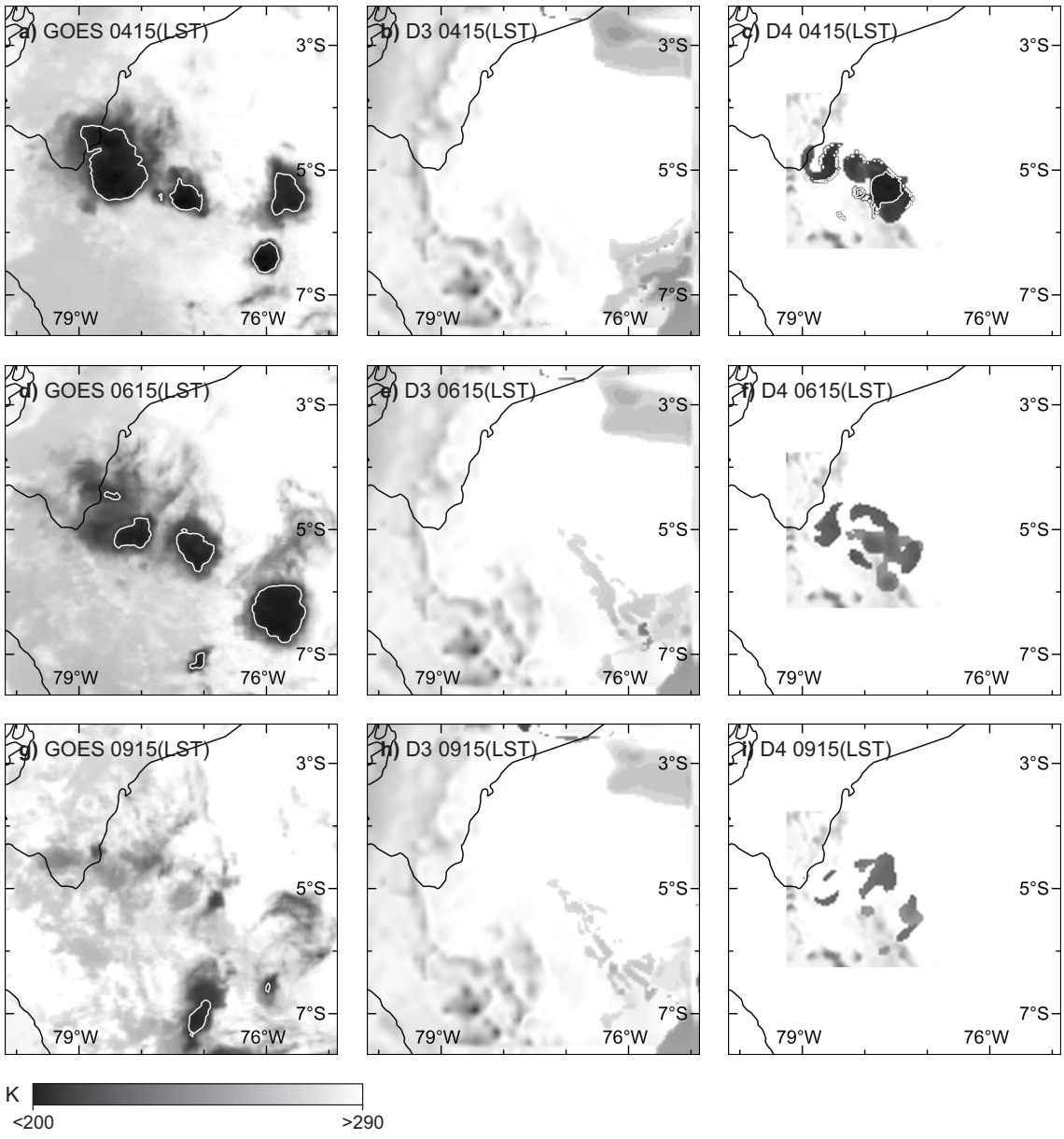

Figure 5.4: GOES-E brightness temperatures (10.2 - 11.2 μm, K) (a, d, g), ARPS brightness temperatures (K) (domain D3 b, e, h) ARPS brightness temperatures (K) (domain D4 c, f, i) with a white contour (220 K) for 0415 LST, 0615 LST and 0915 LST

Additionally, the duration of this shield is less than 6 hours and thus fails to fulfill the definition of an MCC. Therefore, the pattern is an MCS consisting of an ensemble of convective elements (see (Houze, 1995), but not a more severe MCC, as defined by Maddox (1980). At 0415 LST the cluster begins to weaken (see figure 5.4), which is observable by the increasing brightness temperatures (0615 LST). By now the values are around 230 K. The break up of the cloud is related to extensive rainfalls and the lack of sufficient strengthening through latent heat. By the morning hours around 0915 LST, the cloud system has completely disintegrated.

5.4.2 Comparison of Observed and Simulated Cloud Patterns

The spatio-temporal development of the identified convective cloud cluster depicted in figures 5.2, 5.3 and 5.4 is used to validate the simulation results by comparing satellite-observed data and model derived brightness temperatures. Only domain D3 and D4 are displayed, since domain D1 and D2 show no additional information and are not relevant for the current considerations (see figure 5.1).

For the time steps between 2015 LST and 0915 LST, figures 5.2, 5.3 and 5.4 b, e, h show that the simulated data show no distinguishable convective cells in the target area, as visible in the satellite data. ARPS produces neither deep convection nor cloudiness during the night in the region of investigation, except at the eastern side of the domain where warmer clouds (250 K) occur. Analyses regarding the reasons for this lack are discussed in the following sections.

In contrast, an inspection of the inner domain (D4) with a resolution of 1 km (figure 5.2, 5.3 and 5.4 c, f, i) confirms the formation of a growing cold cloud pattern south-east of Ecuador featured by the contour of 220 K. A convective cell develops in the target area at the beginning of the night, which is characterised by low brightness temperatures (5.2 c). Although this cell is smaller (800 - 1000 km^2) than displayed in the satellite data and the GOES-E data show the generation of more than one cell, they show comparable temperatures (220 K). At 2115 LST a quasi-circular system is created reaching a spatial size of 6500 km^2, but still remains less than the observed formation. North-westerly a second cold cloud evolves with brightness temperatures of 220 K and a size of 800 - 1000 km^2 creating an enlarged cluster of 8000 km^2 until 2215 LST. In the ongoing simulation, the two convective clouds are maintained until 0115 LST with colder areas in the cloud shield, corresponding with the patterns visible in the GOES-E data. They are colder than 220 K indicating convective overshooting tops. While in the satellite-observed data the cells merge to one enlarged system reaching a size of maximum 12,000 km^2, the simulated data show two separated and smaller cold clouds, respectively. The dissipation of the southerly cluster has already started by 0115 LST as indicated by the warmer IR temperatures, which characterise stratiform areas. Notable is that the simulated cold clouds are within an equal area visible in the satellite-observed data and that they have a comparable orientation.

At 0115 LST new convective cells evolve to the north-east with values of 220 K. While these cells grow until 0415 LST to an ensemble of convective elements more comparable to the GOES-E data, the two circular systems of time period 2115 LST to 0115 LST have disintegrated. The dissipation of the observed as well as simulated nocturnal convective cluster takes place in the early morning hours (0615 LST - 0915 LST). Although the size of the simulated cluster lies below the observed pattern the development of a nocturnal convective cloud cluster occurs with similar brightness temperatures.

5.4.3 Analyses of Atmospheric Conditions

In order to take a closer look at the reasons for initiation and absence of nocturnal convection, analyses of the development of the surface front and the thermodynamic structure of the atmosphere are presented. The interaction between the cold drainage of air from the Andean mountains with the warm-moist air of the Amazon, both for domains D3 and D4 (see figure 5.5), is investigated in the first instance. The thermodynamics are examined based on the vertical structure of the atmosphere (see figure 5.6 and 5.7). The influence of the terrain is displayed in figure 5.8.

Surface Cold Front

The development and location of the surface cold front is shown by the horizontal distribution of the equivalent-potential temperature θ_e, which is defined as:

$$\theta_e = \theta exp\left(\frac{Le}{c_p T_{LCL}} w_v\right) \tag{5.1}$$

with θ as the potential temperature, Le as the latent heat of evaporation, c_p is the specific heat content, T_{LCL} is the temperature at the lifting condensation level (LCL) and w_v as the mixing ratio for water vapour. θ_e represents a value which is composed of the temperature and the dew point. The greater the dew point, the higher an air parcel is able to rise due to the release of latent heat. Thus, θ_e is an indicator for the energy content of the air. Its values are quasi-constant within an air mass.

Figure 5.5a illustrates θ_e for the 4 km domain (D3) at 1900 LST for the lower troposphere. The differences between the cold Andean regions, with average values of 324 K, and the warm-moist Amazonian basin, with average values of 348 K, are clearly visible. The katabatic winds from the mountains drain cold air into the basin, generating a horizontal gradient, which is evident by the rapid increase in the equivalent-potential temperature field. This gradient is especially noticeable in the cloud formation region south-east of South Ecuador. The values rise by 14 K in a distance of approximately less than 40 km, indicating a boundary of air masses and, thus, the formation of the cold front.

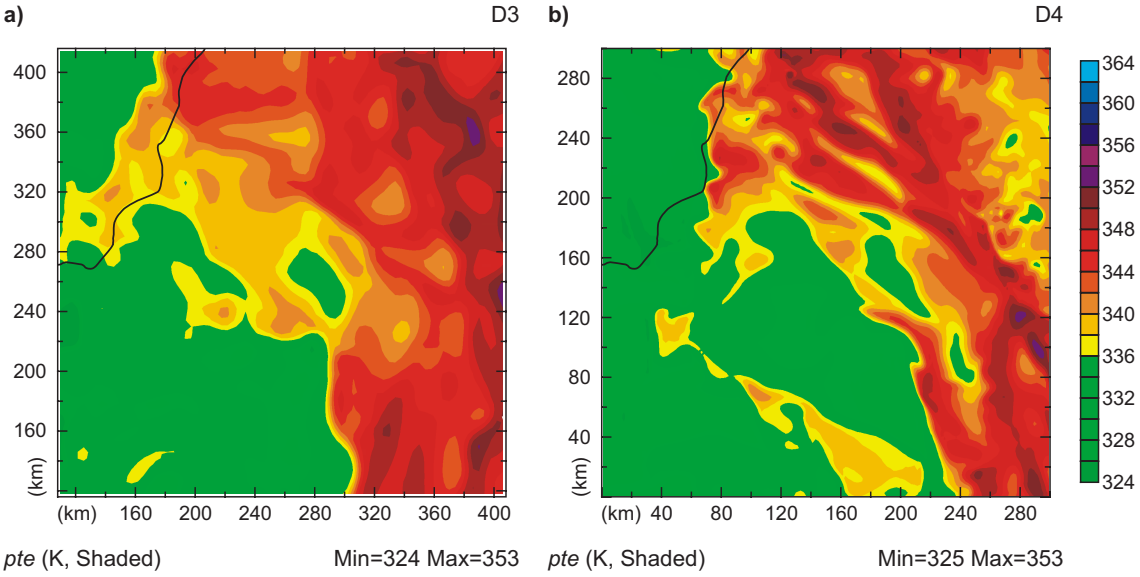

Figure 5.5: Horizontal cross-section (xy-plot at z = 300 m asl) of the equivalent-potential temperature θ_e (*pte*, shaded, K) of a) subset of domain D3 equal to domain D4 and b) domain D4 for 1900 LST

A comparison to the equivalent-potential temperature in the 1 km domain (D4), as displayed in figure 5.5b, shows that there are no great differences in its horizontal distribution. On average, the lower θ_e values of 325 K dominate in the western part of the domain, and in the eastern part, the high values of the Amazon dominate, with an average of 344 K. Here a clearly marked zone of rapidly increasing values developed in the cloud formation area due to the cold drainage of air from the Andean mountains. A horizontal gradient of 14 K also occurs in D3 at a distance of approximately 40 km. However, the impact of the higher horizontal resolution on the individual processes and elements is visible in D4. Along the slopes of the Andes, the cold air propagates further into the Amazon basin. This is caused by stronger generated katabatic flows as a result of more accurately featured terrain: the GTOPO30 terrain data in domain D4 are despite their smoothing better defined affecting the occurrence of the downslope winds.

Atmospheric Stability

A cross section through the front of both domains (D3 and D4) in the region of cloud formation gives further information about the reasons for the initiation and the lack of deep convection, respectively. Therefore, the θ_e is used as well, since it demonstrates the potential instability of the atmosphere. A decrease of θ_e with height signifies a decrease in the absolute humidity.

Figure 5.6a shows the vertical distribution of D3 at 2015 LST. A layer of warm-moist air in the lower troposphere is located to the east of the Andes in the Amazon

basin, which reaches a thickness of approximately 2.5 km. It is characterised by equivalent-potential temperatures with average values of 346 K. Areas with high values of 354 K are arranged in this layer. They are often burst points for strong convective developments. Machado et al. (2002) confirm that θ_e values > 356 K are mainly associated with an unstable boundary layer.

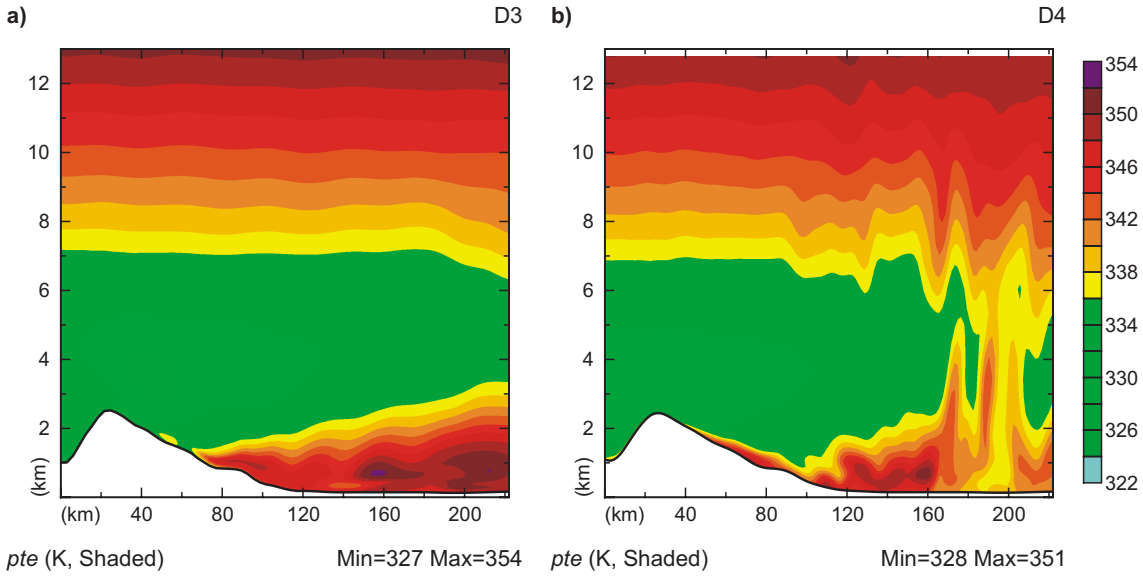

Figure 5.6: Vertical cross-section (xz-plot at x = 38 km and y = 35 km, x = 170 km and y = 215 km) of the equivalent-potential temperature θ_e (*pte*, shaded, K) of a) domain D3 and b) domain D4 for 2015 LST

Above this warm-moist air is a layer of colder and thus, drier air. This layer is located between 2.5 km and 6 km and reaches minimum values of 328 K. That is, the equivalent-potential temperature decreases with height to a level of 6 km. The result is a potentially unstable atmosphere, which can become conditionally unstable if the air is lifted and additionally becomes saturated. In this process the mentioned burst points play an important role in the initiation of deep convection, since they can provide the essential energy. Above this layer the equivalent-potential temperature rises again.

The vertical distribution of the equivalent-potential temperature in the 1 km simulation at the same location and time step (2015 LST) is demonstrated in figure 5.6b. In the lower troposphere, warm-moist air from the Amazon is visible as well. The θ_e values reach a maximum 350 K and a thickness of approximately 2.5 km. A comparably colder layer is located above this air, as displayed in figure 5.6a. However, in the current simulation, this cold layer is interrupted by several columns with high values (344 K). They characterise a vertical transport of warm-moist air which has reached saturation and becomes more unstable due to the release of latent

heat. Hence, this displacement of air masses indicates convective activities, which are already suggested by the brightness temperature patterns in figures 5.3 and 5.4.

Apart from the θ_e horizontal and vertical distribution further parameters are used to study the atmospheric conditions and to evaluate whether convective activities are induced (see table 5.3). The basic parameters for these analyses are the convective available potential energy (*CAPE*) (Moncrieff and Miller, 1976) and the convective inhibition (*CIN*) (Colby, 1984).

The *CAPE* is the vertically integrated positive buoyancy of a parcel between the height of the level of free convection (*LCF*) (z_{LFC}) and the height of the equilibrium level (z_{EL}). It represents the maximum energy available to an ascending air parcel and is an indicator for the potential of convective initiation:

$$CAPE = \int_{z_{LFC}}^{z_{EL}} g \left(\frac{\Theta_{par} - \Theta_{env}}{\Theta_{env}} \right) dz \tag{5.2}$$

with Θ_{par} as the potential temperature of the parcel lifted from the surface (z_{sfc}) up to the *LFC* (z_{LFC}) and Θ_{env} the ambient potential temperature. In contrast, the *CIN* represents the energy required to lift a negatively buoyant parcel from the surface to the *LFC* and is defined as:

$$CIN = - \int_{z_{sfc}}^{z_{LFC}} g \left(\frac{\Theta_{par} - \Theta_{env}}{\Theta_{env}} \right) dz \tag{5.3}$$

Figure 5.7 shows two atmospheric profiles by night (see figure 5.7a and b). The amount of *CAPE* for domain D3 is 872 J·kg^{-1}, which represents only a marginally unstable atmosphere and mean potential for deep convection. In the same time, the *CIN* reaches values of -168 J·kg^{-1}, which is a great amount of negative buoyancy and has to be overcome to initiate convection. On the other hand, the Lifted Index (*LI*) of -3.1 indicates a moderately unstable atmosphere. This is also true for the *K-Index* of 31, which characterises a potential for the development of a thunderstorm.

The atmospheric profile for D4 seems not to differ much from domain D3: the environmental temperature profile and the temperature of an ascending air parcel are almost identical. Due to the same vertical resolution they both develop a surface inversion. The amount of *CAPE* (964 J·kg^{-1}) is slightly greater and the convective inhibition of -146 J·kg^{-1} is slightly smaller. Both profiles represent marginal atmospheric instability and require an explicit trigger to reduce the negative buoyancy and initiate deep convection. However, the *K-Index*, which with its value of 38 is greater than in D3, indicates a very good potential for the formation of a thunderstorm, as already illustrated in figures 5.2, 5.3 and 5.6b. Additionally, a closer look offers some important details: the lifting condensation level (*LCL*) and the level of free convection (*LFC*) are significant lower than in the 4 km simulation. While in D3 the *LCL* is at the 869 hPa level, the *LCL* in D4 reaches 897 hPa. This is also observable in the *LFC*, which is reached in D3 at the 683 hPa level and in D4 at a height of 770 hPa. With a significant trigger function, presumably the downslope

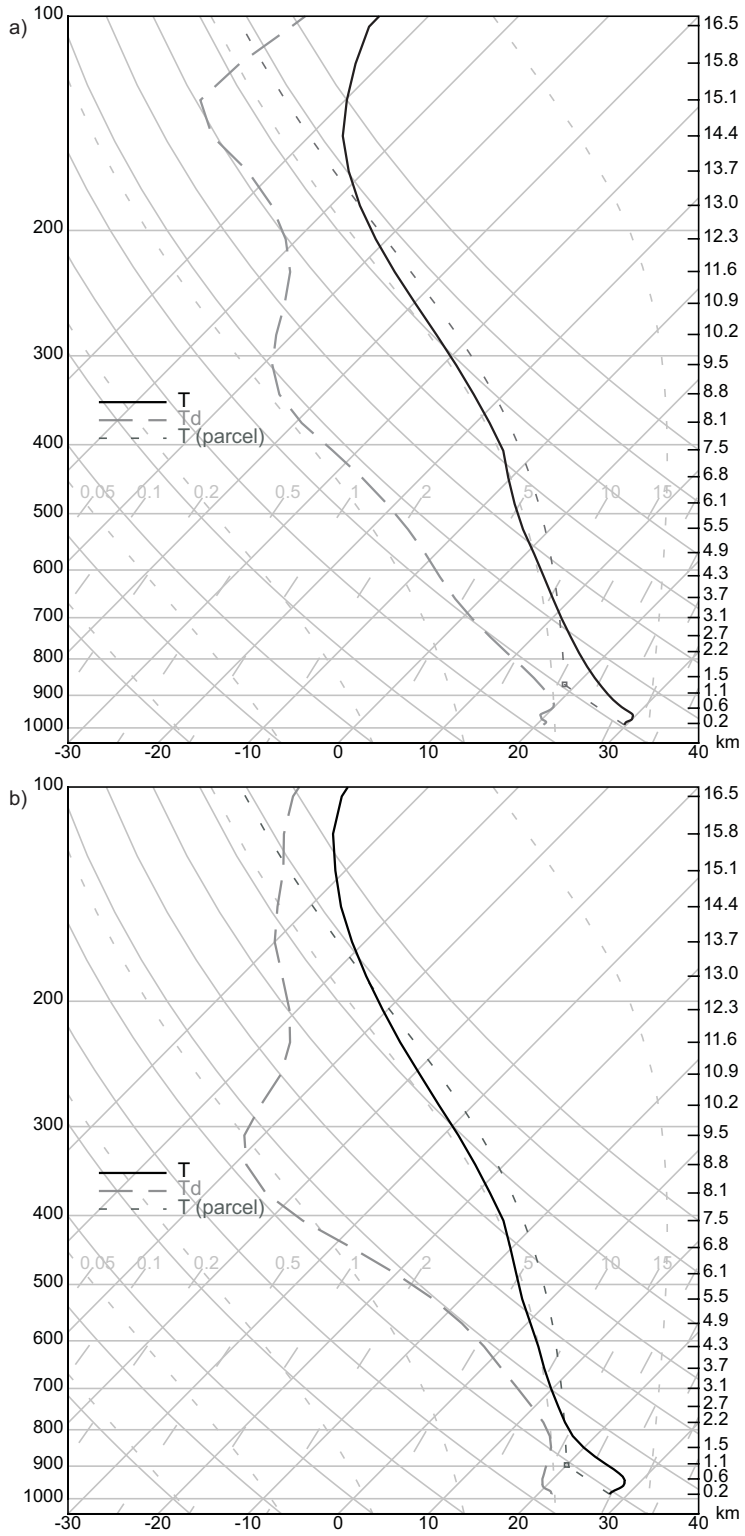

Figure 5.7: SkewT log P profiles a) domain D3 and b) domain D4 taken at -78.0° x -4.9° for 1900 LST

winds from the Andean mountains, the warm-moist air masses of the Amazon at the foothills seen in figure 5.6b are able to reach the *LCL* and, finally, the *LFC*.

Table 5.3: Environmental parameters

	Domain D3	Domain D4
CAPE	872 J·kg^{-1}	964 J·kg^{-1}
CIN	-168 J·kg^{-1}	-146 J·kg^{-1}
LI	-3.1	-3.3
K-Index	31	38
LCL	869 hPa	897 hPa
LFC	683 hPa	770 hPa

The analyses of the D3 and D4 simulation demonstrate that both domains offer a potential instability and thus the probability to initiate deep convection and the formation of a thunderstorm. The results also show that a strong trigger is required to lift the air.

Horizontal Convergences

It is assumed that the nocturnal convective activities in the target area are triggered by strong convergences of katabatic flows from the Andean mountains, which are developed by the shape of the terrain. The flows can be described as horizontal divergence, where negative values describe the convergences and positive values the divergent patterns.

The results of domain D3 and D4 at 1900 LST are demonstrated in figure 5.8. It shows the horizontal divergence patterns with an amplification factor of 1000 in the cloud formation area. Especially noteworthy is the consistent distribution of the convergence patterns in domain D3 with rather small areas of greater values (figure 5.8a), which reach maximum values of 2.5 10^{-3} s^{-1}. The convergence zones are organised along the slopes, reflecting the more coarsely rendered terrain due to the 4 km resolved grid size. These patterns also describe the regime of katabatic flows and their convergences at the foothills.

The more highly resolved D4 simulation shows greater variability in the horizontal divergence distribution when compared with the D3 simulation (figure 5.8b). The convergence patterns are organised in the same areas, but this time more structured and strongly developed. Distinct convergences occur along the slopes with maximum values of 6.5 10^{-3} s^{-1}, which is more than twice as strong as in domain D3. This is caused by terrain effects (see figure 5.1 lower right part), which are defined better in domain D4, despite the 9-point smoothing, due to the 1 km spatial resolution, which affects the katabatic flows.

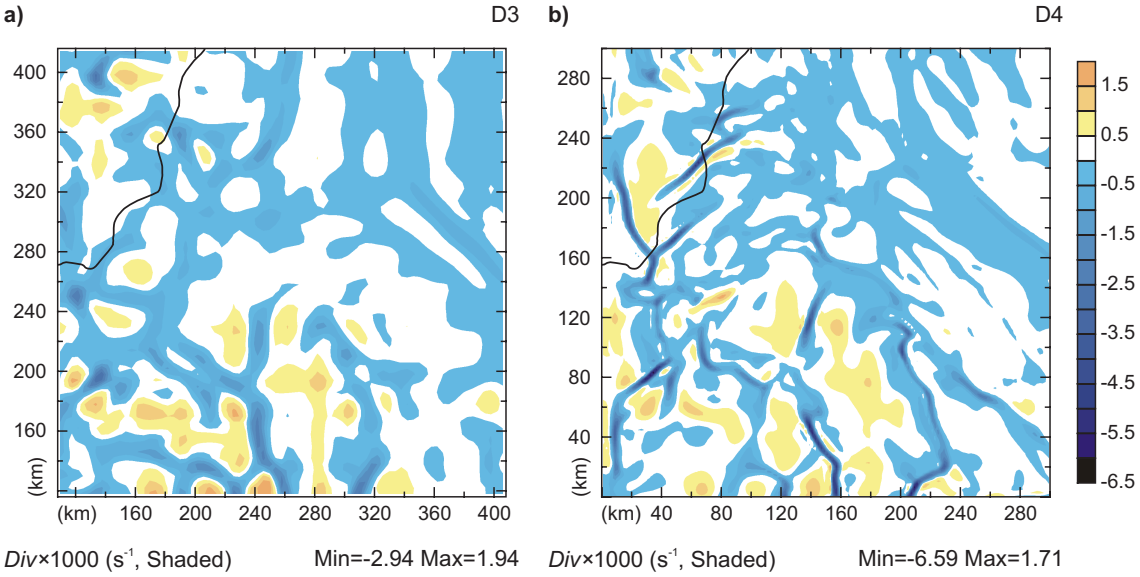

Figure 5.8: Horizontal cross-section (xy-plot at z = 300 m asl) of the divergence field (*DIV*, shaded, s^{-1} amplified by a factor of 1000) for a) subset of domain D3 equal to domain D4 and b) domain D4 for 1900 LST

They propagate down the steeper slopes and converge at the foothills with an higher mass contribution in these areas. As demonstrated in the idealised case study (Trachte et al., 2010) the shape of the terrain strongly influences the pressure increase and convergences caused by the downslope winds. Those convergence zones are closely linked to vertical velocities because they are a consequence of the horizontal convergences, and thus, an increase of mass. The patterns herein are located in the region, where the cold clouds appear in the observational data and in the D4 simulation results, but not in the coarser D3 data. The horizontal convergence demonstrates the influence of the terrain on horizontal dynamics and, subsequently, vertical characteristics. The mass contribution in D3 is not as strong due to the reduced terrain information resulting in a low increase of pressure. Considering the higher *LFC* of D3, those convergences are too weak to sufficiently lift the air and initiate deep convection. For domain D4, the convergences are stronger and the *LFC* lower.

In the next section the development of the cloud cluster is examined and discussed in conjunction with katabatic flows.

5.4.4 Convective Cloud Development

A cross section through the cluster in domain D4 is used to further examine the formation of the displayed cloud.

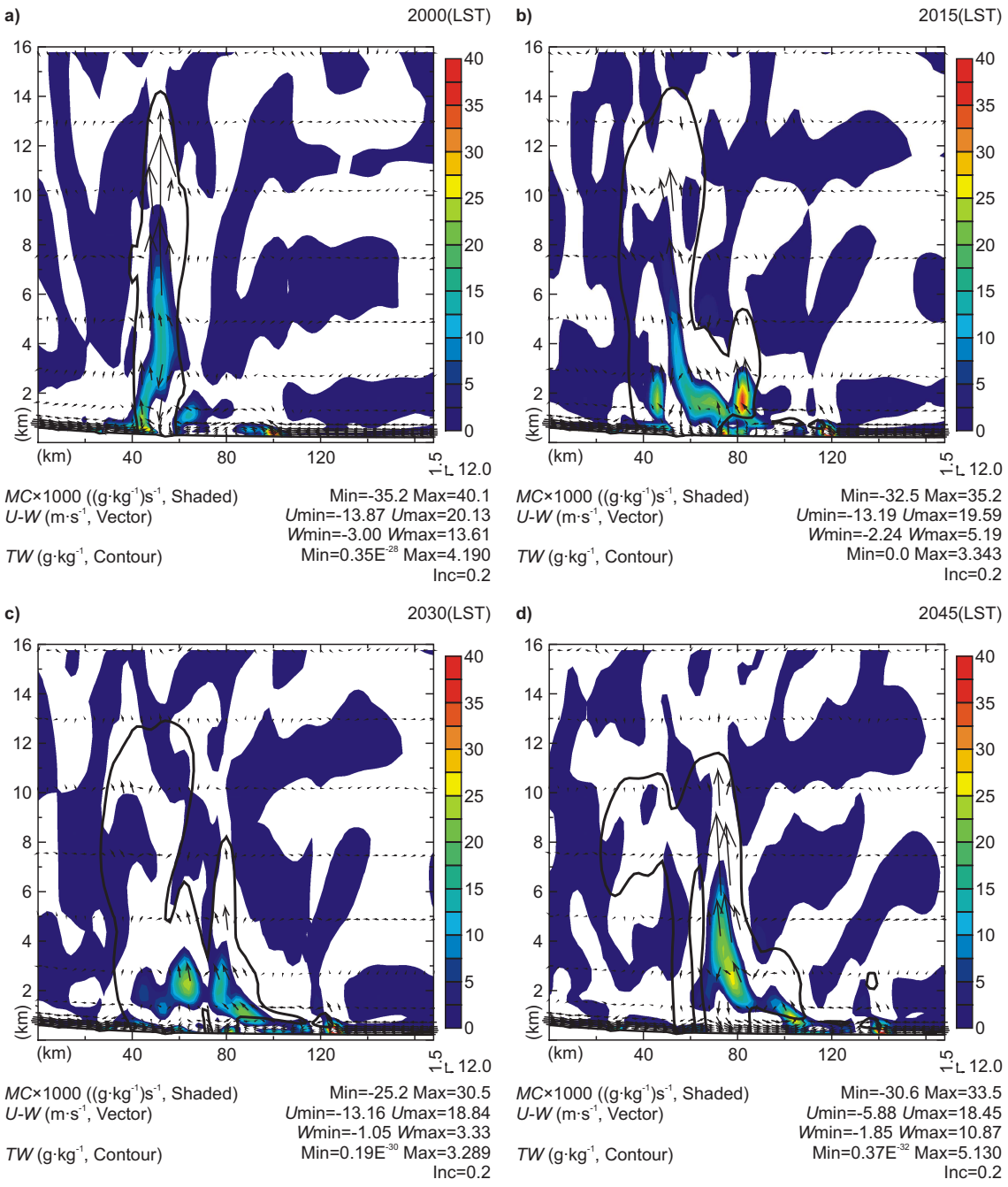

Figure 5.9: Vertical cross-section of domain D4 (xz-plot from x = 71 km, y = 80 km and x = 170 km, y = 215 km) of horizontal moisture convergence amplified by a factor of 1000 (*MC*, shaded, $(g \cdot kg^{-1}) \cdot s^{-1}$), the wind field in *u*-*w* direction (vectors, $m \cdot s^{-1}$) and the total condensed water (*TW*, solid line), $g \cdot kg^{-1}$ at a) 2000 LST, b) 2015 LST, c) 2030 LST and d) 2045 LST

Figure 5.9 shows the horizontal moisture convergence (shaded), the wind field in u-w direction (vectors) and the total condensed water (solid line) at four time steps in a 15 minute interval. In figure 5.9 the development of a convective tower in its cumulus stage, which can be identified by means of the buoyant plume, is illustrated. It is characterised by a region of increasing wind velocities (w vectors increase with height), which reached maximum values of 13.6 $\mathrm{m{\cdot}s^{-1}}$ and a height of 14 km. Those accelerations occur when the *LFC* is reached. Strong low-level moisture convergence with maximum values of 40 $(\mathrm{g{\cdot}kg^{-1}}){\cdot}\mathrm{s^{-1}}$ forces the air parcels to ascend. Within the boundary layer a deep cloud is generated over the maximum of the low level moisture convergence (visible by the solid line of total condensed water) due to the release of latent heat. In the lower troposphere entrainment occurs as a result of the upward mass flux. Accordingly divergence branches in the upper troposphere as well as detrainment evolve at the lateral sides. The cloud remains in this region and grows deeper forced by an enhanced moisture convergence (figure 5.9 b). Cell regeneration takes place in this region, as indicated by the creation of a group of cells. They form as well over the maximum moisture convergence with values of 35 $(\mathrm{g{\cdot}kg^{-1}}){\cdot}\mathrm{s^{-1}}$ causing an acceleration of vertical velocities (5 $\mathrm{m{\cdot}s^{-1}}$). With increasing time (figure 5.9 c) the convective cells merge to a multicell cluster in its mature stage. Dissipation begins at the rear, which is associated with local upward and downward motion causing extensive precipitation patterns. But at the frontside the new cells grow deeper. After a further 15 minutes the rearward cell has dissipated but is survived by upper level cirrus it generated. The convective cell at the leading edge in contrast has strengthend characterised by the increasing wind vectors with height. It shows similar features as the tower in figure 5.9a. Additionally, downbursts of cold air in the lower levels occur initiating the formation of a new cell in the region of strong moisture convergence with maximum values of 27 $(\mathrm{g{\cdot}kg^{-1}}){\cdot}\mathrm{s^{-1}}$. Those structures shown herein of dissipating and growing convective cells can also be observed in the satellite-observed cloud properties in figure 5.2 and are typical for convective cloud clusters (Houze, 2004).

During the developmental stages of the cluster, a strong current in the lower levels of the atmosphere is recognisable, as can be identified by the vectors. This nocturnal flow, presumably the katabatic flow, advances cold air into the convective area. The interaction of the warm-moist air of the Amazon, which occurs in the region of the displayed frontal zone in figure 5.5b, supports the ascension of air parcels and, thus, the formation and maintenance of the multicell cloud cluster.

5.4.5 Katabatic Flows

Katabatic flows and their interaction with the specific terrain configuration in the target area are assumed to be the driving mechanism behind the nocturnal cloud formation. The flows develop in hilly regions on calm, clear nights through radiative surface cooling. A buoyancy deficit is generated as a result of a radiation

divergence associated with the ground heat fluxes, which result from mechanically induced turbulent-kinetic energy (TKE) and latent (LE) and sensible (H) heat fluxes (Prandtl, 1942; Defant, 1949). The soil temperature reduces to a value below the adjacent air temperature followed by the sensible heat flux (H) from the atmospheric boundary layer to the earth surface balancing the heat loss. The surface acts as a sink for the thermal energy. The result is a cooling of the lower atmosphere and a development of a positive temperature gradient (Trachte et al., 2010).

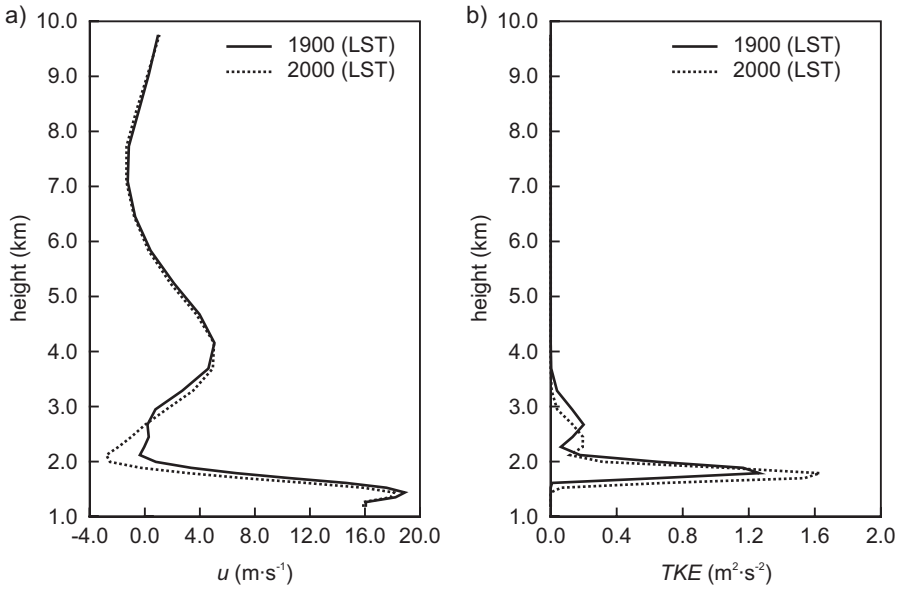

Figure 5.10: Profiles of a) the wind vector (u, m·s^{-1}) and b) the turbulent kinetic energy (TKE, m^2·s^{-2}) for 1900 LST and 2000 LST at -78.5° x -5.2°

Figures 5.10 and 5.11 support the assumption that the low-level flow seen in figure 5.9 is a thermally induced downslope. Figure 5.10 displays the TKE and a vertical profile, taken at an individual slope of the Andes at -78.5° x -5.2° of D4, of the wind velocity in u-direction. The wind profile discloses a jet-like profile in the lower atmosphere, which is typical for downslope motions with maximum wind speeds of 20.0 m·s^{-1}. Below this level, the velocity decreases as a result of ground friction; above it, the velocity is reduced by a decreasing positive temperature gradient. TKE occurs near the maximum of the mean wind speed with values of 1.6 m^2·s^{-2}. In addition to mechanically induced turbulence the vertical wind shear is the second main cause for TKE.

A further indicator for the development of katabatic flows is the heat exchange between the lower levels of the atmosphere and the surface. Figure 5.11 displays the surface fluxes and the net radiation (Rn) from 12 October 1300 LST to 13 October 1300 LST. They show the typical course of the transition from day to the night and back to day. A positive Rn is observed during the afternoon, which inverts to negative values between 1700 LST and 1800 LST due to the sunset and

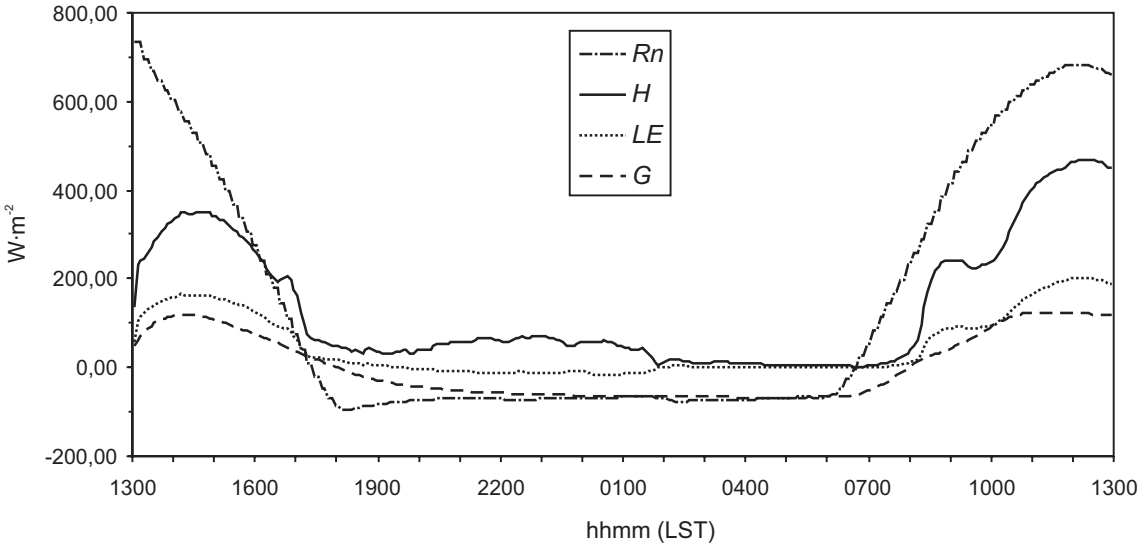

Figure 5.11: The heat energy fluxes in $W \cdot m^{-2}$ with the net radiation (Rn), the sensible heat flux (H), the latent heat flux (LE) and the ground heat flux (G) as a function of time between 12 October 1300 LST and 13 October 1300 LST taken at -78.5° x -5.2°

the associated begin of radiation loss. After a maximum peak of 100 $W \cdot m^{-2}$ at 1800 LST, the radiation loss achieves nearly constant values of 70 $W \cdot m^{-2}$ during the night. The surface fluxes change their direction correspondingly. As a result of the heating effect during the day, the sensible heat flux (H) has positive values but is reduced to almost zero at 1900 LST. The latent heat flux (LE) reduces as well, but keeps clearly positive until 0200 LST indicating a flux from the surface to the atmosphere due to evaporation. The ground heat flux (G) reach negative values as a result of the temperature deficit between the atmosphere and the surface layer. Therefore, an energy flux from the PBL to the surface layer exists, which is caused by a constantly cooling atmospheric boundary layer as a result of a negative radiation budget which is typical for nighttime. This can lead to the development of a surface inversion, as already indicated by the amount of negative buoyancy, which induces a positive temperature gradient. The surface heat fluxes indicate the development of thermally-induced katabatic flows, which are associated with the characteristic features of the downslope flow (figure 5.10).

5.5 Discussion

As expected, the nocturnal formation of the presented convective cloud south-east of Ecuador in the Peruvian Amazon basin is affected by well defined and strong downslope winds from the Andean slopes and valleys. Those katabatic flows induce a surface cold front at the foothills of the Andes in the Amazon basin. The special terrain configuration in the target area can cause the formation of a quasi-concave

terrain line with strong convergences. The underlying processes resulting in the formation of a cold cloud are examined using a case study (12 October to 13 October 2009) diagnosed by GOES-E satellite images. This outlines the impact of the terrain and, consequently, of the katabatic flows on the cloud formation: the 4 km domain (D3) reveals the absence of any cloudiness in the target area at nighttime, but in the inner domain (D4) a convective cloud cluster was generated (figure 5.2 and 5.3).

The atmospheric stability of both domains regarding the frontal zone and the thermodynamic structure was examined. The development of the katabatic induced surface front was described by the horizontal distribution of the equivalent-potential temperature (see figure 5.5). They show similar structures regarding the evolution of a horizontal gradient of θ_e in the cloud formation area. But even here, the impact of terrain and, subsequently, the downslope winds was visible. The cold drainage air in D4 propagated further into the basin, indicating a stronger flow.

A cross section through the front revealed first distinctions (see figure 5.6). While D4 demonstrated the vertical displacement of warm-moist air in the target area in one time step while the brightness temperature showed cold cloud patterns, D3 did not offer such structures. Although D3 has a potential instability and areas of high θ_e (354 K), which are sufficient for a destabilisation of the atmosphere (Machado et al., 2002), convective activities are completely absent.

An inspection of the environmental parameters gave more information concerning the reasons for the initiation and lacking convection, respectively (see figure 5.7). Both domains are marginally unstable, with a great amount of negative buoyancy in the lower levels. However, they also show a good potential for the development of a thunderstorm on the basis of the *LI* and *K-Index* (see table 5.3). The *LFC* in D3 and D4 are significantly different. In D3, the *LFC* for an ascending air parcel is reached at 3359 m, which is 1000 m higher than in D4. In association with the great amount of convective inhibition, which must be overcome first, a strong trigger function must be present. This trigger mechanism is assumed to be the convergence of the katabatic flows from the Andean mountains in connection with the Amazonian warm-moist air. As well, D4 demonstrated stronger convergence patterns indicating the initiation of sufficient vertical motions (see figure 5.8). In this process, the most accurate representation of the terrain, the surface fluxes as well and the resulting katabatic flows are important features.

Laurent et al. (2004) described that MCS initiation in South America is mostly driven by topography. Calbo and Millan (1998) also show the role of the terrain and highlight its influence on the model grid size. The authors demonstrated the significant impact of horizontal resolution on the vertical structure of the model domain. They ascertain that high resolved simulations increase the ability to develop stronger vertical velocities and that the vertical fluxes are more strongly developed. The vertical fluxes can result in modifications in the surface temperature and humidity field, which are sensitive to thermodynamic activities (Mapes and Houze, 1992). These surface fluxes are also the main driver for the development of thermally in-

duced katabatic flows. However, the vertical resolution essential for the evolution of the flows of both domains (D3 and D4) is identical, but the horizontal grid size differs. By increasing the horizontal resolution, as in domain D4, the complexity of the digital elevation model (DEM) increases as well. Thus, the terrain is more structured and the concave shape of the Andes in the target area is better revealed. The katabatic flows are stronger and the convergence in the target area increases. The result is a compressional lifting with markedly high vertical velocities due to a larger increase in pressure. In D4 sufficiently dynamic vertical motions occur, whereby the ascending air parcels reach the *LFC*. In contrast, the 4 km simulation generates weaker horizontal convergences with consequently ascending air parcels, which fail to reach their *LFC* (see figure 5.9). Therefore, the reason for the missing nocturnal cloudiness in domain D3 is that, in the current situation, the lower atmosphere requires a strong trigger to induce deep convection and the formation of a mesoscale cloud cluster. The chosen resolution of D3 is insufficient for this initiation mechanism, since it less represents the terrain, and thus, the katabatic flows and the increase in mass, which are the main driver.

In domain D4 ARPS underestimates the development of the generated convective cloud cluster, since the simulated cluster is smaller than the observed one (see figures 5.2, 5.3 and 5.4). The simulated brightness temperatures at the beginning of the night (2115 LST -0115 LST) showed two distinguishable systems with low IR temperatures (220 K) emerging at two separated regions different from the GOES-E data. But in these areas the convergence patterns, as a direct responds to the terrain (figure 5.8b), are strongest causing the convective initiation. Unlike the observed data, the simulated data do not merge to one convective system. The reason is the lack of a stronger upper level wind field (see figure 5.10) reaching values of approximately 1.5 $m \cdot s^{-1}$. However, new cells emerged at 0215 LST, which are more equal to the observed ones. They consisted of several organised cells within a cloud shield. These different occurring cells suggests two different initiation phases: one being the convergence due to the katabatic flows and the other in the second half of the night a cell regeneration due to the circulation dynamics of the convective cluster. Two different mechanisms of storm initiation in South America was also mentioned by Valesco and Fritsch (1987), although the authors describe one in the afternoon and one nocturnal.

Aside from this deviation, there are several conformances. As in the observed satellite data, the cloud cluster develops in the evening, grows during the night and dissipates in the early morning hours. The cells gain similar brightness temperatures and exhibit typical interior areas with lower values (below 220 K) as well. Even if the location is not exactly collocated with the observed data, the orientation of the cells are similar to the GOES-E data and, the error is marginal in comparison to the cloud physics. So for these conditions there is a good agreement between the satellite images and the modeled data.

A closer look at the development of the cloud cluster demonstrates the influence of the surface convergence by an intermittent influx of cold moist air, indicating drainage flow (figure 5.9). An analysis of an atmospheric profile regarding wind velocity, the *TKE* and heat exchange (figure 5.10 and 5.11) contribute to this result. Although the inversion layer is deeper than in a previous study concerning the confluence of katabatic flows (Trachte et al., 2010), it shows the specific jet-like profile and *TKE* characteristics. The reason for the deviation of the katabatic layer is its dependency on the vertical resolution; in this study, a coarser one was used. The idea that a katabatic flow develops is further supported by the surface fluxes representing diabatic heating. The results in figure 5.11 disclose a typical nocturnal course with net radiation loss and a corresponding energy flux from the PBL to the surface layer. It induces a buoyancy deficit, which is the driving force of the downslope flow.

Based on these results, and due to the fact that the 1 km domain (D4) used no cumulus parametrisation scheme (see table 5.1), a scale dependency for the initiation of these convective activities is assumed. Considering that katabatic flows are small-scale features, the demonstrated simulation results lead to the conclusion that they play a major role in the activation of convection. However, the thermally-induced downslope winds act only on the lower levels of the atmosphere in the PBL. They cause the formation of a surface inversion, which produces negative buoyancy (-146 $J \cdot kg^{-1}$ for D4). *CIN*, thus obtained in the PBL, has to be overcome first to reach the *LFC* with subsequent formation of cold clouds. Therefore, an additional trigger mechanism must be available for strong and sufficient lifting of air. In the light of the concave Andean ridge line south-east of Ecuador, which forms an extensive drainage system directed into the Amazon basin, this specific terrain geometry is extremely important. Particularly the confluence of the cold drainage of air due to the shape of the terrain results in a compressional lifting, which effectively removes the negative buoyancy. In this process, a destabilisation of the atmosphere is caused by the interaction with the warm-moist air of the Amazon, causing deep convection as shown in figure 5.9 and a previous idealised study (Trachte et al. submitted).

5.6 Summary and Conclusions

In this study, the mesoscale model ARPS was used to examine the development of a nocturnal cloud cluster south-east of southern Ecuador in the Peruvian Amazon basin. The main subject of the investigation is the demonstration of the driving mechanism behind the initiation of nocturnal deep convection. We hypothesised that cold drainage of air from the Andean slopes and valleys confluence due to the concave shape of the terrain in the target area. There it forms a katabatic induced surface cold front in connection with the warm-moist air of the Amazon basin. Beyond that, this confluence leads to compressional lifting of air, which causes atmospheric instabilities and the formation of convective clouds.

For the investigation, we used the night from the 12 to 13 October 2009, which was chosen based on GOES-E IR temperature images to identify an MCC in the target area. The data showed a quasi-circular pattern with minimum brightness temperatures of 220 K and an area of 12,000 km^2. The clear-sky conditions were particularly noticeable in the wider area of the MCS, which is favourable for the development of katabatic flows.

A comparison of the observed data with the modeled data was used to validate the simulations. First, we compared the 4 km domain with the observed data, but no convective patterns were observed. However, the 1 km domain revealed a convective cloud with minimum brightness temperatures comparable to the GOES-E data. Since the inner domain with the higher resolved terrain produced a multicell thunderstorm, we expect a scale dependency in convective activities concerning the DEM. The environmental parameters for both domain D3 and D4 reveal a marginally unstable atmosphere with a probability for deep convection. But the essential trigger mechanism, thus the katabatic flow and its strong confluence, is only well presented and strong enough in the more highly resolved 1 km domain.

A cross section through the simulated cloud cluster of the inner domain illustrated the initiation of convection and the formation of a multicell-cell thunderstorm. The data gave a first insight into the PBL and the occurrence of strong low-level flows. The assumption of a strong confluence leading to sufficient amounts of ascending of air was strengthened by the environmental parameters.

Finally, the PBL was more closely examined in order to identify whether the katabatic flows are the driving force for convective initiation. The formation of the downslope flow was shown by a profile taken at an individual slope of the Andes directed into the basin. Furthermore, the surface fluxes indicated a net radiation loss with a subsequent energy flux from the PBL to the surface layer, which is the driving mechanism for the development of katabatic flows.

The results of the presented study confirm the expected underlying processes resulting in convective activities with subsequent cold cloud formation. Moreover, they highlight that this specific cloud development is a local scale phenomenon which is not driven by mesoscale circulation. Hence they confirm our hypothesis that an interaction of katabatic flows with the concave shaped Andean drainage system in connection with the warm-moist air of the Amazon causes a confluence which is strong enough to cause compressional lifting, and that this lifting can induce the formation of a nocturnal cloud cluster.

Acknowledgment
The authors are indebted to the German Research Foundation (DFG) for the funding of the work in the scope of the Research Unit RU816 'Biodiversity and Sustainable Management of a Megadiverse Mountain Ecosystem in South Ecuador', sub projects B3.1 and Z1.1 (BE 1780/15-1, NA 783/1-1). We thank three anonymous reviewers for useful comments on this manuscript.

References

Angelis CF, McGregor GR, Kidd C (2004) A 3 year climatology of rainfall characteristics over tropical and subtropical south america based on tropical rainfall measuring mission precipitation radar data. Int J Climatol 24:385–399

Bendix J, Reudenbach C, Rollenbeck R (2003) The marburg satellite station. Proc Meteorol Satellite Users' Conf EUMETSAT, Dublin, Ireland pp 139–146

Bendix J, Rollenbeck R, Reudenbach C (2006) Diurnal patterns of rainfall in a tropical andean valley of southern ecuador as seen by a vertical pointing k-band doppler radar. Int J Climatol 26:829–846

Bendix J, Trachte K, Cermak J, Rollenbeck R, Nauss T (2009) Formation of convective clouds at the foothills of the tropical eastern andes (south ecuador). J Appl Meteor 48:1682–1695

Bluestein HB, Jain MH (1985) Formation of mesoscale lines of precipitation: Severe squall lines in oklahoma during the spring. J Atmos Sci 42:1711–1732

Bluestein HB, Jain MH (1987) Formation of mesoscale lines of precipitation: Nonsevere squall lines in oklahoma during the spring. Mon Wea Rev 115:2719–227

Businger JA, Wyngaard JC, Izumi Y, Bradley EF (1971) Flux-profile relationship in the atmospheric surface layer. J Atmo Sci 28:181–189

Byun DW (1990) On the analytic solutions of flux-profile relationships for the atmospheric surface layer. J Appl Meteor 29:652–657

Calbo J, Millan MM (1998) Horizontal grid size selection and its influence on mesoscle model simulations. J Appl Meteor 38:1311–1329

Chen Y, Weng F, Han Y, Liu Q (2008) Validation of the community radiative transfer model by using cloudsat data. J Geophys Res 113:D00A03, DOI 10.1029/2007JD009561

Chevallier F, Kelly G (1997) Model clouds as seen from space: Comparison with geostationary imagery in the 11-?m window channel. Mon Wea Rev 130:712–722

Chou MD (1990) Parameterization for the absorption of solar radiation by o2 and co2 with application to climate studies. J Clim 3:209–217

Chou MD (1992) A solar radiation model for climate studies. J Atmos Sci 49:762–772

Chou MD, Suarez MJ (1994) An efficient thermal infrared radiation parameterization for use in general circulation models. NASA Tech. Memo 104606, [Available from NASA Center for Aerospace Information, 800 Elkridge Landing Road, Linthicum Heights, MD 21090-2934]

Colby FP (1984) Convective inhibition as a predictor of convection during avesesame ii. Mon Wea Rev 112:2239–2252

Cotton WR, Lin MS, Anelly RL, Tremback CJ (1989) A composite model of mesoscale convective complexes. Mon Wea Rev 117:765–783

Deardorff JW (1972) Parameterization of the planetary boundary layer for use in general circulation models. Mon Wea Rev 100:93–106

Defant F (1949) Zur theorie der hangwinde, nebst bemerkungen zur theorie der berg- und talwinde. Arch Meteorol Geophys Bioklim A1:421–450

Garreaud RD, Wallace JM (1997) The diurnal march of convective cloudiness over the americas. Mon Wea Rev 125:3157–3171

Houze RA (ed) (1995) Cloud Dynamics. Academic Press

Houze RA (2004) Mesoscale convective systems. Rev Geophys 42:RG4003, DOI 10.1029/2004RG000150

Jirak IL, Cotton WR, McAnelly RL (2003) Satellite and radar survey of mesoscale convective system development. Mon Wea Rev 131:2428–2449

Kanamitsu M, Ebisuzaki W, Woollen J, Yang SK, Hnilo JJ, Fiorino M, Potter GL (2002) Ncep-doe amip-ii reanalysis (r-2). Bull Amer Meteor Soc 83:1631–1643

Laurent H, Machado LAT, Morales CA, Durieux L (2004) Mesoscale convective systems. Rev Geophys 42:RG4003, DOI 10.1029/2004RG000150

Lin YL, Farley RD, Orville HD (1983) Bulk parameterization of the snow filed in a cloud model. J Clim Appl Meteor 22:1065–1092

Lopez ME, Howell WE (1967) Katabatic winds in the equatorial andes. J Atmos Sci 24:29–35

Machado LAT, Laurent H, Lima AA (2002) Diurnal march of the convection observed during trmm-wetamc/lba. J Geophys Res 107:8064, DOI 10.1029/2001JD00338

Maddox RA (1980) Mesoscale convective complexes. Bull Amer Meteor Soc 61:1374–1387

Maddox RA (1983) Large-scale meteorological conditions associated with midlatitude mesoscale convective complexes. Int J Climatol 111:1475–1493

Mapes BE, Houze RA (1992) An investigated view of 1987 australian monsoon and its mesoscale convective systems, part i, horizontal structure. Q J R Meteorol Soc 118:927–963

Mapes BE, Warner TT, Xue M (2003) Diurnal patterns of rainfall in northwestern south america. part i: Observations and context. Mon Wea Rev 131:799–812

Moncrieff MW, Miller MJ (1976) The dynamics and simulation of tropical cumulonimbus and squall lines. Quart J Roy Meteor Soc 102:373–394

Morcrette JJ (1991) Evaluation of model-generated cloudiness: Satellite-observed and model-generated diurnal variability of brightness temperature. Mon Wea Rev 119:1205–1224

Noilhan J, Planton S (1989) A simple parameterization of land surface processes for meteorological models. Mon Wea Rev 117:536–549

Poveda G, Mesa OJ, Salazar LF, p A Arias, et al HAM (2004) The diurnal cycle of precipitation in the tropical andes of colombia. Mon Wea Rev 133:228–240

Prandtl L (ed) (1942) Stroemungslehre (Flow studies). Vieweg und Sohn, Braunschweig, Germany

Rickenbach TM (2004) Nocturnal cloud systems and the diurnal variation of clouds and rainfall in southwestern amazonia. Mon Wea Rev 132:1201–1219

Sato T, Miura H, Satoh M, Takayabu YN, Wang Y (2009) Diurnal cycle of precipitation in the tropics simulated in a global cloud-resolving model. J Clim 22:4809–4826

Sun Z, Rikus L (2004) Validating model clouds and their optical properties using geostationary satellite imagery. Mon Wea Rev 132:2006–2020

Trachte K, Nauss T, Bendix J (2010) The impact of different terrain configurations on the formation and dynamics of katabatic flows - idealized case studies. Bound-Layer Meteor 134:307–325

Trigo IB, Viterbo P (2003) Clear-sky window channel radiances: A comparison between observations and the ecmwf model. J Appl Meteor 42:1463–1479

Valesco I, Fritsch JM (1987) Mesoscale convective complexes in the americas. J Geophys Res 92:9591–9613

Weinreb MP, Jamieson M, Fulton N, Chen Y, Johnson JX, Bremer J, Smith C, Baucom J (1997) Operational calibration of geostationary operational environmental satellite-8 and -9 imagers and sounders. Appl Optics 36:6895–6904

Xue M, Martin WJ (2006) A high-resolution modeling study of the 24 may 2002 dryline case ihop. part i: Numerical simulations and general evolution of the dryline and convection. Mon Wea Rev 134:149–171

Xue M, Droegemeier KK, Wong V, Shapiro A, Brewster K (eds) (1995) Advanced Regional Prediction System (ARPS) version 4.0 user's guide. Center for Analysis and Prediction of Storms, University of Oklahoma

Xue M, Droegemeier KK, Wong V (2000) The advanced regional prediction system (arps) - a multiscale nonhydrostatic atmospheric simulation and prediction tool. part i: Model dynamics and verification. Meteor Atmos Phys 75:161–193

Xue M, Droegemeier KK, Wong V, Shapiro A, Brewster K, Carr F, Weber D, Liu Y, Wang DH (2001) The advanced regional prediction system (arps) - a multiscale nonhydrostatic atmospheric simulation and prediction tool. part ii: Model physics and applications. Meteor Atmos Phys 76:134–165

Yang GY, Slingo J (2001) The diurnal cycle in the tropics. Mon Wea Rev 129:784–801

6 Summary and Outlook

6.1 Summary

The development of clouds has many causes, not all of those are examined. In consideration of rainfall behaviour and distribution knowledge of cloud formation, processes in the tropics are of particular importance. Clouds are part of the hydrological cycle, influencing water resources and the energy budget. The insight into unknown cloud generation processes is a great benefit in the developmental procedure of understanding the structure and functionality of an ecosystem and its biodiversity.

The main objective of the presented study was to investigate an unidentified nocturnal cloud formation procedure in the eastern Andes of South Ecuador and the adjacent northern Peruvian Amazon. The central theses encompass the confluence of katabatic flows in highly complex terrain due to a concave configuration. This cold drainage of air induces a surface cold front in the foothills of the eastern Andes, which initiates moisture convection due to compressional lifting by the terrain; a nocturnal LLJ triggers the development of the MCS.

For the evaluation of the hypotheses the numerical model ARPS was used to analyse the not fully understood highland - lowland interactions in the PBL. ARPS, with its dynamic framework and comprehensive physics, provides the essential components for the applied method. The investigations of the presented study consists of three main parts:

1. At first, simulations of an accurate katabatic flow and its behaviour in complex terrain were performed with optimal conditions and without location information. The main subject of the study was the confluence of the cold drainage of air as a result of concave-lined terrain. Simplified DEMs, inspired by the Andes, were used for this analysis, due to the very steep slopes and valleys of the real terrain. A stepwise increase in their complexity, beginning with a simple slope, enabled the examination of the impact of the terrain configuration on the flow's dynamic behaviour. Typical characteristics, such as the jet-like profile and the katabatic layer, were used to show that a katabatic flow developed. Furthermore, it could be demonstrated that the flow was thermally induced, driven by surface fluxes along with net radiation loss. With the most complex terrain model, which represents a concave ridgeline interrupted by several valleys draining into a basin, the confluence of the downslope flows due to the geometry of the terrain was demonstrated. Thus, a representative,

persistent, thermally driven flow was generated, creating a convergence line that was largest in the centre of the basin.

2. Afterwards, a simulation of a katabatically induced surface cold front with subsequent convective cloud formation was performed with the same model framework, except for the atmospheric water vapour. The initial sounding achieved sufficient atmospheric moisture for convection. The simulation showed the same confluence of the downslope flows with a convergence line inside the basin as before. The development of a katabatically induced cold front was identified based on characteristic attributes described in chapter 2 using a cross-section through this line. Furthermore, the results also showed a convergence line that was largest in the centre of the basin. Because of the initiation of moisture convection in this area, due to sufficient moisture in the atmosphere, it was evident that the terrain geometry was the triggering mechanism for cloud formation. The persistent drainage of cold air into the basin nourished the convective activities and a multi-cell cloud cluster was generated. The presence of an LLJ in the basin showed the intensification of the cloud formation process. However, the previous results showed that the cluster developed primarily due to compressional lifting by the terrain. This shows that the LLJ had marginal effects on the initiation of moisture convection, acting primarily as an enhancement of its occurrence.

3. Finally, the spatial reference was enabled and the parametrisation set-up of the idealised studies was assigned and adjusted to a multi-nested, approximately realistic model setting, strengthening the evidence from the previous results. For the study, a specific situation, selected on the basis of GOES-E satellite data encompassing the essential atmospheric conditions, such as an MCS in the target area and clear-sky conditions for the development of katabatic flows, was used. The main subject was the demonstration of the development of an MCS in the foothills of the eastern Andes due to the presence of katabatic flows as the driving mechanism. The GOES-E brightness temperatures were used to compare the satellite-observed data with the ARPS data to verify the simulated cloud appearance. Due to the fact that the 4 km domain revealed no convective clouds, but a convective cloud cluster was generated on the 1 km domain, a scale dependency was determined. This was caused by two factors: first of all, the NBL processes were simulated more accurately due to the higher vertical resolution, thus more accurately representing the katabatic flows. Furthermore, the higher resolved domain represented a more structured terrain, resulting in stronger convergences of the downslope flows. The comparison of the satellite and the modelled data presented a good agreement concerning the orientation, the location as well as the cold tops of the cells. A closer look at the NBL revealed cold air drainage, nourishing the cell regeneration. The typical characteristics, discussed in the idealised study without location

information, confirmed the occurrence of thermally induced downslope flows as the driving process behind convective initiation.

The investigations of the presented work have shown that the expected underlying processes, i.e. katabatic flows and their confluence due to the configuration of the terrain, are effectual in lifting air to initiate convection. It was also confirmed that these flows play a major role in the specific occurrence of nocturnal convective cloud systems in the eastern Andes of South Ecuador. The idealised studies demonstrated the dynamic procedure under optimal conditions without a disturbing atmospheric environment. By using a selected situation, the test case also showed the cloud formation and downslope motions. For that reason, the hypothesised mechanism of katabatic flows interacting with the Andean terrain resulting in convective activities and the development of an ensemble of deep cumulus clouds can not be disproven, and thus should be accepted as an occurring procedure. Moreover, the test case study disclosed a scale dependency of the initiation of moisture convection, which should be taken into account when examining weather phenomena with an atmospheric numerical model.

6.2 Outlook

The presented research findings regarding the nocturnal cloud formation process in the eastern Andes indicate that further investigations should be conducted. The simulation and evaluation results confirmed the feasibility of the mechanism and allowed a good understanding of the interaction between the responsible atmospheric aspects and the highly complex terrain.

Measurement data are necessary in order to enhance these results and obtain more insight into environmental atmospheric conditions during a nocturnal MCS event. With observing platforms consisting of several methods, such as a Sodar system, wind profiler and towers with various instruments, a broad range of atmospheric effects could be recorded (Angavine et al., 1998; Adachi et al., 2004; Princevac et al., 2008). In consideration of the wide area, the instruments have to be distributed over the target area and placed along the slopes and valleys of the Andes draining into the Amazon to capture katabatic flows and the environmental conditions. With an extensive measuring network, atmospheric effects that probably affect the nocturnal cloud development would be detected. The observed data can be used to initialise the numerical model, which is beneficial for a LES study. The aim of such a study is the decrease of applied parametrisation schemes to explicitly simulate the aspects of interest. A more detailed insight into the boundary layer processes such as the interaction between the surface and the atmosphere (Skyllingstad, 2003) might be achieved. Another factor that affects the development of the flows is the shading effect of the terrain. Particularly in such a complex terrain, those modifications in the radiation budget can alter its occurrence (Chow et al., 2006). But that, in turn,

requires a highly resolved grid with sufficiently highly resolved initial values in-depth for the atmosphere and the land coverage provided by the measuring campaign.

On the other hand the impact of this novel discovered cloud formation mechanism on the annual precipitation patterns would be of importance. In this context, possible modifications of the precipitation behaviour and its statistical relevance should be examined. The newly gained knowledge of scale dependency regarding the resolution of terrain should be used to record relevant diviations to the annual precipitation mean. If these diviations are significant, they have a great impact on the water resources and energy budget and should be accounted for during climate simulations to enhance the accuracy of their results.

Considering the planned scenario simulations for the central Andes within the second phase of the DFG RU 816 the information about the water energy budget would be very useful. Questions that do arise are whether this mechanism can be captured during a long-term run and whether it occurs during a climate change scenario. Within the climate change discussion modified atmospheric conditions might result in an altered hydrological cycle. Those changings can affect the biodiversity of the mountain forest by means of a varying vegetation composition due to an altered precipitation behaviour and following temperature patterns. This in turn influences the evolution of the katabatic flows by modified features such as the roughness length and the wind speed. In addition, the surface properties affect the radiation budget by modifying the surface heat fluxes, and thus the net radiation (see chapter 3 for more details). Hence, climate change feedbacks may result in a changed land coverage and thus, influences the development of katabatic flows. The subsequent formation of nocturnal MCS could be changed or could no longer occur, which might result in shift of precipitation and temperature patterns. If such a special mechanism of convective cloud development is taken into account during climate change scenario simulations potential modifications of precipitation behaviour might be predicted more accurately. Again, effects of changing atmospheric conditions on the flora and fauna might be better predicted as well. The knowledge gained would be an additional, valuable advancement in understanding the complex structure and possible change of the biodiversity of the ecosystem in the tropical mountain rain forest of southern Ecuador.

References

Adachi A, Clark WL, Hartten LM, Gage KS, Kobayashi T (2004) An observational study of a shallow gravity current triggered by katabatic flow. Annales Geophys 22:3937 – 3950

Angavine WM, Grimsdell AW, Hartten LM, Delany AC (1998) The flatland boundary layer experiments. Bull Amer Meteorol Soc 79:419 – 431

Chow FK, Weigel AP, Street RL, Rotach MW, Xue M (2006) High-resolution large-eddy simulations of flow in a steep alpine valley. part i: methodology, verification, and sensitivity experiments. J Appl Meteorol Climatol 45:63–86

Princevac M, Hunt JCR, Fernando HJS (2008) Quasi-steady katabatic winds on slopes in wide valleys: Hydraulic theory and observations. J Atmos Sci 65:627 – 643

Skyllingstad ED (2003) Large-eddy simulation of katabatic flows. Boundary-Layer Meteorol 106:217–243

Zusammenfassung

Die Entstehung von Wolken hat vielfältige Gründe; nicht alle davon sind bisher erforscht. Wissen über Wolkenentstehungsprozesse in den Tropen ist hinsichtlich des Niederschlagsverhaltens und dessen Verteilung von großer Bedeutung. Wolken sind ein Teil des hydrologischen Zyklusses, der wiederum die Wasserressourcen und den Energiehaushalt beeinflusst. Aus diesem Grund ist die Erkenntnis solch unbekannter Wolkenentstehungen von großem Nutzen in dem sich permanent weiterentwicklenden Prozess des Verstehens der Struktur und der Funktionalität eines Ökosystems und seiner Biodiversität.

Das Hauptziel der vorliegenden Studie war die Untersuchung einer unbekannten nächtlichen Wolkengenese an der östlichen Abdachung der Anden von Süd-Ecuador und des angrenzenden Peruanischen Amazonas. Die zentralen Thesen umfassen die Konfluenz katabatischer Flüsse in hoch komplexem Gelände aufgrund einer konkaven Form. Diese Kaltluftabflüsse induzieren eine lokale Kaltfront am Fusse der östlichen Anden, die wiederum hochreichende Konvektion durch Kompressionshebung aufgrund des Geländes auslöst.

Zur Evaluierung der Hypothesen ist das numerische Modell ARPS verwendet worden, um die nicht vollständig verstandene Hochland-Tiefland Interaktion in der planetaren Grenzschicht zu analysieren. ARPS stellt mit seinem dynamischen Rahmen und seiner umfassenden Modellphysik die notwendigen Komponenten für die angewandte Methode zur Verfügung. Die Untersuchungen der vorliegenden Studie bestehen aus drei Hauptkomponenten:

1. Zunächst wurden ideale Siumlationen von katabatischen Flüssen und deren Verhalten in komplexem Gelände durchgeführt ohne einen Raumbezug und mit optimalen Bedingungen. Das Ziel der Studie war die Analyse der Konfluenz der Kaltluftabflüsse hervorgerufen durch die konkave Form des Geländes. Vereinfachte Höhenmodelle, abgeleitet von den Anden, wurden aufgrund der sehr steilen Hänge und Täler des eigentlichen Geländes für diese Analyse genutzt. Eine schrittweise Erhöhung deren Komplexität, beginnend mit einem einfachen Hang, ermöglichte die Untersuchung des Einflusses des Geländes auf das dynamische Verhalten des Hangabwindes. Anhand typischer Eigenschaften wie z.B. das 'jet-like' Profil und der katabatische Layer, konnte gezeigt werden, dass sich ein katabatischer Fluss entwickelte. Des weiteren konnte gezeigt werden, dass dieser Fluss thermisch induziert wurde, angetrieben von den Bodenwärmeflüssen einhergehend mit der Netto-Ausstrahlung. Mit dem

komplexesten Höhenmodell, das einen konkaven Höhenzug mit einschneidenden Tälern, die in ein Becken drainieren, representiert, wurde die Konfluenz des Hangabwindes aufgrund der Geometrie des Geländes demonstriert. Folglich wurde ein charakteristischer, permanenter thermisch-induzierter Fluss generiert, der eine Konvergenzlinie erzeugte, die im Zentrum des Beckens am ausgeprägtesten war.

2. Anschließend wurden Simulationen der katabatisch induzierten Bodenkaltfront mit daraus folgender konvektiver Wolkengenese durchgeführt und zwar mit dem gleichen Modell-Setup außer dem Wasserdampfgehalt der Atmosphäre: Das Initialisierungssounding wurde mit ausreichend Feuchte für Konvektion ausgestattet. Die Simulationen zeigten die gleiche Konfluenz der Hangabwinde mit einer Konvergenzlinie innerhalb des Beckens wie zuvor. Mit einem Querschnitt durch diese n Bereich wurde die Entwicklung einer katabatisch induzierten Kaltfront anhand kennzeichender Eigenschaften, identifiziert. Des weiteren zeigten die Ergebnisse ebenfalls eine Konvergenzlinie, die im Zentrum des Beckens am ausgeprägtesten war. Aufgrund des Einsetzens der Konvektion in diesem Gebiet, hervorgerufen durch ausreichend Feuchte in der Atmosphäre, war es ersichtlich, dass die Geländegeometrie der Auslöser für die Wolkenentstehung war. Der anhaltende Kaltluftabfluss in das Becken hinein nährte die konvektiven Aktivitäten und ein Mehrzellen-Wolkencluster wurde generiert. Die Anwesenheit eines LLJ im Becken zeigte eine Intensivierung der Wolkengenese. Doch die vorherigen Ergebnisse verdeutlichten, dass der Cluster primär aufgrund der Kompressionshebung durch das Gelände erzeugt wurde. Daher hatte der LLJ nur geringfügige Effekte auf die Auslösung der Feuchtekonvektion, sondern eher eine verstärkende Wirkung auf ihre Ausprägung.

3. Abschließend wurde der Raumbezug wieder hergestellt und die Parametrisierung der idealen Studie auf ein mehrfach genestetes annährend realistisches Modellsystem übertragen und angepasst. Für diese Studie wurde eine spezifische Situation verwendet, die anhand von GOES-E Satellitendaten selektiert wurde und alle relevanten Bedingungen wie MCS im Zielgebiet und wolkenlose, klare Nacht umfasste. Das Ziel war das Aufzeigen von katabatischen Flüssen, die in der Erzeugung konvektiver Wolken am Fusse der östlichen Anden resultierten. GOES-E brightness temperature/Helligkeitstemperaturen wurden zum Vergleich von Satellitendaten mit ARPS Daten verwendet, um die simulierte Wolke zu verifizieren. Aufgrund der Tatsache, dass auf der 4 km Domain keine Konvektionsbewölkung zu sehen war, aber die 1 km Domain einen konvektiven Wolkencluster aufgewiesen hatte, wurde eine Skalenabhängigkeit festgestellt. Sie wurde dadurch verursacht, dass auf der inneren Domain keine Konvektionsparametrisierung verwendet wurde und durch die höhere Auflösung die Prozesse der nächtlichen Grenzschicht besser aufgelöst wurden. Der Vergleich der Satellitendaten mit den Modelldaten zeigte eine

gute Übereinstimmung hinsichtlich der Größe des Clusters sowie seiner Oberflächentemperaturen und seiner Lokalisierung. Mit einem näheren Blick auf die nächtliche Grenzschicht konnten Kaltluftabflüsse, die die Zellregeneration nährten, festgestellt werden. Die kennzeichnenden Eigenschaften, die bereits in der idealen Studie vorgestellt wurden, bestätigten die Ausprägung von thermisch induzierten Hangabwinden als antreibender Prozess bei der Aktivierung der Konvektion.

Die Untersuchungen der vorliegenden Arbeit haben gezeigt, dass die vermuteten zugrundeliegenden Prozesse der nächtlichen Grenzschicht ausgelöst werden von einer Kompressionshebung durch die Form des Geländes. Es wurde ebenfalls bestätigt, dass diese Flüsse verantwortlich sind für ein bestimmtes Auftreten von nächtlichen konvektiven Wolkensystemen an der Andinen Ostabdachung Süd-Ecuadors. Die ideale Studie hat die dynamische Prozedur unter optimalen Bedingungen und ohne überlagernde und störende atmosphärische Umgebung gezeigt. Anhand eines bestimmten Ereignisses stellte dieser Testfall das Wolkensystem sowie die Kaltluftabflüsse ebenfalls dar. Aus diesem Grund kann der angenommene Mechanismus interagierender katabatischer Flüsse mit dem Andinen Gelände, welches in Konvektion und Wolkenbildung resultiert, nicht falsifiziert werden, sondern sollte daher als auftretender Mechanismus akzeptiert werden. Darüberhinaus verdeutlichte die reale Studie eine Skalenabhängigkeit bezüglich der Feuchtekonvektion, die Berücksichtigung finden sollte bei der Untersuchung von Wetterphänomenen mit einem numerischen Atmosphärenmodell.